Vertically Aligned (In)GaN Nanowires Grown by MOCVD

by

Hsun Chih Kuo

A dissertation submitted in partial fulfillment
of the requirements for the degree of
Doctor of Philosophy
(Electrical Engineering)
in the University of Michigan
2014

Doctoral Committee:

Associate Professor Pei-Cheng Ku, Chair

Professor Jamie D. Phillips

Assistant Professor Emmanouil Kioupakis

Assistant Professor Stephen Maldonado

TABLE OF CONTENTS

LIST OF TABLES vi

LIST OF FIGURES vii

LIST OF APPENDICES xiv

ABSTRACT xv

CHAPTER 1 1
Introduction 1

1.1 InGaN Material 1

1.2 High GaN Film Quality using LEO and Core-shell Nanowires 5

1.3 (In)GaN Axial Nanowires 7

1.4 High GaN Film Quality using Axial NWs 9

1.5 Dissertation Overview 11

CHAPTER 2 13
High-Quality GaN Thin Film Template 13

2.1 Vapor-Liquid-Solid and Vapor-Solid-Solid Growth Mechanisms 15

2.2 GaN Film on GaN NWs 17

2.2.1 GaN NWs on Sapphire 17
2.2.2 Tilted and Twisted GaN NWs 19
2.2.3 GaN Thin-Film Growth 21
2.2.3.1 First and Second Stages of GaN Film Growth 22
2.2.3.2 Third Stage of GaN Thin-Film Growth 24
2.2.4 Overview of GaN film on NW template 27

2.3 Results and Discussion 29
2.3.1 Strain Distribution of GaN NWs 29
2.3.2 Photoluminescence Study 31
2.3.3 XRD Results 33
2.3.4 TEM Results 36
2.3.5 Extended Defects 39
2.3.6 Overview of the Results and Discussion 41
2.4 Multi-stack GaN Growth 43
2.4.1 GaN NW Growth 44
2.4.2 Tilted and Twisted GaN NWs on Each Stack 46
2.4.3 Second- and Third-stack GaN Growth 48
2.4.4 XRD Results for Different Stacks 51
2.4.5 Estimation of Anisotropy with Various NW Densities 53
2.4.6 Overview of Multi-Stack GaN Growth 55
2.5 Summary 56
CHAPTER 3 58
InGaN NW Growth by MOCVD 58
3.1 InGaN NW Growth 58
3.1.1 Surface Morphology Control Experiment 58
3.1.2 Impact of Growth Temperature 60
3.1.3 Impact of Growth Pressure 62
3.1.4 Summary 63
3.2 Analysis of NW structure 66
3.3 Time dependent InGaN NW Growth 67
3.3.1 Time-dependent Evolution of NW Growth 70
3.3.2 Ni Catalysts with Growth Time 70
3.3.3 Vertical Length and Base Diameter with Growth Time 72
3.3.4 Base Diameter with Growth Time 73
3.3.5 Vertical Length with Growth Time 75
3.3.6 Three Facets with Growth Time 77
3.3.7 Overview of InGaN NW growth model 78
3.4 Summary 78

CHAPTER 4 80
Properties of InGaN NWs 80

4.1 Optical Properties 80

4.1.1 Photoluminescence and Cathodoluminescence 80
4.1.2 Energy-Dispersive Spectroscopy 83
4.1.3 Temperature-dependent Photoluminescence 84
4.1.4 Temperature-dependent and Time-resolved Photoluminescence 86
4.1.5 Overview of optical properties 88

4.2 Emission Energy of Bulk InGaN NWs 89

4.2.1 Surface Morphology 89
4.2.2 Fabrication Development for Optical Measurement 90
4.2.3 Tunable Emission Energy up to 2.5 eV 93
4.2.4 Overview of emission energy of bulk InGaN NW 94

4.3 Material Properties 96

4.3.1 InGaN Bottom Thin Film and Bulk Region 96
4.3.2 InGaN NW Surface Oxide Layer 98
4.3.3 InGaN NW Tip 100
4.3.4 Overview of material properties 101

4.4 Summary 102

CHAPTER 5 103
Contributions and Future Work 103

5.1 Overview of Contributions 103

5.1.1 Vertical InGaN NWs 104
5.1.2 High-quality a-plane GaN 105

5.2 Future Work 106

5.2.1 Development of Solar Cells using InGaN NWs 106
5.2.2 Device Concepts 106
5.2.3 Fabrication Design 108
5.2.4 Photocurrent Response 110
5.2.5 Summary 112

APPENDICES 113
Appendix A: Wurtzite Nitrides Structure 114
Appendix B: Parameters for III-nitrides 116

BIBLIOGRAPHY 117

LIST OF TABLES

Table 2.1	FWHM of the (11$\underline{2}$0) reflection of a-plane GaN films grown on various NW densities and a control sample	35
Table 2.2	FWHM values of the (11$\underline{2}$0) reflection of *a*-plane GaN films grown on various NW densities and a control sample	53
Table 4.1	The average and FWHM value of In composition from XRD, EDX, and PL measurement	96
Table 5.1	Photocurrent response from the experimental results of InGaN NW samples	112

LIST OF FIGURES

Figure 1.1	Schematic diagram of (a) GaN laterally epitaxially overgrown and (b) core-shell InGaN/GaN MQWs nanowires device	6
Figure 1.2	Schematic diagram of (a) LED devices under GaN NWs template structure and (b) substrate lift off and deposit contacts	11
Figure 2.1	Schematic epitaxial growth of an *a*-plane GaN on *r*-plane sapphire, typically in the directions shown.	14
Figure 2.2	Schematic drawing of a GaN film on top of GaN NWs.	15
Figure 2.3	Schematic illustrating the growth of a NW by the VLS mechanism. Phase 1: atoms dissolve into catalyst. Phase 2: atoms separate out from catalyst. Phase 3: material deposits at interface.	16
Figure 2.4	GaN NW series grown on *r*-plane sapphire substrates with various annealing conditions, time, and temperature. “T” represents the annealing temperature, and “t” represents the annealing time.	18
Figure 2.5	Slightly tilted and twisted NWs are observed in SEM images of the first stage of GaN film growth: (a) cross-sectional and (b) top-view images correlate to tilted and twisted NWs, respectively.	20
Figure 2.6	Histograms of (a) tilted and (b) twisted angle distributions of GaN NWs grown on *r*-plane sapphire substrates with various NW densities. The FWHMs of the NW distributions were estimated by fitting Gaussian functions (black lines).	21
Figure 2.7	45°-tilted and cross-sectional (inset) SEM images of the (a) first and (2) second stages of GaN growth. Part (a) illustrates a wire-like surface morphology, whereas (b) illustrates a film-like morphology.	24

Figure 2.8	LEXT images of GaN atop a NW template at the third stage of growth, taken after (a) 30, (b) 60, and (c) 120 min. Image (d) shows a control sample of GaN on sapphire without NW as a base with 120 min of growth. RMSs were calculated from $130 \times 130\ \mu m^2$LEXT images.	26
Figure 2.9	Schematic of the growth parameters (temperature, pressure, and V:III ratio) for GaN grown on a NW template at each stage.	27
Figure 2.10	Schematic of the growth process of an *a*-plane GaN film on GaN NW/r-plane sapphire based on SEM observations. Picture 1: Ni-catalyzed GaN NWs on an r-sapphire substrate; Picture 2: first GaN nanostructures grown along GaN NW side walls; Picture 3: second stage of GaN layer growth; Picture 4: third stage of GaN growth with full coalescence. The insets are cross-sectional SEM images corresponding to each figure. All processes were carried out in an MOCVD reactor without any growth interruptions.	28
Figure 2.11	2D strain simulation calculated by NEXTNANO: (a) color mapping of the strain distribution in a GaN NW on an r-plane sapphire substrate (assuming 15.4% lattice mismatch) and (b) relative elastic energy as a function of distance from the substrate. The spacing between each point is $10\ nm$; point A is $30\ nm$ below the interface, and point G is 50 nm away from the interface.	30
Figure 2.12	Raman spectra of a GaN NW sample grown on an r-plane sapphire substrate by Ni-catalyzed VSS growth. Two common strain-free frequencies, $A_1(TO)$ and $E_2(high)$, are shown on the left in Raman spectra measured along both the *c*- and *m*-axes. An illustration of these two frequencies is shown on the right.	31
Figure 2.13	(a) Low-temperature (20 K) PL and (b) SEM images of each stage of GaN film growth.	33
Figure 2.14	XRD of the (11$\underline{2}$0) reflection of *a*-plane GaN films grown on GaN NWs and reference GaN. (a) and (b) correspond to diffraction planes parallel to the *c*- and *m*-axes, respectively. (c) FWHM variation of the XRC for a-plane GaN films with the azimuth angle. (d) FWHM difference of a-plane GaN and a reference as a function	35

	of the azimuth angle. Dotted lines indicate linear fitting.	
Figure 2.15	(a) STEM image of the GaN NW region. The contract line indicates the border area between the initial GaN NW and first-stage GaN nanostructure. (b) Low-magnification cross-sectional TEM image near the interface between GaN and the *r*-sapphire substrate.	37
Figure 2.16	(a) STEM image of two GaN NWs overlapped near the interface region with the substrate; (b) STEM image of first-stage GaN NWs with small mis-orientation; SAED patterns taken from NW_1 and NW_2 are shown in the inset.	39
Figure 2.17	Schematic of two merged NWs. Tilted NWs can cause extended defects.	40
Figure 2.18	Schematic of two merged NWs. Twisted NWs can cause extended defects.	41
Figure 2.19	Schematic of GaN film grown on multi-stacks. Picture 1: GaN NWs on sapphire. Picture 2: first-stack GaN. Picture 3:GaN NWs on the first-stack GaN. Picture 4: second-stack GaN on NWs.	44
Figure 2.20	SEM images of GaN NWs grown on a first-stack GaN film with (a) 300, (b) 180, (c) 120, and (d) 60 *s* of annealing time. The other conditions are held constant.	45
Figure 2.21	Histograms of (a) tilted and (b) twisted angle distribution of GaN NWs grown on each stack with various NW densities. The FWHM values of the NW distributions were estimated by fitting Gaussian functions (black lines).	46
Figure 2.22	(a) Tilted NW density and (b) FWHM of the twisted angle as a function of total GaN NW density grown on each stack.	47
Figure 2.23	LEXT images were taken from (a) GaN on sapphire, (b) first-stack GaN on a NW template, (c) second-stack GaN on a NW template, and (d) third-stack GaN on a NW template	50
Figure 2.24	XRD of the (11$\underline{2}$0) reflection of *a*-plane multi-stack GaN films grown on GaN NWs and the reference GaN. (a) and (b) correspond to diffraction planes parallel to the *c*- and *m*-axes, respectively. (c) FWHM variation of the XRC for *a*-plane GaN films with the azimuth angle. (d)	52

	FWHM differences of *a*-plane GaN and that of a reference as a function of the azimuth angle. The dotted lines indicate linear fitting.	
Figure 2.25	Estimation of the FWHM ratio of the *m*-axis to the *c*-axis for each stack with various NW densities.	54
Figure 2.26	Schematic of the growth parameters (temperature, pressure, and V:III ratio) for multi-stack GaN grown on a NW template.	55
Figure 3.1	Schematic illustrating the VSS growth mechanism. Picture 1: single-side-polished *r*-plane sapphire, Picture 2: deposited 3 nm Ni film on top of sapphire, Picture 3: annealed Ni film to form Ni catalysts, Picture 4: vertical InGaN NW growth	60
Figure 3.2	The 45°-tilted SEM images of InGaN NW grown at growth temperatures of (a) 600, (b) 685, (c) 715, and (d) 735℃. The growth pressure was fixed at 300 $torr$. The scale bar is 5 μm.	61
Figure 3.3	The 45°-tilted SEM views of InGaN NWs grown at pressures of (a) 50, (b) 100, (c) 200, and (d) 400 $torr$. The growth temperature was fixed at 715℃. The scale bar is 5 μm.	63
Figure 3.4	InGaN NW density and fraction of vertical aligned NWs as a function of (a) growth temperature and (b) growth pressure.	65
Figure 3.5	SEM images: (a) 45° tilted, (b) cross sectional, and (c) top view. (d) Schematic diagram of an InGaN NW. The NW growth direction is along [11$\underline{2}$0] and consists of three facets.	67
Figure 3.6	(a) Three-dimensional AFM image of the substrate after annealing for 900 s; (b) histogram of Ni catalyst distribution based on AFM images. The average diameter is 14.6 nm.	68
Figure 3.7	Schematic illustrating the growth of InGaN NWs by the VSS mechanism on an *r*-plane sapphire substrate. Picture 1:0.3 nm Ni on an r-plane sapphire substrate; Picture 2: Ni_2Ga_3 compound formation; Picture 3: NW growth by the VSS mechanism; Picture 4: NW growth by both VSS and epitaxial thin growth.	69
Figure 3.8	TEM images of InGaN NW tips after (a) 600 and (b)	71

	$1{,}200\ s$ of growth.	
Figure 3.9	Two series of scaling NW length-width dependences of Ni-catalyzed InGaN NW growth. The fitting curve is shown as a dashed line, and experimental data are shown as symbols. W_1 and W_2 represent the semipolar and *c*-plane width, respectively. The vertical length is measured from an InGaN thin film.	72
Figure 3.10	(a) 45°-tilted and top-view (inset) SEM images indicate that two NWs have enveloped each other during growth. The contribution on the side wall proceeds simultaneously with axial growth; (b) average base width of InGaN NWs as a function of growth time.	74
Figure 3.11	TEM images of an InGaN NW side wall after (a) 600 and (b) $1{,}200\ s$ of growth. There is a significant contribution in the lateral direction between 600 and $1{,}200\ s$.	75
Figure 3.12	Experimental results of NW vertical length and thin film thickness as a function of growth time. The fitting curve is shown as a dashed line, and experimental data are shown as symbols. The error bars represent the range in which all samples were measured.	76
Figure 3.13	(a) Growth rate along the <0001> and <$\underline{1}$101> directions as a function of growth time; (b) angle between two side wall facets {0001} and {$\underline{1}$101} as a function of growth time. Values were measured based on SEM images.	77
Figure 4.1	(a) CL spectra at 300 K (top) and PL spectra at 30 and 300 K (bottom) of InGaN NWs grown at $715℃$ with fixed 200 torr at 300 and 30 K. (b) SEM image (top) and CL spectra (bottom) at all wavelength emissions at 300 K.	81
Figure 4.2	(a) Cross-sectional SEM image, with the top view as an inset. (b) NW-scale CL spectra at $2.67\ eV$. (c) CL spectra at $2.06\ eV$. CL measured at 300 K.	82
Figure 4.3	TEM-EDS scan of InGaN NWs with (a) horizontal and (b) vertical scans. In composition from each scan point is shown at the bottom of (a) and (b). The scan spacing is $10\ nm$. (c) X-ray diffraction (XRD) of InGaN and GaN NWs.	84
Figure 4.4	(a) Ratio of bulk to localized-state emission for various	86

	V:III ratios. The inset shows PL spectra of three samples at 300 K. (b) integrated PL spectra as a function of 1,000/T. The red lines represents fitting curves, and experimental results are shown as symbols.	
Figure 4.5	(a) TRPL result at 10 K; (b) carrier lifetime, fit by Eq. 4.2, as a function of temperature between 10 and 300 K.	88
Figure 4.6	SEM images of InGaN NWs with growth temperature fixed at $715℃$, pressure fixed at $250\ torr$, and TMIn flow of (a) 5, (b) 20, (c) 40, and (d) 100 sccm, and another set with the same growth temperature, pressure fixed at $100\ torr$, and TMIn flow of (e) 50, (f) 100, (g) 200, and (h) 300 sccm. A control GaN NW sample (i) was grown at the same conditions (V/III ratio, temperature, carrier gas, N_2, and pressure at $250\ torr$).	90
Figure 4.7	(a) Schematic illustrating process flow. Picture 1: InGaN NW growth; Picture 2: conformal $200\ nm$ Cr deposited on NWs; Picture 3: spinning and coating of SPR 220 with $3\ \mu m$ thickness and etching by plasma until the tops of NWs are exposed; Picture 4: Cr etching by chemical solution and removal of SPR 220. (b) SEM image of stage 4, with a cross-sectional SEM image as the inset.	91
Figure 4.8	(a) PL of an InGaN NW at stages 1 and 4 in Fig. 3.2.2.1(a). PL intensity at stage 4 is five times the original intensity. (b) XRD of InGaN NW at stage 1 and of GaN NW. InGaN bulk band gap versus In composition is shown in the inset. In composition was calculated from XRD, and band gap was estimated from PL.	93
Figure 4.9	(a) Normalized XRD of InGaN NWs. In content was estimated from lattice constants. (b) SEM images of InGaN NWs at various In contents. (c) PL at stage 4 in Figure 3.2.2.1(a).	94
Figure 4.10	TEM images of (a) an InGaN NW sample at low magnification; (b) an InGaN NW side wall 500 nm away from substrate; (c) interface between InGaN and *r*-sapphire substrate. The NW growth direction is along the [11$\underline{2}$0] direction (*a*-plane), represented as g.	98
Figure 4.11	TEM images of (a) HAADF and low-magnification STEM images with focuses of (b) 0 and (c) -42 nm; (d) XEDS image from the NWs to the oxide layer.	99

Figure 4.12	TEM images of (a) HAADF and (b) close-up image of the NW tip region; (c) geometric phase analysis for a needlelike NW; (d) TEM image, with (e) an EDS line scan image from A to B.	101
Figure 5.1	(a) Absorption measurement setup; (b) absorption at various InGaN NW densities and of a control sample without NWs.	107
Figure 5.2	(a) Schematic of Schottky and Ohmic contacts; (b) overall diagram of InGaN solar cell device	108
Figure 5.3	(a) Schematic illustrating the fabrication process. Picture 1: InGaN NW growth to 1 μm on average; Picture 2: parylene spinning and coating to a 1.5 μm thickness and etching by plasma until the NW tops are exposed; Picture 3: metal deposition by 50 nm Pt/200 nm Au/1 μm Ag in sequence; Picture 4: lift-off substrate by the LLO process with a 248 nm pulse laser; Picture 5: removal of the bottom film by a dilute chemical solution; Picture 6: metal deposition with 10 nm MoO_2.	110
Figure 5.4	(a) I-V characteristics of InGaN NW samples with various incident light intensities; (b) current and power densities as a function of the applied voltage in scenario A.	111

LIST OF APPENDICES

Appendix A	Wurtzite Nitrides Structure	114
Appendix B	Parameters for III-nitrides	116

ABSTRACT

Wide-bandgap, nitride-based semiconductors have gained a lot of attention for optoelectronic devices (e.g. photovoltaics (PVs), light emitting diodes (LEDs), and laser diodes (LDs)) thanks to their remarkable material properties. However, due to lattice mismatch, most epitaxially grown InGaN-based devices are limited by the quality of the GaN layer and the total thickness of the InGaN layers that can be stacked on the substrate. These challenges seriously affect our ability to produce high performance optoelectronic devices.

The unique growth mechanism of nanowires can circumvent these issues by effectively relaxing the strain on lattice-mismatched substrate, thus allowing the growth of defect- and strain-free materials. First, we report the growth of *a*-plane GaN thin film on top of GaN nanowires by metal organic chemical vapor deposition (MOCVD). We analyzed the microstructural properties and the results showed that small-angle tilts and twists of the nanowires were the primary causes of defects in the top GaN films. To this end, we have developed a novel multi-stage growth process for coalesced nanowires to further improve the a-plane GaN film quality. Furthermore, defect-free vertically aligned bulk InGaN nanowires were achieved by MOCVD for the first time. The Indium composition in the InGaN alloy can be

continuously tuned from 0 to 19%, covering the blue and green part of the visible spectrum. Because of the significance of these wavelengths, our work has the potential to not only impact high power LEDs and LDs device but also enable efficient energy conversion in PVs applications.

CHAPTER 1

Introduction

1.1 InGaN Material

In the past two decades, III-Nitride based materials have been studied extensively and considered for use in semiconductor devices. Due to the fact that nitride-based compounds are wide band gap materials, these materials are chemically very stable, and have high heat capacity and thermal conductivity. Therefore, GaN transistors can operate at much higher temperatures and voltages than silicon transistors. In addition, nitride alloys have also been the subject of considerable interest for wide band gap optoelectronic semiconductor devices, since these compounds are capable of producing a wide range of emission wavelengths (from ultraviolet, visible to infrared). Nitride alloys are the only group of V-III compounds that has a direct optical band gap covering a wide range of emission energy. These properties of nitride-based materials make their applications very attractive both in optical and electrical semiconductor devices.

The band gap of InGaN alloy can be expressed with a constant linear term and a non-linear term according to the bowing parameter, E_b [1]. The value of the bowing parameter is dependent on indium composition, x. Eq. 1.1 shows the formula of InGaN band gap.

$$E_g^{AB} = E_g^A + \left(E_g^B - E_g^A\right)x + x(1-x)E_b \qquad (eq.\,1.1)$$

The left side of Eq. 1.1 describes the band gap of $In_xGa_{1-x}N$. On the right side, E_g^A, E_g^B, and E_b describe the band gap of GaN (3.4 eV), InN (0.7 eV), and the bowing parameter, 1.43 eV, respectively, and x represents InN alloy composition. As the formula indicates, the band gap of $In_xGa_{1-x}N$ can be tuned from 0.7 to 3.4 eV by tuning the indium composition. The range of emission energy from InGaN overlaps the entire visible spectrum. Because of the significance of these wavelengths, InGaN is considered a great candidate not only for high power light emitting diodes (LEDs) and Laser diodes (LDs) devices, but also for PVs applications since it enables efficient energy conversion.

Metalorganic chemical vapor deposition (MOCVD) and molecular beam epitaxy (MBE) system are typically used for epitaxial growth of III-V nitride material. Due to remaining technological challenges, the III-nitride material is still in its developing stages. The research described in this dissertation focuses on addressing some of these challenges related to material quality, including the lack of suitable

substrate, thermodynamic non-isotropic growth phenomenon, and high dislocation density in layers of MQWs. Contribution to solving/overcoming these challenges have a direct impact on successful applications of III-V nitride materials.

Nitride-based semiconductors are commonly used in high efficiency blue and green LEDs, and LDs [2]. Often, these InGaN multi-quantum-well (MQW) structures were grown on sapphire substrate. Due to the larger lattice mismatch (16% for GaN and 29% for InN on sapphire) and thermal mismatch (-34% for GaN and -100% for InN on sapphire) between epitaxial layer and sapphire, epitaxial growth of InGaN and GaN on sapphire substrates creates threading dislocations (TDs), and basal plane stacking faults. Although SiC and ZnO provide a better lattice match (3% for GaN on SiC and 2% for GaN on ZnO), similar dislocation densities have been shown with these materials. Point defects and threading dislocations are also caused by lattice mismatch of GaN- and InGaN-epitaxial layer during multi-quantum wells (MQWs) growth. Because of the strain introduced by lattice mismatch, the growth surface suffers an external force. The defects are generated where atoms tend to coalesce [3, 4] near the growth surface. A large number of defects and dislocations can be created in the growth of strained hetrostructures. High threading dislocation density in the range of $10^7 - 10^{10}\ cm^{-2}$ significantly impacts internal quantum efficiency (IQE) [5, 6, 7, 8], thus impacting device efficiency. Therefore, in order to produce high efficiency optical devices, it is very important to solve these defect issues. Furthermore, several studies have proposed that the low device efficiency is also mainly caused by defects in MQWs [9, 10, 11, 12, 13, 14]. These are the major

technological challenges of III-nitride LED devices, the lack of a defect-free substrate and low density of extended defects in MQWs.

III-nitride solar cell devices have been proposed and developed based on the LED technology. Since photovoltatic (PVs) devices are similar to LEDs in terms of material, structure, and operation power, it is possible to take benefits of the existing technical knowledge and experience learned from LEDs and apply them to PVs. Recently, InGaN have been used to develop high efficiency solar cells [15,16,17]. This is because the probability of absorbing a photon depends on absorption coefficient, and InGaN based material has higher absorption coefficients than Si material. InGaN requires an absorption layer $100 - 200\ nm$ thick [18,19] to absorb incident photons.

However, the applications of InGaN material in PVs face the same defect issues as in its LED applications. In a minority carrier device, such as a solar cell, the behavior of minority carriers in the bulk essentially is affected by the crystalline quality. Therefore, InGaN bulk solar cell has been limited to the thickness of absorption layer free of defects. However, defect density in absorption layer increases with higher indium composition due to increasing lattice mismatch.

In order to increase indium composition without generating defects, the multiple quantum well absorption layer has been used, with which the indium composition can reach 25 to 30 % [20,21,22]. With this method, it is possible to make solar cells with internal quantum efficiency up to 70%, external quantum efficiency up to 72%, and band gap about $3\ eV$. However, it remains a technical

challenge to reach the required band gap energy of 2.4 eV for an ideal 4-junctions solar cell. To extensively use nitride-based device, improving material crystalline perfection is the key. In the following section, other solutions that have been investigated are discussed in more details.

1.2 High GaN Film Quality using LEO and Core-shell Nanowires

Recently, laterally epitaxially overgrown (LEO) and core-shell GaN nanowires (NWs) structure have been investigated as shown in Figs. 1.3 (a) and (b), respectively. Those growth techniques have been gaining great interests in optoelectronic devices because those growth methods potentially provide a solution to improve GaN template quality. The concept of LEO is to create micro-structure masks, SiO_2, and selectively grown GaN structure in windows region. The mask provides an initial stage on which GaN grow laterally. Also, it limits accommodation of threading dislocations induced by lattice mismatch at interface of epitaxial layer and sapphire substrate. In many cases, the results of threading dislocation densities were gradually reduced in two to three orders. However, it also increased the complexity in fabrication flows, and increased device costs. In order to enable the development high quality GaN template, one-dimensional NW growth has been proposed.

NW can circumvent the defect issues by effectively relaxing the strain on lattice-mismatched substrate, thus allowing the growth of defect- and strain-free materials. Due to efficiently reducing threading dislocations and basal plane stacking faults in GaN layer, InGaN NW have gained great interests in optoelectronic devices. Several LEDs, LDs and PVs devices have been developed and characterized using NW geometry grown on sapphire and Si substrate [23]. The most common geometry of InGaN NWs consists of GaN NW cores and forms core-shell structure [24, 25, 26, 27, 28, 29] to make the devices. Compared to the planar structure, core-shell geometry not only provides dislocation-free epitaxial GaN layer, but also offers a larger surface area to grow MQWs that can enhance device efficiency. However, it is difficult to incorporate core-shell NW structures into a two-terminal electrical device. Thus, an (In)GaN NW axial growth opens a new direction that allows to supply high quality InGaN films and MQWs, and also simple integrated device.

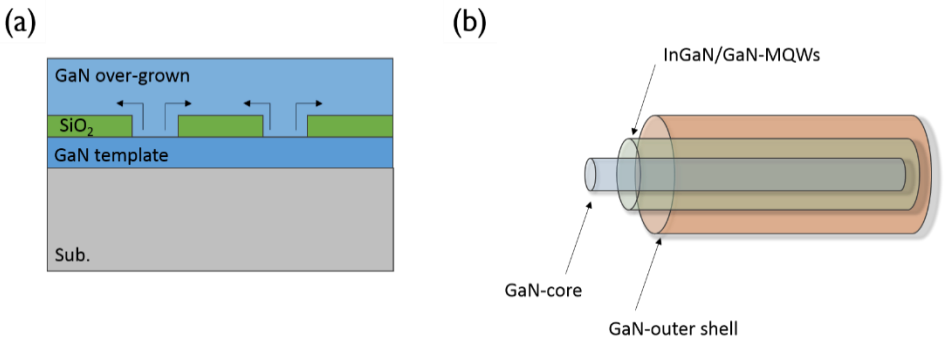

Figure 1.1: Schematic diagram of (a) GaN laterally epitaxially overgrown and (b) core-shell InGaN/GaN MQWs nanowires device

1.3 (In)GaN Axial Nanowires

Advantages of axial NW growth include low densities of extended defects and the relaxation of strain in lattice-mismatched substrate. This is because the interface strain caused by lattice mismatch between substrate and epitaxial layer could sufficiently release at NW region. Recently, high quality of GaN film was obtained using the vertically aligned NW as a template [30, 31]. Due to the strain free NW geometry, GaN NWs can be grown on varied substrates such as sapphire and Si substrate. Without considering lattice mismatch, GaN NWs do not consist of any threading dislocation and basal stacking faults. With following growth of aligned GaN NW array, a GaN film was grown on the upper part of NW. It turns out the GaN film was suspended by NWs. This growth technique confines threading dislocations at certain area, and leaves low defects in the film region. If those defects do not penetrate to MQWs or to film surface, they won't degrade device performance. An additional advantage of using NW template is offering a continuous growth process; therefore, it reduces complex fabrication flows to provide high quality GaN material.

Based on an optimization of the growth conditions, it could lead to extreme low extend defect density in non-polar GaN template. This NW-templated growth method can effectively provide high quality material and an economical template. Therefore, GaN NW-template growth method holds promise to provide a new direction of nitride based applications. Notably, we expect that in-depth

understanding of GaN NW-template growth method could further grow a high-quality non-polar GaN epitaxial film by decreasing anisotropy phenomenon.

InGaN MQWs grown over GaN NW eliminate both dislocation density in MQWs and GaN template. Therefore, it is possible to achieve high indium composition and tunable emission wavelength using a NW structure. These concepts make axial InGaN NW geometry particularly attractive as a potential geometry for LEDs, LDs and PVs devices. Furthermore, an axial geometry holds promise for the device fabrication [32]. Recently, NW diameter-dependent emission wavelengths that use InGaN/GaN MQWs in LED devices grown on *c*-plane sapphire substrate by MBE have been reported. [33]. By changing the NW diameters, researchers were able to control the confinement of electrons and holes, and thus the emission wavelengths. Based on these concepts, different diameters of NWs can be integrated into an array to build a white light LEDs device. However, the polar InGaN NW significantly degrade LED performance due to piezoelectric field induced at InGaN/GaN interface. The overlap integral of electron and hole envelope wave functions was decreased with induced piezoelectric field. Because of this disadvantage, InGaN-based NW LEDs and LDs device have not widely been used.

Furthermore, the axial InGaN NW geometry has only reported using MBE and CVD technique [34, 35, 36, 37, 38] but not in MOCVD system. This is because the growth condition of InGaN NW is quite similar and thus indistinguishable to that of thin film vapor epitaxial growth in MOCVD system. As a result, the growth conditions are unfavorable for getting axial growth only. However, III-nitride LED

industries have been widely developed based on MOCVD technology. Thus, bulk InGaN NW is important for further developed axial InGaN NW device.

1.4 High GaN Film Quality using Axial NWs

Material quality is one of the major challenges in nitride-based devices. The devices were grown in a non-polar nature (*a*-plane), exhibiting basal stacking faults (BSFs) as high as $10^6\ cm^{-2}$ and threading dislocations (TDs) as high as $10^{10}\ cm^{-2}$. These high defect densities are caused by an anti-symmetric crystalline structure and lattice mismatch between the epitaxial layer and substrate. However, diverse and in-depth studies of optimized growth conditions and novel growth techniques have been presented to achieve high-quality non-polar GaN films [39, 40, 41, 42, 43, 44].

A novel and promising growth technique using NWs as templates was recently employed to obtain high-quality GaN and ZnO films, which commonly accompanies vertically aligned, high-aspect-ratio, and strain-free NWs [45, 46, 47]. Such a NW array serves both foundation and strain-alleviating roles. The NW-bridged epitaxy high quality film is effective in terms of reducing the defect density and making the growth process simple and cost effective. Fig. 1.5 (a) shows the schematic diagram of device structure which was suspended by axial NWs. However, an in-depth understanding of NW growth and material properties is critical to

develop potential applications for nanoepitaxial devices. In the following, we will discuss the details of high-quality GaN thin-film growth in chapter 2.

Furthermore, in order to enhance LED output power, removing the low electrical and thermal conductivity of sapphire becomes an important topic. The most commonly used technique for removing sapphire substrate is laser liftoff process [48, 49]. In this technique, GaN based device was exposed to a high-power ultraviolet (UV) pulses laser directly. Under this illumination, the GaN interface layer can locally decompose into metallic gallium and nitrogen gas due to induce high temperature by laser. However, the heating process can be non-uniform over etching the wafer and cracked devices [50]. Typically, the diameter of NWs is in the range of hundred nm; therefore, using NWs as a template sufficiency allows for sapphire substrate liftoff without damaging wafer. In addition, using NWs device structure provides the method of vertical LEDs fabrication. Compared to lateral LED geometry, the vertical geometry can suppress the current crowing at the edge of LED device [51]. Hence, a vertical structure is a more promising method to offer a high power LEDs device. Fig. 1.5 (b) shows the configuration of LED chips via NWs template after liftoff of the substrate and deposit bottom and front contacts. The substrate lift-off process will be demonstrated in chapter 5. The method is good for implementing the high power vertical LED configuration via NWs GaN template.

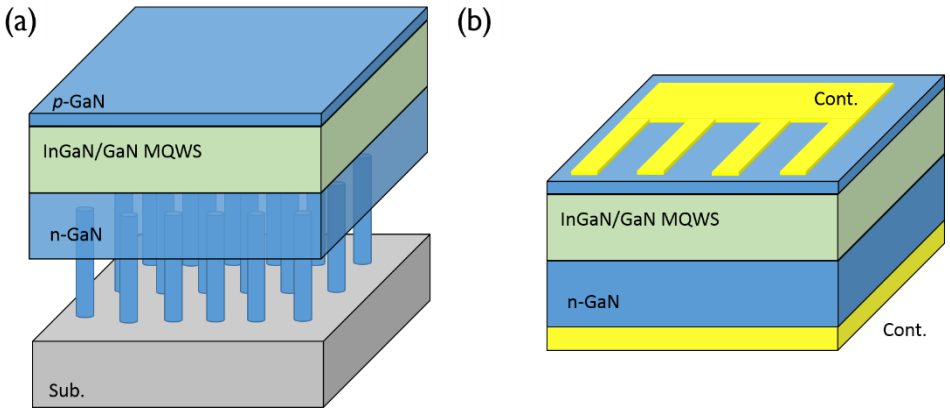

Figure 1.2: Schematic diagram of (a) LED devices under GaN NWs template structure and (b) substrate lift off and deposit contacts

1.5 Dissertation Overview

In summary, wide band gap, nitride-based semiconductors have gained a lot of attention for optoelectronic devices (e.g. PVs, LEDs, and LDs), because of their remarkable material properties. Most epitaxially grown InGaN-based devices are limited by the quality of the GaN layer and the total thickness of the InGaN layers that can be stacked on the substrate. This is mainly due to the high density of dislocations caused by different lattice constants and thermal expansion coefficients [52, 53, 54, 55, 56]. As a result, the number of threading dislocations, which tend to serve as non-radiative recombination centers in semiconductor, increases with the dramatic decrease in device efficiency. InGaN-based optoelectronic devices exhibit low external quantum efficiencies especially in the green and longer wavelength ranges [57, 58, 59].

Recently, many studies have analyzed the impacts of device performance in high quality material. Also, GaN core-shell structures have been demonstrated in applications in solid-state lighting and PVs. Based on previous studies, using (In)GaN NW as a template could possibly lead a new direction for achieving high indium composition with low defects InGaN epitaxial layer and high quality GaN thin film. In the following chapters we will focus on providing high quality a-plane GaN film and bulk InGaN NWs. Our work has the potential to not only impact high power LEDs and LDs device, but also enable efficient energy conversion in PVs applications.

CHAPTER 2

High-Quality GaN Thin Film Template*

A GaN film is grown on a GaN NW template, it can develop a low-defect density film and improve the anisotropy issues of a-plane non-polar GaN growth. Fig. 2.1 presents a schematic of an epitaxial GaN film on an *r*-plane sapphire substrate. The orientation of the *a*-plane GaN on *r*-plane sapphire was reported as $[0001]_{GaN}//[-1101]_{sapphire}$ and $[-1100]_{GaN}//[11-20]_{sapphire}$ [60]. In *a*-plane GaN growth, the growth rate of the *c*-direction is faster than that of the *m*-direction, resulting in anisotropic growth. This phenomenon causes triangular pits on the surface and serious issues in TDs and BSFs.

* A majority portion of the work described in this Chapter was jointly developed with Dr. Taesu Oh.

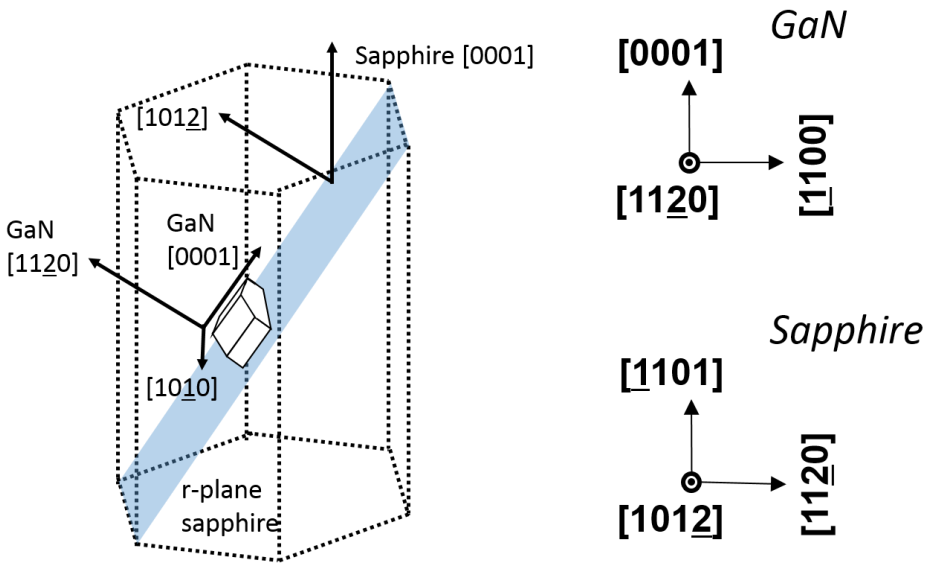

Figure 2.1: Schematic epitaxial growth of an *a*-plane GaN on *r*-plane sapphire, typically in the directions shown.

To develop high-quality crystalline GaN films, the structure design of the films is based on the work of George T. Wang *et al*. This novel technique is known as NW-templated lateral epitaxial growth. In this technique, an array of vertically aligned GaN NWs is first grown on a sapphire substrate via vapor-solid-solid (VSS) growth (*as described in Section 2.1*). A thick GaN film is then grown on top of the GaN NWs. The diameter of a GaN NW is sufficiently small to relieve the strain, so this epitaxial layer is free of dislocations. Thus, a GaN film on top of NWs can be expected to have a lower defect density than a GaN film grown on a sapphire substrate. Despite the initial success reported by Wang, detailed studies of the relationship between defect structures and NW growth conditions are still largely unknown. In this research, we will discuss this dependence and present methods to improve the materials quality.

This growth method includes the growth of GaN NWs and three main stages of GaN film growth, as shown in Fig. 2.2. The details of the growth conditions in each phase are provided below.

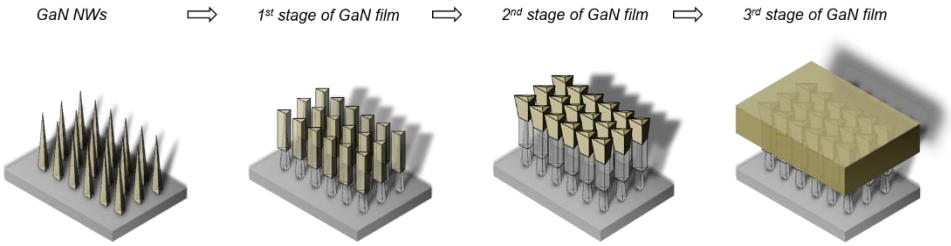

Figure 2.2: Schematic drawing of a GaN film on top of GaN NWs.

2.1 Vapor-Liquid-Solid and Vapor-Solid-Solid Growth Mechanisms

The vapor-liquid-solid (VLS) growth mechanism is an anisotropic crystal growth method for semiconductor nanowires (NWs). The method is commonly used for growing NWs, because it allows for the growth of NWs with very high aspect ratios and good controllability for the orientation and dimensions of NWs. The VLS growth mechanism was first demonstrated for the growth of a single crystalline silicon NW with diameter of 100 nm by Wagner and Ellis in 1964 [61].

Under the VLS growth mechanism, metal droplets are required as the seed to grow NWs. The material is dissolved into catalysts at certain growth conditions, and

the catalysts form a liquid alloy. When the liquid alloy reaches its super-saturation condition at a given temperature, its concentration will no longer increase. Therefore, a solid material will separate out at the interface between liquid and solid, which leads to nucleation and growth. Fig. 2.3 illustrates the VLS growth mechanism, which involves the absorption of a source material in vapor, solid, and liquid phases and promotes the elongation of the metal droplet into a NW. Direct observations of NW growth from gold nanoclusters by the VLS mechanism were recorded with in situ TEM by Yang *et al* [62]. The VLS growth mechanism implies a growth temperature above the eutectic point of the catalysts. If the growth temperature is less than the eutectic point of the catalysts, the metal droplet becomes a solid, and the growth mechanism is called the vapor-solid-solid (VSS) mechanism. Recent studies have reported the formation of III-V and II-VI NWs based on the VSS growth mechanism [63, 64, 65].

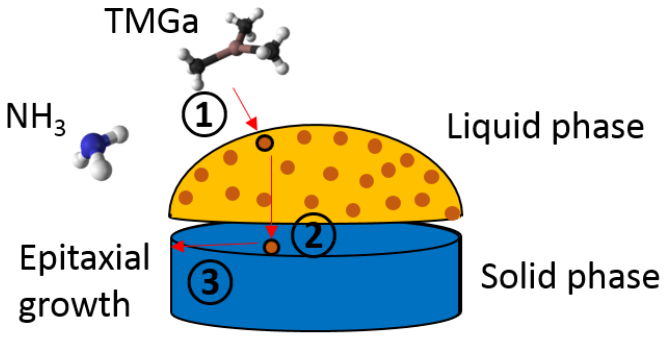

Figure 2.3: Schematic illustrating the growth of a NW by the VLS mechanism. Phase 1: atoms dissolve into catalyst. Phase 2: atoms separate out from catalyst. Phase 3: material deposits at interface.

2.2 GaN Film on GaN NWs

2.2.1 GaN NWs on Sapphire

To date, GaN NWs have generally been achieved as single-crystalline and dislocation-free structures by molecular beam epitaxy (MBE). This study considers the growth of large-scale and vertically aligned GaN NWs on *r*-plane sapphire by MOCVD.

Based on the VSS growth mechanism, GaN NW growth requires a catalyst. The Ni-catalyzed procedure is the same as the growth of InGaN NWs (*see chapter 3*). First, a $0.3\ nm$ Ni film is deposited on an *r*-plane sapphire substrate, and then, the Ni film is annealed in an MOCVD chamber for $900\ s$. Afterward, GaN NWs are grown via the VSS growth mechanism for $600\ s$. The growth temperature is 680℃, and the growth pressure is $200\ torr$. Our experimental results indicated that vertical GaN NWs depend on both the annealing and growth conditions. The growth conditions, such as growth temperature, pressure, carrier gas, and V:III ratio, influence the VSS growth window (*data not shown*). The length of the GaN NWs can be controlled by adjusting the growth time and catalyst size. In this study, we maintained constant NW growth conditions and Ni films but used various annealing conditions to control the NW density and alignment.

GaN NWs were grown on single-side-polished *r*-plane sapphire substrates at 680℃ in an H_2 environment for $600\ s$. On average, the length and diameter of the NWs were in the ranges of $3\ \mu m \pm 0.51\ nm$ and $50 \pm 14\ nm$, respectively. Fig. 2.4

presents the impacts of annealing time and temperature on the GaN NW surface morphology. We further investigated the correlation between the GaN NW surface morphology and annealing conditions.

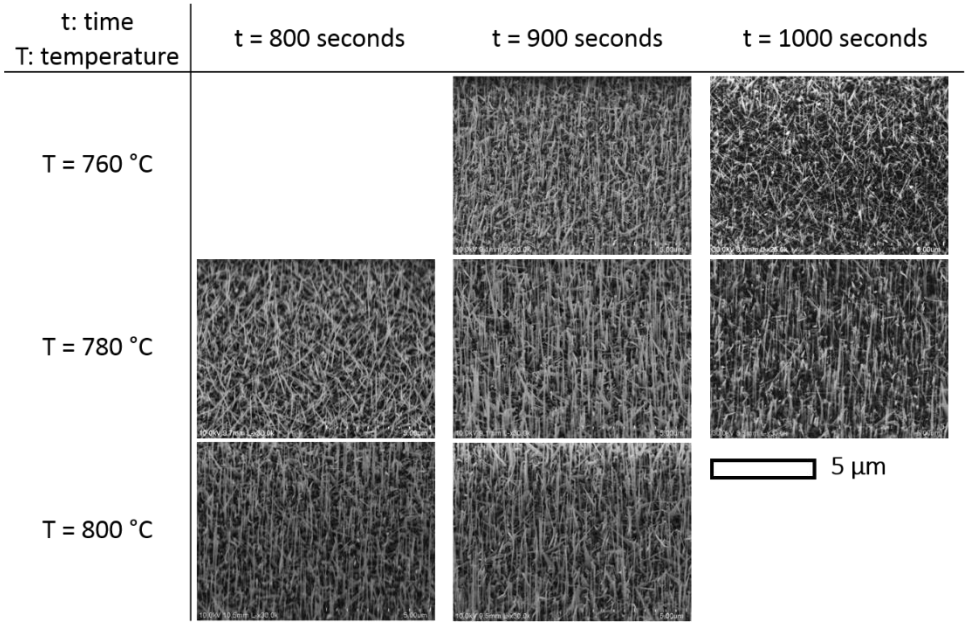

Figure 2.4: GaN NW series grown on *r*-plane sapphire substrates with various annealing conditions, time, and temperature. "T" represents the annealing temperature, and "t" represents the annealing time.

All 45°-tilted SEM images were collected at the center of each sample. The SEM images indicated that the annealing conditions can be used to sensitively tuning the NW density, orientation, and uniformity. High-degree alignments of NWs were found at relatively high substrate temperatures. Furthermore, the diameter of a NW varies with annealing time because the annealing time contributes to Ni adatom desorption and therefore affects catalyst size and uniformity as well as NW size and

density. With the most vertically aligned GaN NW, the catalyst has a diameter of 15 nm and height of 3 nm, determined by $2 \times 2\ \mu m^2$ AFM images.

These GaN NWs are considered the foundational supports for GaN films. To grow a thin film on top of NWs, GaN NWs with high density and wide diameter are preferred; however, these two parameters are difficult to achieve at high temperature. For this reason, we choose a reliable annealing time of $900\ s$ and an annealing temperature of $780°C$. These conditions promote the formation of vertically aligned GaN NWs with densities as high as $5 \times 10^{10}\ cm^{-2}$.

2.2.2 Tilted and Twisted GaN NWs

GaN NWs were grown on *r*-plane sapphire substrates with 15% lattice mismatch. Epitaxial layers require a certain thickness to release the strain accumulated at the interface. In initial growth, the strain may be critical to governing the orientation of GaN NWs. Based on SEM images, we discovered slightly tilted and in-plane twisted GaN NWs. These mis-orientation angles are defined with respect to certain directions, as shown in Figs. 2.5(a) and (b).

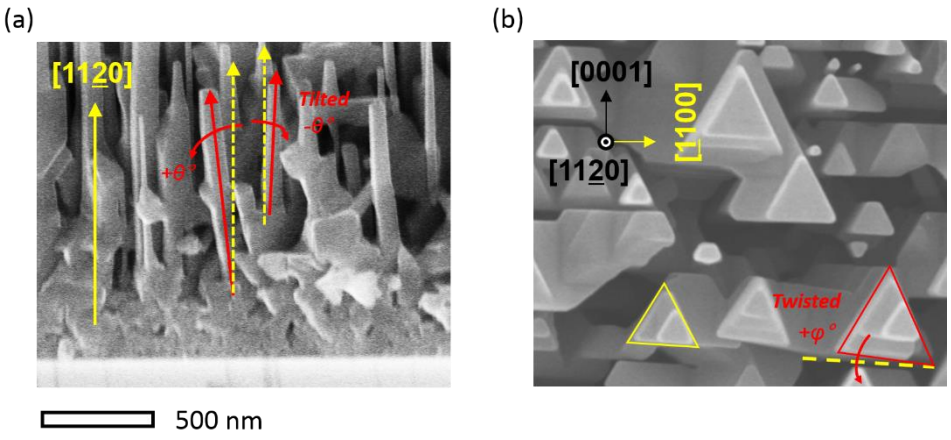

Figure 2.5: Slightly tilted and twisted NWs are observed in SEM images of the first stage of GaN film growth: (a) cross-sectional and (b) top-view images correlate to tilted and twisted NWs, respectively.

To estimate the distribution of mis-orientation angles, we analyzed the angles from cross-sectional and top-view SEM images. To minimize the measurement and observation errors, over 200 NWs were counted in each sample at random places. The histograms of tilted and twisted angles of mis-oriented GaN NWs are shown in Figs. 2.6(a) and (b), respectively. Based on the FWHM values from Gaussian fitting, we confirmed that the distribution of both mis-orientation angles was notably reduced with increasing NW density. According to the numerical analysis, the total amount of mis-oriented NWs are held constant. The proportion of mis-oriented GaN NWs is reduced with increasing total NW density. In particular, the mis-oriented NW percentage rapidly decreased in the $6.1 \times 10^{9}\ cm^{-2}$ NW sample. The average tilted and twisted angles were estimated to be 6 and 5.8°, respectively.

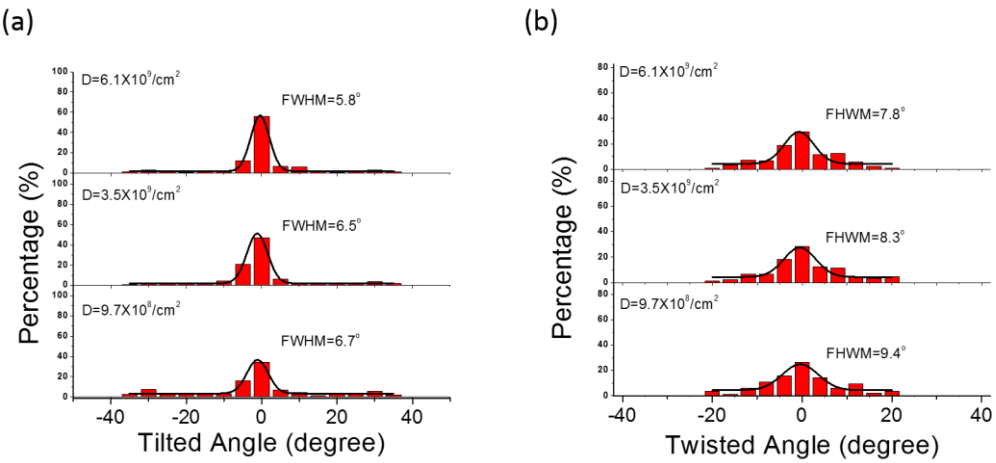

Figure 2.6: Histograms of (a) tilted and (b) twisted angle distributions of GaN NWs grown on *r*-plane sapphire substrates with various NW densities. The FWHMs of the NW distributions were estimated by fitting Gaussian functions (black lines).

The occurrence of tilted or in-plane twisted NWs could be related to the GaN NWs still experiencing strain at the beginning of growth. However, to explain this phenomenon, further investigation is needed in terms of the formation of an amorphous layer at the interface between the NW and substrate [66].

2.2.3 GaN Thin-Film Growth

The growth of GaN thin films on top of GaN NWs can be divided into three stages. The first stage is growth immediately above the GaN NWs, and the layer is grown during temperature ramping. The following layer in the second stage of GaN is grown at a stable intermediate temperature (900℃). Lateral growth dominates at the first and second stages, making the tops of NWs fully coalesce to each other. The third stage of GaN film growth continues to the formation of a planarized surface at

high temperature (1,100℃) and low pressure (60 $torr$). Epitaxial growth changes from three-dimensional (3D) to two-dimensional (2D) growth. In this study, each layer was characterized under different growth conditions and will be discussed in the following sections.

2.2.3.1 First and Second Stages of GaN Film Growth

Epitaxial growth at the first and second stages involves predominantly side wall growth. These stages are required to suppress VSS axial growth. From our experience, the VSS growth method is controlled by growth temperature and pressure. If the growth conditions are not within the VSS mechanism range, then VSS growth will not proceed. Therefore, our growth conditions were modified to meet these requirements. Under optimized growth conditions, the optimal result occurs at a growth temperature of 900℃ and growth pressure of 100 $torr$. The average diameter of GaN NWs before the first stage of GaN film growth was 50 nm. Therefore, NWs could easily decompose at high temperature. To prevent damage to NWs, TMGa and NH_3 precursors continually activated flowing during temperature ramping from 680 to 900℃. This ramping procedure requires 600 s and represents the first stage of GaN film growth. Subsequently, the second stage of growth proceeds at a stable temperature of 900℃ for 900 s. The second stage proceeds until all top NWs fully coalesce into a film. Thus, growth time depends on NW density. From our experience, the growth time of the second stage must increase to 1,200 s

for GaN NW density on the order of $10^8\ cm^{-2}$. A brief interface stage between the first and second stages occurs to reduce NH_3 flow and decrease growth pressure. This period only lasts for $30\ s$. Here, we can ignore the impact of this short period on the GaN film product. Ga adatoms diffusion length was reduced at a low pressure environment that allowing interrupted NW axial growths. Additionally, due to the ratio of Ga- to N-face growth rates being relatively different, it also can selectively overgrown on NWs sidewall (lateral growths) via controlling V:III ratio [67]. Ga-face toward {0001} faces which is the coalescence front at low V:III ratio conditions. In the second stage, the V:III ratio was decreased from 460 to 380 and the pressure was decreased from 200 to $100\ torr$ to enhance further the lateral growth rate.

Figs. 2.7(a) and (b) present 45°-tilted SEM images of the first and second stages of GaN growth, respectively. The insets are cross-sectional SEM images. The SEM images in Fig. 2.7(a) indicate that vertical length was suppressed and lateral epitaxial growth proceeded based on the changed growth parameters. Fig. 2.7(b) presents a coalesced film after lateral growth of 900 s. The inset of Fig. 2.7(b) clearly illustrates that the film was suspended by NWs. The surface reveals a mountain-like structure after the second stage of GaN film growth. The root mean squared (RMS) of surface roughness was estimated to be approximately $204\ nm$ in a $130 \times 130\ \mu m^2$ area by LEXT (Nomarski microscope). This mountain-like feature is mainly caused by the anisotropic growth rate toward different planes and the non-uniform length of GaN NWs. GaN NWs with triangular shapes have an anisotropic growth rate, and thus, side wall deposition is concentrated in the *c*-direction, [0001],

instead of the other two semipolar directions. Initially, the average GaN NW length is 3 μm, but the standard deviation is nearly 500 nm. The surface roughness must be further reduced for uniform GaN NW length and density.

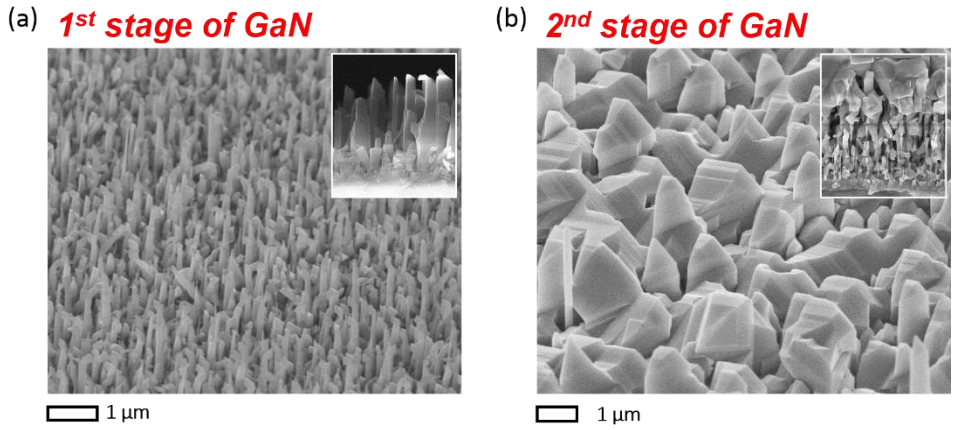

Figure 2.7: 45°-tilted and cross-sectional (inset) SEM images of the (a) first and (2) second stages of GaN growth. Part (a) illustrates a wire-like surface morphology, whereas (b) illustrates a film-like morphology.

2.2.3.2 Third Stage of GaN Thin-Film Growth

The GaN film exhibits a smooth surface by the end of the third stage. To perform 2D growth, the growth temperature rises to 1,100℃, the growth pressure decreases to 60 torr, and the V:III ratio decreases to 150. The SEM images indicated that GaN film growth on a NW template at higher temperatures, lower pressures, and lower V:III ratios significantly improves surface morphology (*not shown here*). Furthermore, we estimated the growth rate of GaN film as 2.5 μm/h from the cross-

sectional SEM images. The final thickness was approximately $5\ \mu m$ at the end of the experiment.

At the beginning of third-stage GaN growth, large islands coalesce to form a film-like surface. With continued growth, triangular pits appear on the film surface, implying incomplete formation. These pits are introduced by anisotropic growth along the *c*- and *m*-directions. The LEXT images in Figs. 2.8(a) to (c) present the GaN film grown on a NW template after 30, 60, and 120 min, respectively. Fig. 2.8(a) illustrates that there are several pits on the surface with different scales on the order of micrometers. Based on Figs. 2.8(b) and (c), although the pit size remains in the range of hundreds of nanometers, it is greatly reduced with increased growth time. To avoid these pits on the surface, a certain thickness is required for GaN to fully coalesce. RMSs of 134, 77, and $7\ nm$ are estimated by LEXT in a $130 \times 130\ \mu m^2$ area from Figs. 2.8(a) to (c), respectively. The surface morphology improves with increasing growth time. Figs. 2.8(c) and (d) present GaN films grown on a NW-template substrate and *r*-plane sapphire substrate, respectively. The surface of the GaN film grown on a NW template remains strip-like. RMSs of 7 and $16\ nm$ are estimated by LEXT in a $130 \times 130\ \mu m^2$ area from Figs. 2.8(c) and (d), respectively. Non-polar *a*-plane GaN on a NW template can compete with GaN film grown on an *r*-plane sapphire substrate.

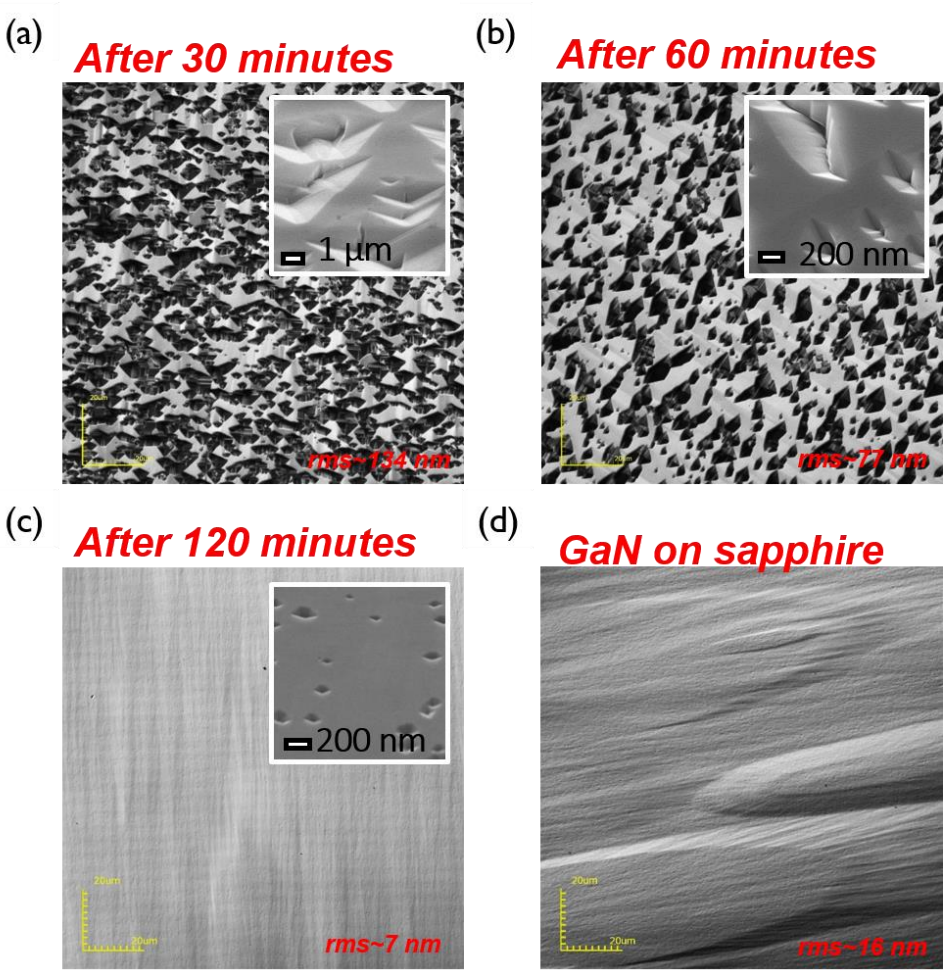

Figure 2.8: LEXT images of GaN atop a NW template at the third stage of growth, taken after (a) 30, (b) 60, and (c) 120 min. Image (d) shows a control sample of GaN on sapphire without NW as a base with 120 min of growth. RMSs were calculated from $130 \times 130\ \mu m^2$ LEXT images.

In addition, the quantity of defects and anisotropy effects were analyzed by XRD, and the results are discussed in chapter 2.2.3. Although the surface morphology is gradually improved, further optimization in each stage could eventually result in further reductions in the RMS.

2.2.4 Overview of GaN film on NW template

Fig. 2.9 presents a schematic of the key growth parameters in each stage. The solid line represents the actual precursor flow rate into the reactor, and the dashed line represents lack of flow into the reactor.

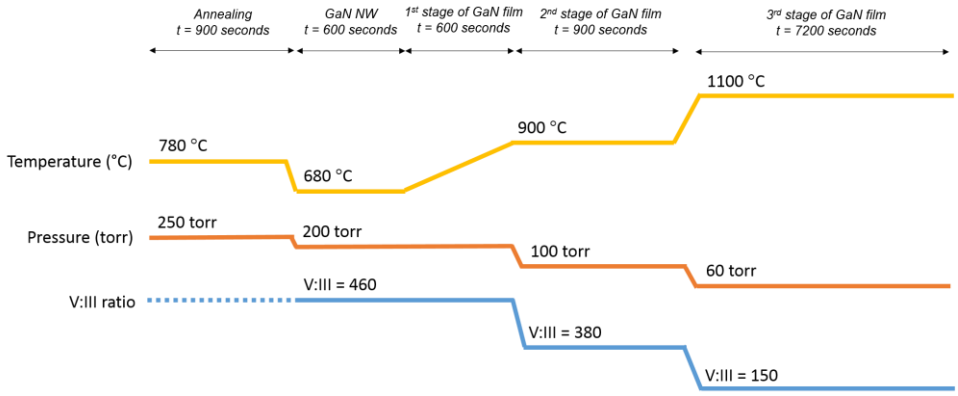

Figure 2.9: Schematic of the growth parameters (temperature, pressure, and V:III ratio) for GaN grown on a NW template at each stage.

In conclusion, the annealing conditions are critical factors to control of GaN NW density, orientation, and uniformity due to the sensitivity of Ni catalysts to annealing conditions. According to the numerical analysis, the number of tilted or in-plane twisted NWs is reduced with increasing total NW density. Mis-orientated NWs are likely caused by strain induced at the interface; however, this phenomenon requires further investigation.

We have demonstrated the epitaxial growth of suspended *a*-plane GaN film on Ni-catalyzed GaN NW structures by MOCVD. Fig. 2.10 presents a detailed sequence of the three major stages. The SEM images of each stage are shown in Fig.

2.10. In this growth method, we propose that the first growth stage of the GaN layer must be continually processed with increasing temperature. The second stage of GaN layer was grown at stable temperature, pressure, and V:III ratios until all NWs coalesced into a film. Because of the unique growth conditions, NWs no longer experienced axial growth according to the VSS growth mechanism. The key concept of the first and second stages of GaN is the activation of lateral epitaxial growth only. At the third stage, the GaN film was grown at high temperature, low pressure, and low V:III ratios with improved surface morphology. Afterward, an approximately 5 μm GaN layer was grown, with an RMS of 7 nm. Due to homoepitaxial growth, the GaN layer on top of NW exhibits more uniform crystals. Further details are provided in chapter 2.3.

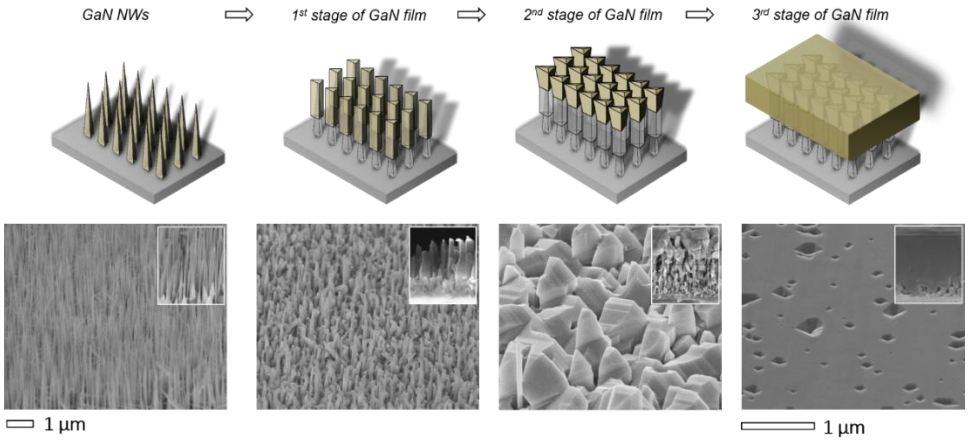

Figure 2.10: Schematic of the growth process of an *a*-plane GaN film on GaN NW/r-plane sapphire based on SEM observations. Picture 1: Ni-catalyzed GaN NWs on an r-sapphire substrate; Picture 2: first GaN nanostructures grown along GaN NW side walls; Picture 3: second stage of GaN layer growth; Picture 4: third stage of GaN growth with full coalescence. The insets are cross-sectional SEM images corresponding to each figure. All processes were carried out in an MOCVD reactor without any growth interruptions.

2.3 Results and Discussion

2.3.1 Strain Distribution of GaN NWs

Because GaN NWs have a small diameter, they may be able to efficiently relieve the epitaxial strain induced by lattice mismatch between the epitaxial layer and substrate. To confirm the lack of strain in GaN NWs, 2D finite-element analysis was performed by the semiconductor simulation software NEXTNANO. The simulation places the *m*-direction along the lateral axis and the *a*-direction along the vertical axis (*see Fig. 2.1*). Based on the lattice constants, lattice mismatch is approximately 15.4% for *a*-plane GaN NWs on an *r*-plane sapphire substrate.

Fig. 2.11(a) presents representative examples for the evaluation of the strain distribution in a GaN NW with a $100\ nm$ diameter. The presence of strain in a NW depends on its diameter; however, we only consider the average case of $100\ nm$ here. Color mapping indicates the ideal strain distribution inside a GaN NW and sapphire substrate. Fig. 2.11(b) presents the strain distribution at the center of a NW along the *a*-direction. Each curve represents the strain distribution at the center at various distances from the substrate. The spacing between each point between A and F is $10\ nm$; point D is right at the interface, and point G is $50\ nm$ away from the substrate. The maximum strain accumulates at the interface and decays to zero at approximately $50\ nm$ from the substrate considering a GaN NW with a diameter of $100\ nm$. In reality, a strain will not accumulate without forming any dislocation. In fact, once the epitaxial thickness exceeds the critical thickness, dislocation defects

will be formed to relieve elastic strain. The simulation results indicated that over-estimation of the NW length is required to release strain.

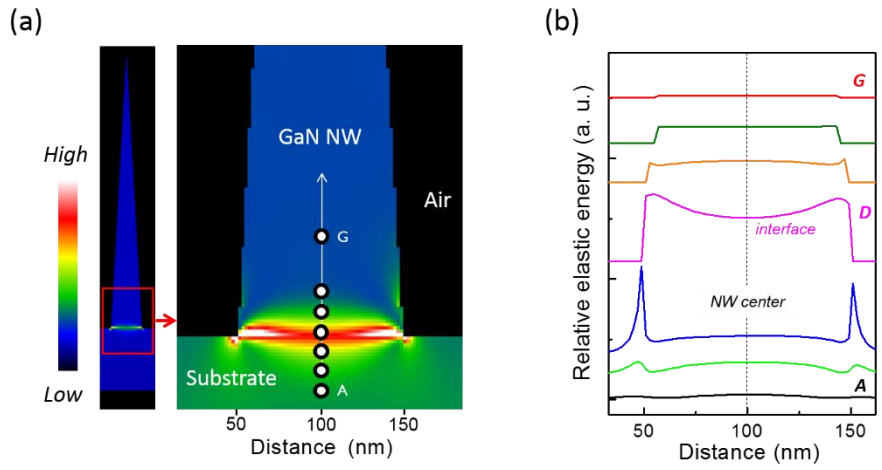

Figure 2.11: 2D strain simulation calculated by NEXTNANO: (a) color mapping of the strain distribution in a GaN NW on an r-plane sapphire substrate (assuming 15.4% lattice mismatch) and (b) relative elastic energy as a function of distance from the substrate. The spacing between each point is 10 *nm*; point A is 30 *nm* below the interface, and point G is 50 nm away from the interface.

To experimentally determine the presence of strain-free GaN NWs, room-temperature Raman scattering spectra were collected along the *c*- and *m*-axes. The spectra of GaN NWs are composed of several optical phonon modes, as shown in Fig. 2.12. In the figure, two Raman peaks appear at 568.6 and 532.7 cm^{-1}, which are assigned to the phonon modes of E_2 (high) and A_1 (TO), respectively. Based on Raman spectra analyses, we determined that these NWs experience no strain. However, a few broad peaks were recognized as impurities and defects. During the synthesis of NWs via the VSS growth mechanism, incorporation of Ni alloy and

other impurities into and mis-orientation of NWs affect their growth. These issues result in additional peaks in the Raman spectra.

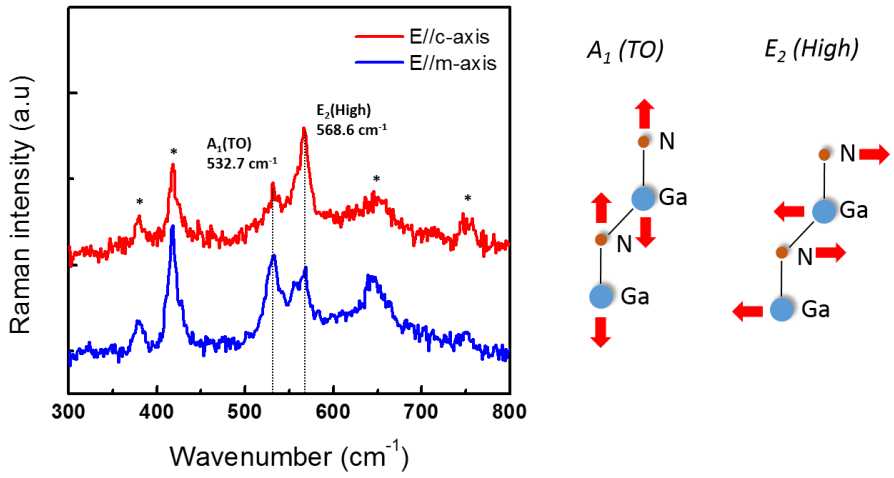

Figure 2.12: Raman spectra of a GaN NW sample grown on an r-plane sapphire substrate by Ni-catalyzed VSS growth. Two common strain-free frequencies, $A_1(TO)$ and $E_2(high)$, are shown on the left in Raman spectra measured along both the *c*- and *m*-axes. An illustration of these two frequencies is shown on the right.

2.3.2 Photoluminescence Study

Figs. 2.13(a) and (b) present the low-temperature (20 K) PL and SEM image of GaN film at each stage, respectively. From Gaussian curve fitting, we discovered three major emissions from GaN NWs that correspond to donor-acceptor pair (DAP), BSF, and near-bend edge (NBE) emissions at energies of 3.3, 3.43, and 3.47 eV, respectively. Based on the presence of DAP and BSF emissions, we anticipated that a number of defects, such as stacking faults, exist in the GaN NW growth stages.

The PL results indicated the presence of very weak NBE but intense BSF and DAP emissions in the NW sample. We eliminated the possibility that those emissions arise from the bottom GaN thin film because the DAP and BSF emissions still existed at the merging stage (second stage). These defect emissions were presumably caused by imperfections in GaN NW growth and/or impurities incorporated into the material during NW growth [68, 69].

NBE emissions are increased after the growth of a high-quality GaN film in the third stage; however, defect emissions remain obvious. Furthermore, there is a unique emission at $3.2\ eV$, LO_{DAP}, which appears only in the second and third stages of GaN film growth. According to previous studies, this emission is associated with excitons trapped by unidentified point defects at the dislocation for GaN films grown on a high-density NW-templated substrate; we found that LO_{DAP} emissions had a lower intensity than the GaN film on a low-density NW-templated substrate (*Data not shown*). Thus, we assigned this unique DAP emission to mis-orientation at the mis-aligned boundaries [70, 71].

Comparing the PL data of GaN on a NW template and GaN on sapphire, we found similar defect emissions from DAP, BSF, and NBE. The ratio of NBE to BEF emission intensities was calculated to quantify the optical properties of the film. Comparing the PL of GaN on sapphire and GaN on a NW template reveals slight increases in the ratio of NBE to BEF. Furthermore, GaN on a NW template has an island structure in the first and second stages. Those nanostructures involve a large number of mis-aligned boundaries formed by small tilted and twisted angles, which

are further discussed in chapter 2.3.5. Thus, the most promising way to further improve the optical properties of an *a*-plane film is to decrease the mis-oriented NW structure.

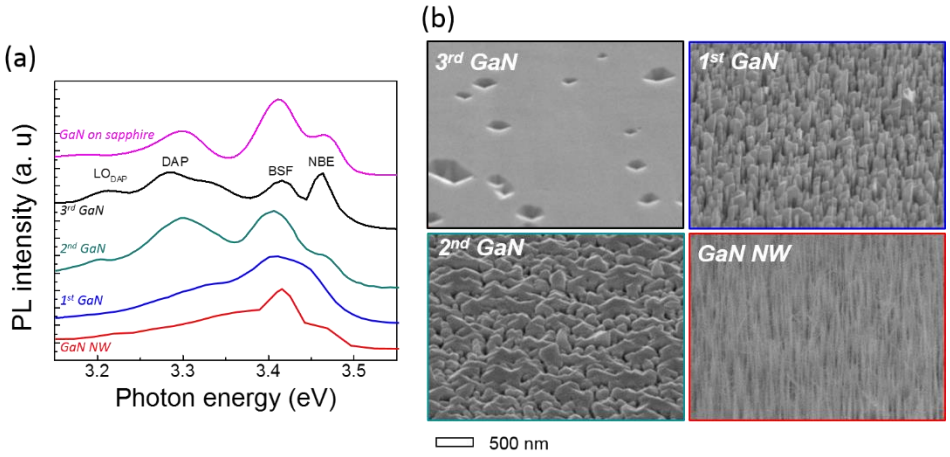

Figure 2.13: (a) low-temperature (20 K) PL and (b) SEM images of each stage of GaN film growth.

2.3.3 XRD Results

A high-resolution XRD rocking curve is employed to evaluate the structural quality and anisotropy of a-plane GaN layers. Figs. 2.14(a) and (b) present (1120) reflection omega rocking curves of the control sample, GaN on sapphire, and GaN on a NW template with various NW densities along the *c*- and *m*-directions, respectively. The FWHM values from Gaussian fitting of all samples on NW-templated substrates are smaller than those of the control sample, indicating improved GaN film quality. This result originates from a homoepitaxy-like approach

by introducing GaN NWs as a base. This growth structure could effectively decay the epitaxial strain from both lattice mismatch and thermal strain at the interface between the NW and sapphire [72, 73]. Therefore, GaN on a NW template may lead to improved crystalline quality.

In addition, because GaN on a NW template affords relatively symmetric growth in the *c*- and *m*-directions, this nanostructure provides a solution of anisotropic nature in an *a*-plane GaN film. XRD FWHMs as a function of azimuth angles are plotted in Fig. 2.14(c) to evaluate the material quality of *a*-plane GaN. The azimuth angles defined at 0 and 90° correspond to the GaN *c*-axis (0001) and *m*-axis ($10\underline{1}0$) directions, respectively. For GaN on a NW template, the FWHM of rocking for the *c*- and *m*-axes decreased with increasing NW density at all angles. Fig. 2.14(d) presents the FWHM difference compared to the control sample. The low FWHM value indicates improved crystalline quality.

Table 2.1 presents the FWHM values of all samples along the *c*- and *m*-directions. From the FWHM values in different directions, GaN on a NW template clearly exhibits more isotropic behavior than the control sample. The results reveal the improvement in the suppression of anisotropy in *a*-plane GaN by the NW template nanostructure.

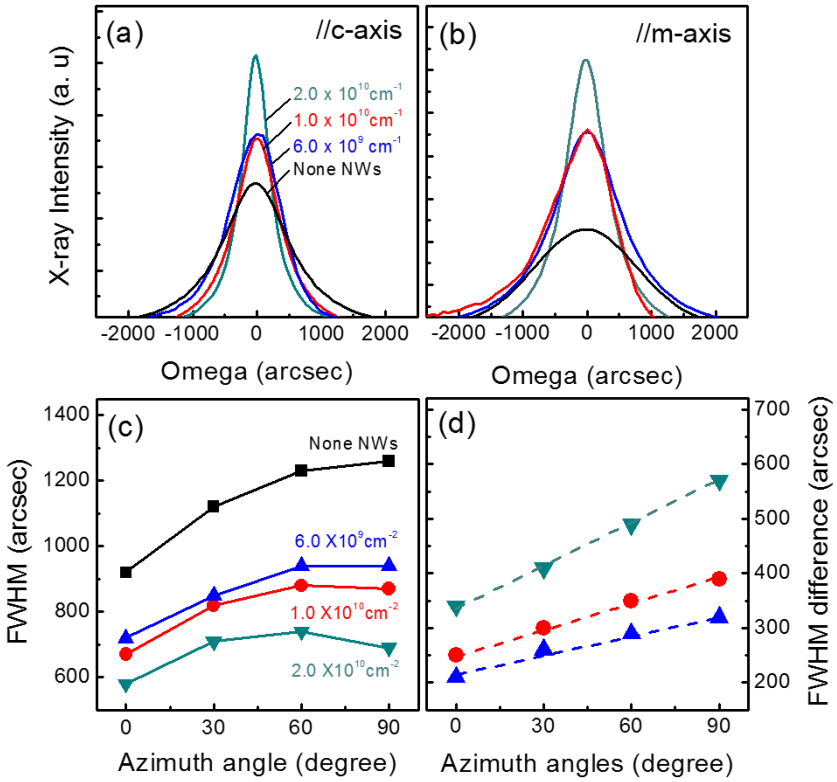

Figure 2.14: XRD of the (11$\underline{2}$0) reflection of *a*-plane GaN films grown on GaN NWs and reference GaN. (a) and (b) correspond to diffraction planes parallel to the *c*- and *m*-axes, respectively. (c) FWHM variation of the XRC for *a*-plane GaN films with the azimuth angle. (d) FWHM difference of *a*-plane GaN and a reference as a function of the azimuth angle. Dotted lines indicate linear fitting.

Table 2.1: FWHM of the (11$\underline{2}$0) reflection of *a*-plane GaN films grown on various NW densities and a control sample

	XRD ROCKING CURVE (ARCSEC)		
	// *c*-axis	// *m*-axis	$\frac{m-\text{axis}}{c-\text{axis}}$
CONTROL SAMPLE	920	1,260	1.37
GAN ON NW TEMPLATE $D = 6 \times 10^9\ cm^{-2}$	720	940	1.31
GAN ON NW TEMPLATE $D = 1 \times 10^{10}\ cm^{-2}$	670	870	1.30
GAN ON NW TEMPLATE $D = 2 \times 10^{10}\ cm^{-2}$	580	690	1.19

The different growth rate-induced crystallographic anisotropy in *a*-plane GaN can be improved by limiting the preferable growth direction [74]. The initial growth behavior along GaN NW side walls can limit preferable growth along the [000$\underline{1}$] direction through fast coalescence between GaN NW structures. This feature causes significant suppression of anisotropic crystallinity in *a*-plane GaN grown on NW structures. Therefore, the insertion of GaN NWs was expected to improve material crystallinity and significantly suppress structural anisotropy with respect to the in-plane orientation. Interestingly, both the crystallographic quality and anisotropy improved with increasing GaN NW density.

2.3.4 TEM Results

Another major advantage of GaN grown on a NW template is the material's low defect density and isotropic growth along the *c*- and *m*-axes. TEM and STEM were employed to investigate the microstructures to confirm the defect-free crystalline structure. Figs. 2.15(a) and (b) present STEM images from a sample after the first GaN growth stage and cross-sectional TEM images taken from a sample with GaN film grown on a GaN NW template, respectively.

Fig. 2.15(a) presents the initial GaN NW and the first stage of GaN film growth. From Fig., the initial NW exhibits dark contrast, and the first stage of GaN shows light contrast. Initially, NWs grown by the VSS growth approach do not exhibit defects. After introducing the first-stage GaN film, we discovered

dislocations with horizontal direction that were created during the first stage of GaN growth. Fig. 2.15(b) illustrates the high defect densities at the base of NWs, the coalesced region in the second stage, and the interface between the epitaxial layer and sapphire substrate.

Most dislocations are concentrated at the nanostructure merge region, which is indicated by the dark contrast in Fig. 2.15(b). Interestingly, these dislocations bend forward and end at the GaN NW side wall. Relatively few defects are observed compared to third-stage GaN films.

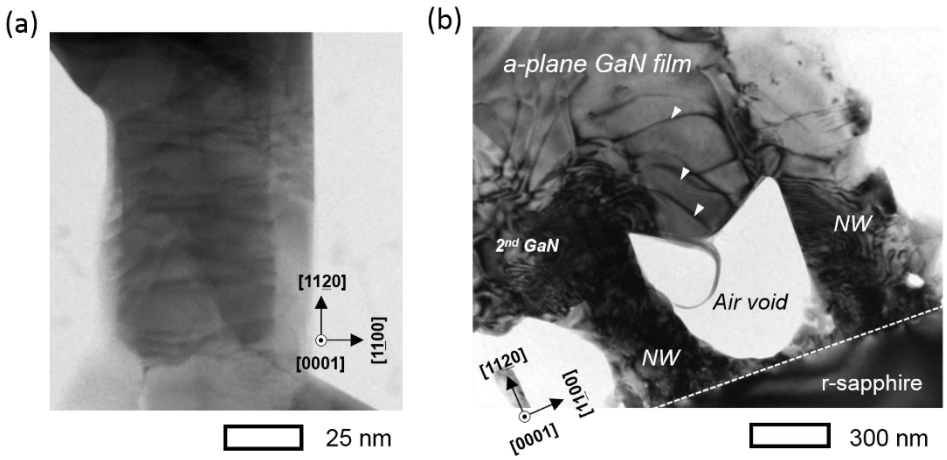

Figure 2.15: (a) STEM image of the GaN NW region. The contract line indicates the border area between the initial GaN NW and first-stage GaN nanostructure. (b) Low-magnification cross-sectional TEM image near the interface between GaN and the *r*-sapphire substrate.

Figs. 2.16(a) and (b) present high- and low-magnification TEM images after the first stage of GaN film growth, respectively. Fig. 2.16(a) presents a high-resolution STEM image focused at the merge region of two mis-oriented NWs. Based on indexing SAED patterns, the tilted angle of NW_B is estimated to be 8.5°,

with NW_A representing a vertical NW. At the overlapped region, a clear border line is formed, as indicated by a dashed line, which implies the existence of a mis-oriented boundary structure. Furthermore, there is a noticeable triangular offset of crystallographic orientation at the interface.

The low-magnification TEM image clearly illustrates that mis-oriented NW_1 merge with vertical NW_2, as shown in Fig. 2.16(b). Distinct boundary border lines are indicated by two red arrows. Based on the SAED patterns, the tilted angle in NW_1 was estimated to be 7°. When two NWs combine with each other, a new mis-oriented direction is created that influences the first and second GaN nanostructures. From the SAED pattern, a new mis-oriented direction results in a non-periodic diffraction pattern that is caused by highly disordered crystalline structures. Based on the SEM images, we observed mis-oriented NWs with tilt angles of nearly 30°; however, these mis-orientations were not detected in the TEM images. NWs with large mis-orientation impact the crystallographic orientation more significantly than those with small mis-orientation.

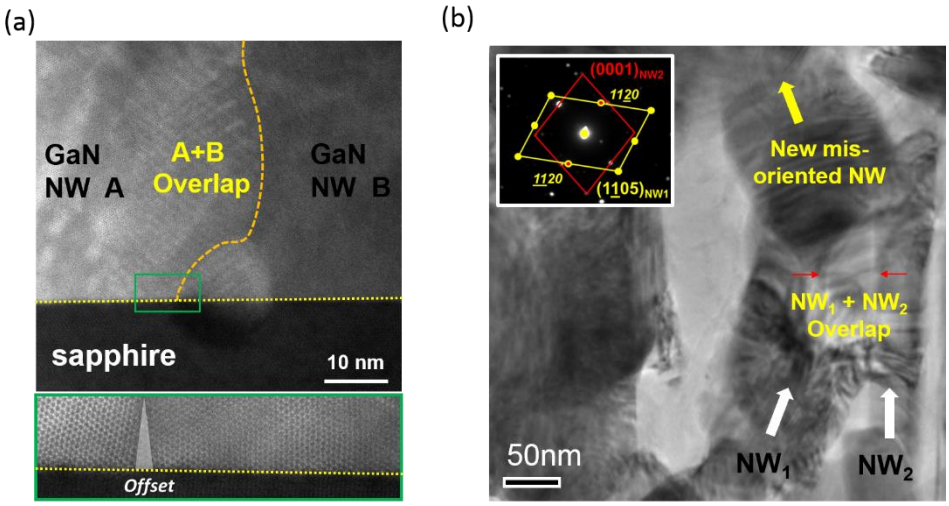

Figure 2.16: (a) STEM image of two GaN NWs overlapped near the interface region with the substrate; (b) STEM image of first-stage GaN NWs with small mis-orientation; SAED patterns taken from NW_1 and NW_2 are shown in the inset.

2.3.5 Extended Defects

In the SEM and TEM studies, we observed mis-oriented NWs with tilted and in-plane twisted angles during the first and second stages of GaN film growth. These mis-oriented NWs influenced crystallographic orientation and induced extended defect structures. XRD broadening indicates corrected evidence of defects caused by mis-oriented GaN NWs. As mentioned above, the number of tilted and twisted NWs is reduced with increasing total NW density. GaN formed on a NW template with high NW density has lower FWHM values than a sample with low NW density. In addition, the intense defect emission, LO_{DAP}, was only discovered in the GaN film sample under a highly mis-oriented GaN NW template.

GaN NWs were grown on commercial *r*-plane sapphire substrate. Under AFM image investigation, it shows ladder steps on polished surface with RMS roughness is 0.2 *nm* (*not shown here*). These steps structure caused mis-orientation phenomenon. To suppress this mis-orientation phenomenon, the GaN films have improved crystallographic orientations and optical properties.

The first type of extended defect structure is caused by tilted mis-oriented NWs. Fig. 2.17 presents a schematic of tilted NWs merging with vertical NWs. The extended defect structure can be generated at the boundary when two mis-aligned NWs merge with each other. This extended BSF defect could either end in a NW boundary or continue from the dislocation and end at the film surface. In reality, TEM confirmed that defects not only appear at the boundary but also surround the new NW where the two NWs converge. An example of the TEM image analysis of the merging region is discussed in section 2.3.4.

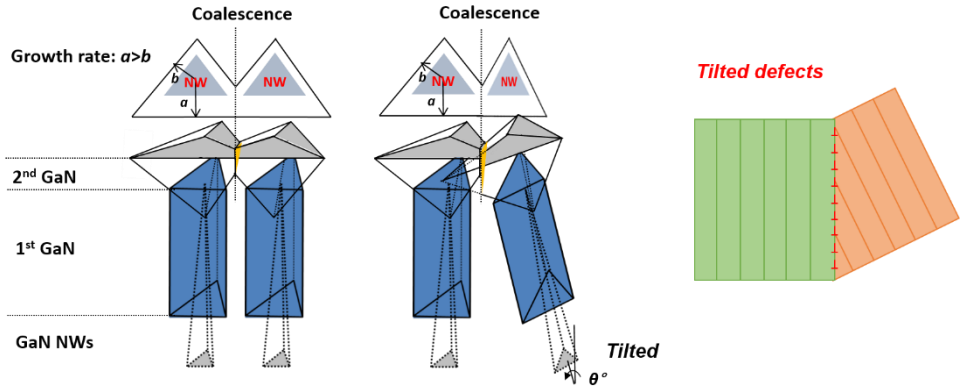

Figure 2.17: Schematic of two merged NWs. Tilted NWs can cause extended defects.

The second type of extended defect structure is caused by in-plane twisted mis-oriented NWs. Similar to the first type of defect, dislocation can be generated in localized regions when two NWs merge with each other but with a small difference angle. Fig. 2.18 presents a schematic of in-plane merging between twisted and non-twisted NWs. The predominant defects caused by crystallographic mis-orientations exist as a dislocation array and are frequently observed even in laterally grown GaN and GaAs systems [75, 76].

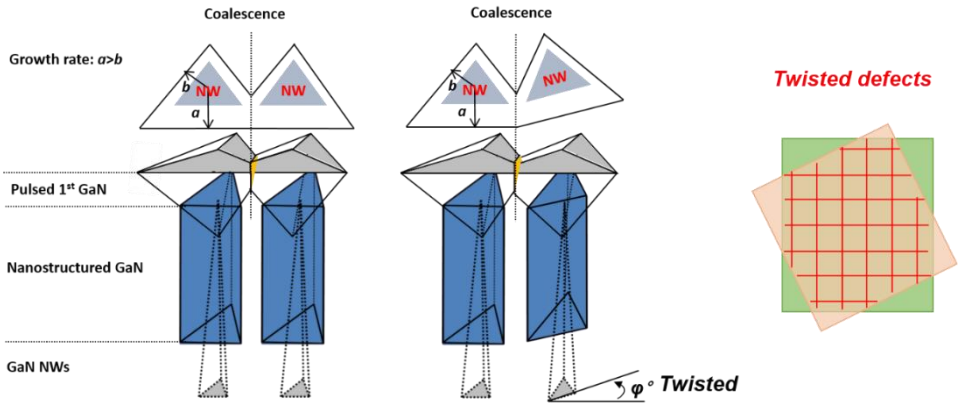

Figure 2.18: Schematic of two merged NWs. Twisted NWs can cause extended defects.

2.3.6 Overview of the Results and Discussion

In summary, NW-templated *a*-plane GaN film was grown and investigated by SEM, XRD, PL, and TEM. The simulations and experiments confirmed that GaN NWs grown by the VSS mechanism do not experience strain. Based on the PL results, point defects and impurity emissions are present in the second and third stages of GaN film growth. The DAP emission was enhanced at the nanostructure

merge stage (second stage) because of the highly tilted and twisted GaN NWs. The BSF emission gradually reduced between GaN on a NW template and GaN on a sapphire substrate. GaN film on a NW template had improved optical properties similar to those of a non-polar GaN film.

X-ray rocking curves indicated that NW-templated GaN had successfully reduced defect densities and suppressed anisotropy phenomena. Because the GaN film is suspended by NWs, the crystalline structure is influenced by the total GaN NW density and mis-orientated NWs. Imperfections during GaN NW growth can be further reduced and the anisotropy of *a*-plane GaN films can be further suppressed via improvement in the NW alignment. The TEM study confirmed that the mis-orientation of NWs significantly influences crystallographic orientation. Furthermore, most dislocations are concentrated at the merge region and end at the NW side wall. The relatively low defect density at the third stage of GaN film growth indicates the potential to realize high-quality GaN film by this growth method.

The properties of *a*-plane GaN films were predominately influenced by the proportion of mis-oriented NWs. Further suppression of the mis-orientation phenomenon can further improve the films in terms of both the crystallographic orientation and optical properties.

2.4 Multi-stack GaN Growth

We recently reported a high-quality bulk GaN layer formed on top of GaN NWs by MOCVD. The strain induced by lattice-mismatch between GaN NWs and the *r*-plane sapphire substrate causes some wires to have small tilted and in-plane twisted angles. We analyzed the micro-structural properties and discovered that this mis-orientation phenomenon degrades the quality of the GaN films.

In this section, we propose a new structure design to reduce the numbers of tilted and twisted NWs by growing GaN film in a multi-stack growth process. Fig. 2.19 presents the growth sequences in each stack. We grew the first stack GaN layer on top of GaN NWs on an *r*-plane sapphire substrate. We then grew the second stack GaN layer on top of the existing first stack GaN film. The second GaN NWs were grown on a high-quality GaN film, and thus, less strain was induced at the interface. Due to the lower strain between the second stack GaN NWs and first stack GaN film, we expect that the total numbers of tilted and twisted NWs decrease with the growth of multi-stacks, possibly decreasing the total number of imperfect GaN NWs by several orders of magnitude. Thus, the two-stack growth process can further improve the *a*-plane GaN film quality. With this structure design, we can further increase the number of stacks to improve the final *a*-plane GaN film. The results are discussed below.

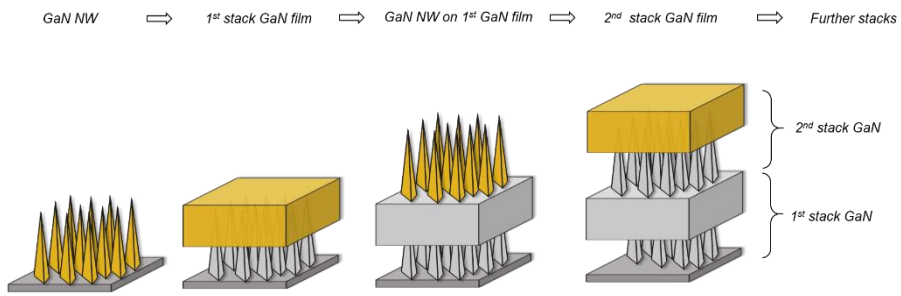

Figure 2.19: Schematic of GaN film grown on multi-stacks. Picture 1: GaN NWs on sapphire. Picture 2: first-stack GaN. Picture 3:GaN NWs on the first-stack GaN. Picture 4: second-stack GaN on NWs.

2.4.1 GaN NW Growth

GaN NWs were grown on *r*-plane sapphire after the deposition of 0.3 nm of Ni. The Ni film was annealed in an MOCVD chamber at 780℃ for 900 s; GaN NWs were then grown at 680℃ for 600 s. A GaN film is located at the bottom of the structure, and GaN could decompose at high temperature and react with Ni catalysts within a short period. Afterward, there are no Ni catalysts remaining as seeds for VSS NW growth. However, we can maintain a high GaN NW density if the annealing conditions are changed to a shorter time and NW growth conditions remain the same. Our experiment demonstrates that GaN films were decomposed at the annealing temperature and reacted with Ni more quickly than at lower temperatures. Hence, an annealed Ni film on a GaN film can be used for a shorter period than a Ni film on a sapphire substrate.

A series of GaN NW samples with various annealing times was prepared. The 45°-tilted SEM images present GaN NWs grown on a NW template for 600 s

with annealing times of 300, 180, 120, and 60 s, as shown in Figs. 2.20(a)-(d), respectively. In this study, we only varied the annealing time and held the other conditions constant. GaN NW density depends highly on the annealing time due to the annealing effect of Ni island size distribution and density. Understanding the correlation between Ni catalysts and annealing conditions requires further investigation. Here, we demonstrate that annealing at 680℃ for 60 s results in good alignment and highly dense NWs on the first-stack GaN template.

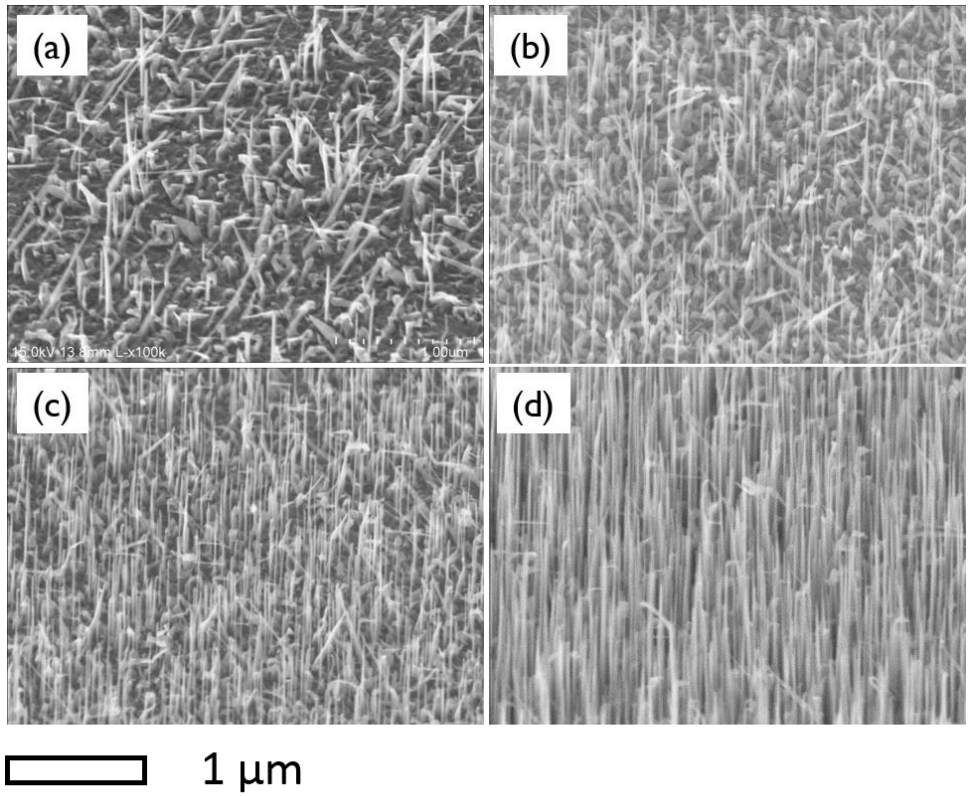

Figure 2.20: SEM images of GaN NWs grown on a first-stack GaN film with (a) 300, (b) 180, (c) 120, and (d) 60 s of annealing time. The other conditions are held constant.

2.4.2 Tilted and Twisted GaN NWs on Each Stack

We expected that the GaN NWs grown on a GaN film could reduce the distribution of slightly tilted and twisted NWs due to the lower amount of strain induced. Therefore, the degree of mis-orientation can decrease if GaN NWs are grown on multi-stack GaN. As a result, it is possible to have GaN film with less anisotropy by suspending highly vertical NWs. To confirm our concepts, the GaN NW distribution was estimated from SEM images. Again, hundreds of NWs were counted to eliminate measurement and observation errors.

Figs. 2.21(a) and (b) present the GaN NW distributions of tilted and twisted angle, respectively, on different stacks. Based on the FWHM values from Gaussian fitting, we were able to confirm that the distribution of both mis-orientation angles was notably reduced when the NWs were grown on multi-stacks.

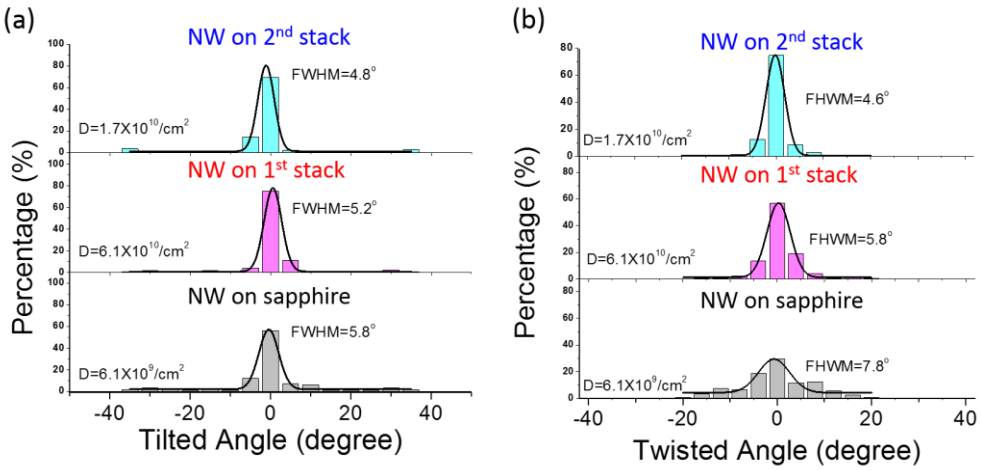

Figure 2.21: Histograms of (a) tilted and (b) twisted angle distribution of GaN NWs grown on each stack with various NW densities. The FWHM values of the NW distributions were estimated by fitting Gaussian functions (black lines).

Based on previous experience, the distribution of both mis-orientation angles is reduced with increasing NW density. We sought to confirm that this reduction of mis-orientation NWs is caused by growing NWs on multi-stack GaN rather than by the increased NW density. To this end, samples were grown with various NW densities on each stack. Figs. 2.22(a) and (b) present the tilted NW density as a function of total NW density and FWHM as a function of total NW density, respectively. Based on this analysis, both tilted and twisted distributions can be improved by NW growth on continued stacks.

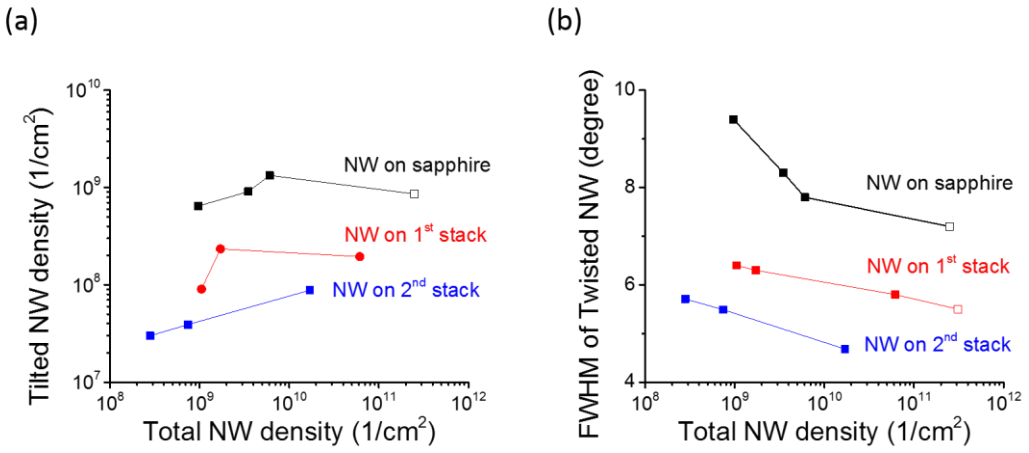

Figure 2.22: (a) Tilted NW density and (b) FWHM of the twisted angle as a function of total GaN NW density grown on each stack.

2.4.3 Second- and Third-stack GaN Growth

A GaN film was grown on top of NWs using the same growth conditions as the first-stack GaN but proceeding to the third stage of GaN film growth. Three major growth stages were processed via temperature ramping, middle-high, and high temperatures for the first, second, and third stages of GaN film growth, respectively. The first and second stages involved predominantly lateral growth to suspend the film, and the third stage involved a 2D growth mode to improve surface morphology (*see section 2.2.3*). In this multi-stack growth study, cover-free NWs could be destroyed by high temperature. The first-stack GaN NWs (NWs on sapphire) are largely unable to survive after multi-stack growth. Thus, the film collapses at the edge, and the film size shrinks. Particularly, almost all GaN NWs grown on sapphire decomposed during the third stack growth. Therefore, in this study, the growth time decreased from 7,200 to 1,800 s at the third stage of GaN film growth of each stack and in the control sample. A schematic of the growth sequence in each stage is provided in the conclusion section (*see Fig. 2.26*).

Because the GaN layer is only processed for $1{,}800\ s$ at high temperature ($1{,}100℃$), the surface has not yet fully coalesced. Several pit features were discovered on the surface after growth. Figs. 2.23(a) to (d) present LEXT images of the control sample, GaN on sapphire, and GaN on a NW template, respectively, of the first to third stacks. Figs. 2.23(a) and (b) reveal several pits on the surface at the micrometer scale. The pit size on the surface of first stack GaN is considerably larger than that of the control sample. Thus, GaN on a NW template requires a thicker film

to fully coalesce than GaN on an *r*-plane sapphire substrate. The second-stack GaN film revealed some gentle ramps on the surface, as shown in Fig. 2.23(c). Furthermore, the third-stack GaN displayed reduced roughness, as shown in Fig. 2.23(d). RMSs of $34, 68, 15,$ and $5\ nm$ are estimated by LEXT in a $10 \times 10\ \mu m^2$ area from Figs. 2.23(a) to (d), respectively. These values were taken from the smoothest region on each sample. In general, the surface roughness of a GaN film can be improved with the multi-stack growth technique. Further optimization of the growth time to reduce pit size without damaging GaN NWs could further reduce the surface roughness.

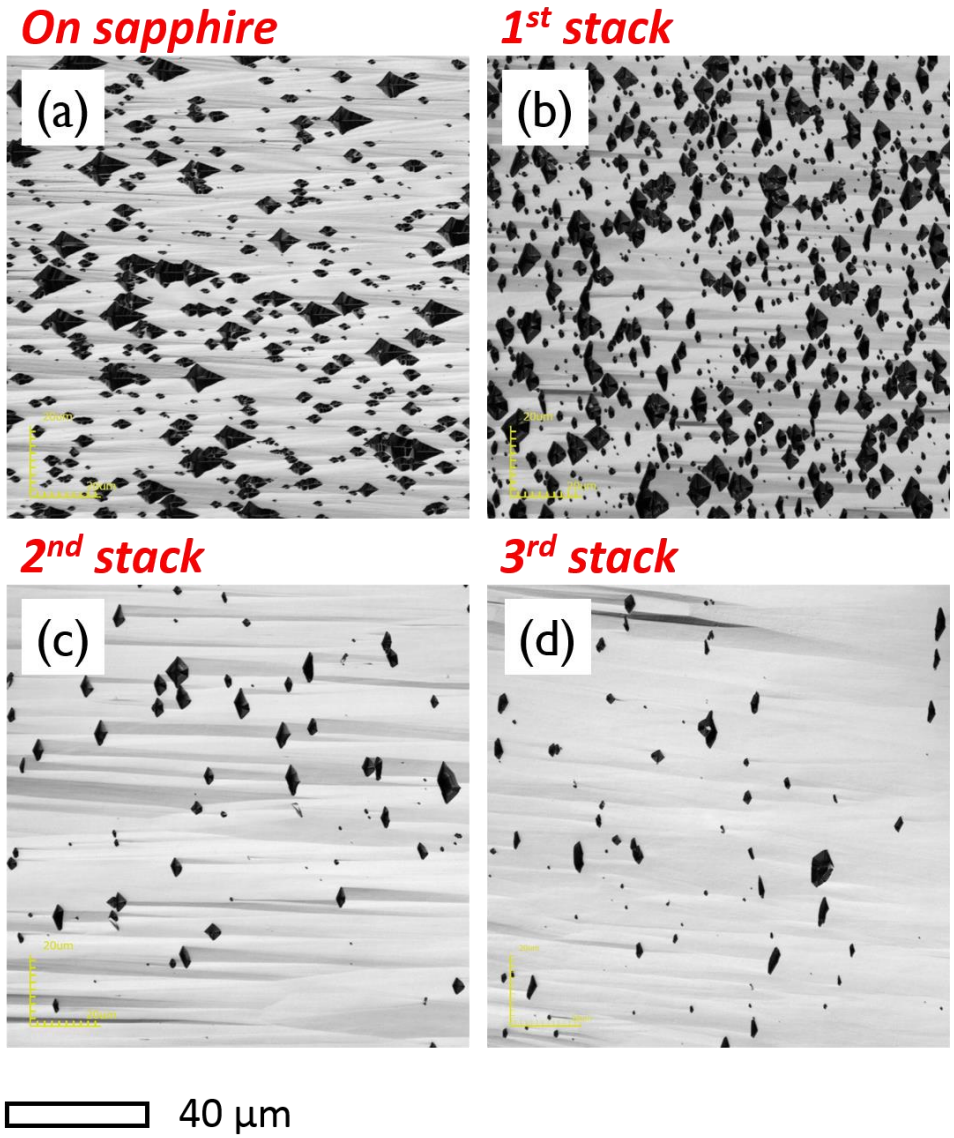

Figure 2.23: LEXT images were taken from (a) GaN on sapphire, (b) first-stack GaN on a NW template, (c) second-stack GaN on a NW template, and (d) third-stack GaN on a NW template

2.4.4 XRD Results for Different Stacks

The commercial GaN film grown on an *r*-plane sapphire exhibits anti-symmetric growth along the *c*-and *m*-axes, causing a difference in the XRD rocking curves in these two directions. In previous results, GaN grown on a NW template displayed improving the anisotropy phenomenon. However, the high order of mis-oriented GaN NWs degraded the film performance. To achieve better film quality, a GaN film was grown on the NW template of each stack and investigated by XRD. Without considering lattice mismatch between GaN NWs and GaN film, we could reduce mis-oriented tilting and twisting angles. Therefore, we expect that this film exhibits reduced anisotropy. Furthermore, because film coalescence is incomplete after less than 1,800 s, we also expect the FWHM of XRD rocking curves to be larger than in previous results (*see section 2.3.3*).

Figs. 2.24(a) and (b) present (11$\underline{2}$0) reflection omega rocking curves of the control sample, GaN on sapphire, and GaN on a NW template with various stacks along the *c*- and *m*-directions, respectively. The azimuth angles measured toward 0 and 90° correspond to the GaN *c*-axis (0001) and *m*-axis (10$\underline{1}$0) directions, respectively. Based on Gaussian fitting, the samples under NW-templated substrates exhibit smaller values than the control sample at all azimuth angles, as shown in Fig. 2.24(c). Figure 2.24(d) illustrates the difference in the FWHM of multi-stack GaN on a NW template compared to the control sample.

In addition, Table 2.2 provides the FWHM values of all samples along the *c*- and *m*-directions. From the table, GaN on a NW template with multi-stacks exhibits

considerably improvement compared to the control sample, particularly in the *m*-axis ($10\underline{1}0$) directions. The third-stack GaN on a NW template exhibits more isotropic growth than the control sample. The FWHM ratio of the *m*-axis to the *c*-axis is close to 1.1, and the difference at those two directions remains at $72\ arcsec$. The results suggest the improvement in suppression of anisotropy in *a*-plane GaN film growth by a NW template with this multi-stack method.

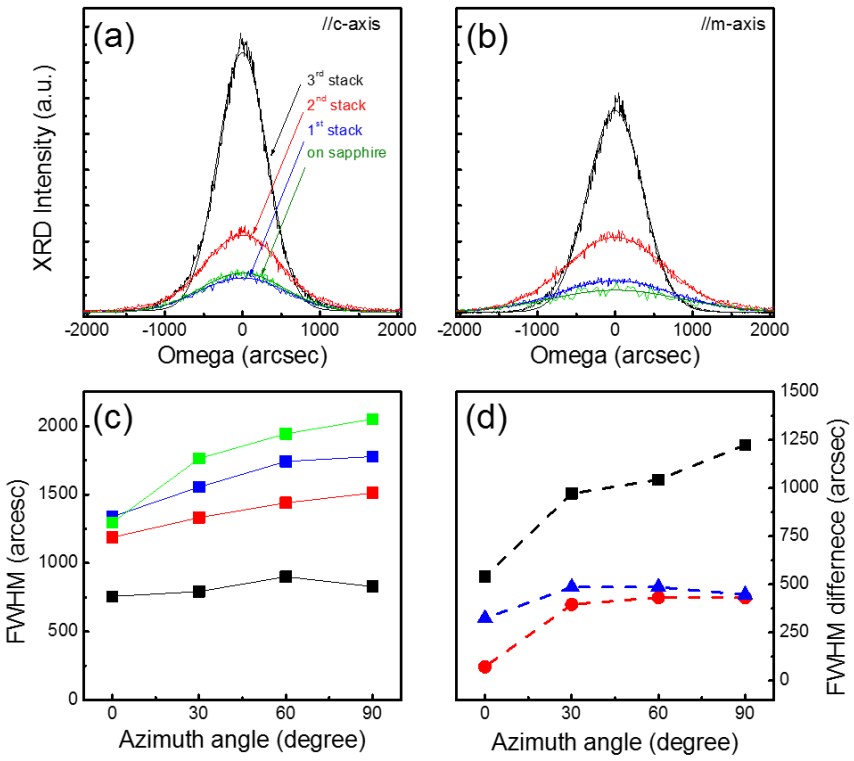

Figure 2.24: XRD of the ($11\underline{2}0$) reflection of *a*-plane multi-stack GaN films grown on GaN NWs and the reference GaN. (a) and (b) correspond to diffraction planes parallel to the *c*- and *m*-axes, respectively. (c) FWHM variation of the XRC for *a*-plane GaN films with the azimuth angle. (d) FWHM differences of *a*-plane GaN and that of a reference as a function of the azimuth angle. The dotted lines indicate linear fitting.

Table 2.2:FWHM values of the (11$\underline{2}$0) reflection of *a*-plane GaN films grown on various NW densities and a control sample

	XRD ROCKING CURVE (ARCSEC)		
	// *c*-axis	// *m*-axis	$\frac{m-\text{axis}}{c-\text{axis}}$
CONTROL SAMPLE	1,296	2,052	1.58
GAN ON THE NW TEMPLATE ***First stack***	1,340	1,778	1.32
GAN ON THE NW TEMPLATE ***Second stack***	1,188	1,512	1.27
GAN ON THE NW TEMPLATE ***Third stack***	756	828	1.09

2.4.5 Estimation of Anisotropy with Various NW Densities

In natural *a*-plane GaN growth, the growth rate on the *c*-axis is faster than that on the *m*-axis. Therefore, most dislocations are induced in the *m*-direction during film coalescence, leading to larger FWHM values from XRD in the *m*-direction than in the *c*-direction. Multi-stack growth of GaN on a NW template has been confirmed to reduce the degree of anisotropy. Based on various NW densities on each stack, we could further estimate the roles of NW density and multi-stacks in this reduction in anisotropy. First, we estimated the degree of anisotropy based on the ratio of FWHM and the other azimuth angles to the *m*-directions. If the ratio is close to one, *a*-plane GaN growth is nearly isotropic. Figs. 2.25(a)-(d) present the GaN film's FWHM

ratio value of the *m*-axis to the *c*-axis on different stacks with various NW densities. The FWHM values are estimated based on experimental results of the film grown on a NW template on each stack, as shown in Fig. 2.23 and Table 2.2. The FWHM ratio of the *m*-axis to the *c*-axis was clearly reduced by GaN grown on further stacks and high-density NWs. Multi-stack GaN exhibits a significantly lower degree of anisotropy than the control sample.

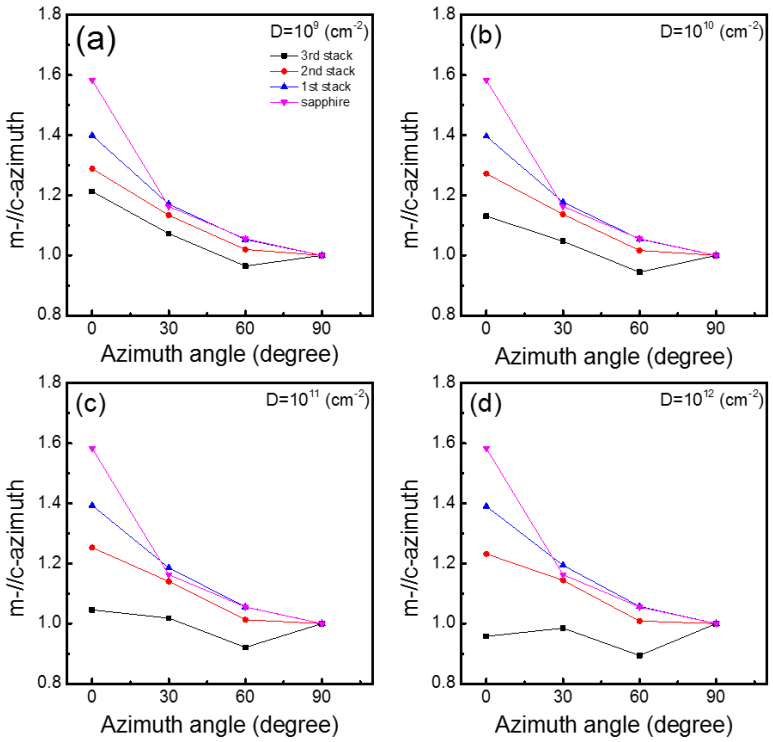

Figure 2.25: Estimation of the FWHM ratio of the *m*-axis to the *c*-axis for each stack with various NW densities.

2.4.6 Overview of Multi-Stack GaN Growth

Multi-stack GaN exhibits an improved surface morphology and lower degree of anisotropy compared to the control sample. The growth conditions of the first stack are discussed above (*see section 2.2.4*). Fig. 2.26 presents a schematic of the growth conditions for the second and third stacks.

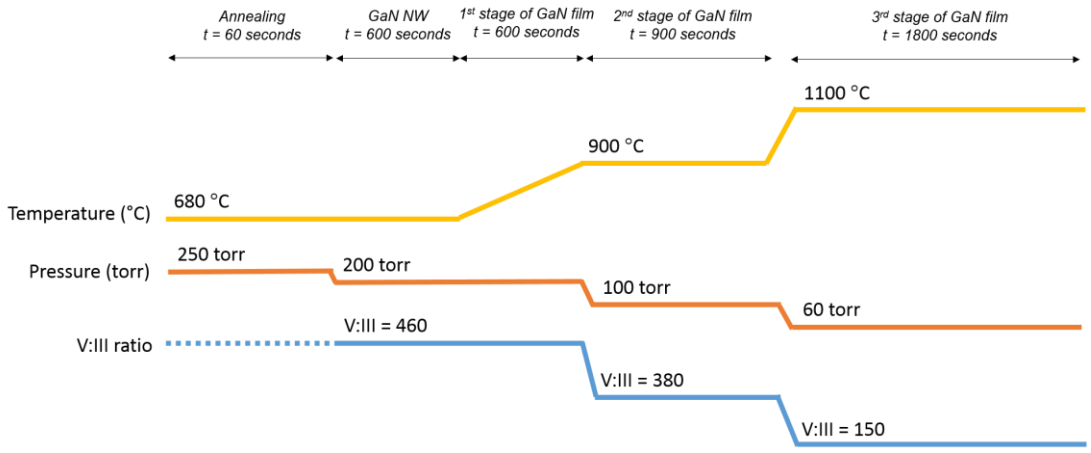

Figure 2.26: Schematic of the growth parameters (temperature, pressure, and V:III ratio) for multi-stack GaN grown on a NW template.

In conclusion, multi-stack GaN grown on a NW template has been realized. Based on the distributions of tilted and twisted angles, NWs grown on multiple stacks exhibit fewer mis-oriented NWs, perhaps because less strain is induced at the interface between the GaN NWs and film. Based on this multi-stack GaN study, the degree of anisotropy is reduced considerable. In particular, nearly homoepitaxial growth at all azimuth angles is observed at the third GaN film on a NW template. However, the surface morphology cannot be further improved because GaN NWs do

not have a long lifetime at high temperatures. Additional investigations regarding methods to protect NWs at high temperatures are necessary.

2.5 Summary

In this chapter, we demonstrated growth of high-quality *a*-plane GaN on a NW template. In the demonstration, we grew GaN NWs on an *r*-plane sapphire substrate and then grew GaN film on top of the NWs. Based on TEM results, we discovered that most defects were confined at the NW region and first stage of GaN film. Relatively few defects and a smooth surface film were observed at the end of GaN film growth. From XRD, significant improvement in crystalline perfection is found along both *c*- and *m*-axes, resulting in homoepitaxial growth. Based on further investigation, we found that mis-oriented GaN NWs contribute significantly to degradation of film quality.

To reduce these mis-oriented GaN NWs, we grew GaN NWs on multi-stack GaN NW-templated film. Due to the lower strain induced at the interface, we expected the small-angle tilted and twisted phenomena to be improved. According to histograms of tilted and twisted angle distributions of GaN NWs on each stack, we found reduction of mis-oriented GaN NWs as GaN NWs were grown on further stacks. Under appropriate growth conditions, multi-stack GaN film was further grown. We observed that *a*-plane GaN film on multi-stack GaN shows remarkable enhancement in isotropic growth. However, because GaN NWs do not last long at

high temperatures, surface morphology cannot be improved further. A tradeoff situation between the anisotropic phenomenon and surface morphology was found in this multi-stack growth study.

CHAPTER 3

InGaN NW Growth by MOCVD

3.1 InGaN NW Growth

3.1.1 Surface Morphology Control Experiment

We use *r*-plane ($1\underline{1}02$) sapphire substrates in this study because this orientation allows vertically aligned (In)GaN NWs to be grown epitaxially. First, a $0.3\ nm$ nickel (Ni) thin film was deposited on the substrate by vacuum thermal evaporation at a pressure of $1.8 \times 10^{-6}\ torr$ and then annealed at 780℃ and $400\ torr$ in an MOCVD reactor (Thomas swan:closed coupled showerhead 3×2) for $900\ s$. Based on AFM images as shown in Fig. 3.4.1, the surface was covered with Ni catalysts with diameter of $14.6 \pm 2.5\ nm$ at a density of $3.8 \times 10^{12}/cm^2$. Based on growth temperature at around 700℃, Ni-Ga solid solution formed Ni_3Ga phase [77]. The InGaN NWs were synthesized by the VSS growth method using MOCVD for $1{,}200\ s$. Fig. 3.1.1 provides a schematic illustrating InGaN NW growth. Trimethylgallium (TMGa), trimethylindium (TMIn), and ammonia (NH_3) were

employed as precursors for gallium (Ga), indium (In), and nitrogen (N), respectively; N_2 was used as a carrier gas.

The optimized InGaN NWs growth is procedure in the following growth parameters. The growth condition of V:III ratio is an important for development of axial InGaN NW growth; and the growth condition of temperature and pressure are adjusted to ensure optimum NWs growth. The dependence of InGaN NW growth on substrate temperature and growth pressure was studied to investigate the impact of growth conditions on vertically aligned and dense InGaN NWs. Furthermore, because of the catalysts might affect InGaN NW growth, we kept Ni thickness and annealing conditions as a constant in these studies. In order to analysis the effects of the growth parameters, the InGaN NWs of four different samples were grown in two series. The details will discuss in section 3.1. After growth optimization, during InGaN NW growth, the flow rates for TMGa, TMIn, and NH_3 were maintained at $f_{[TMGa]} = 18\,\mu mol/min\,f$, $f_{[TMIn]} = 1\,\mu mol/min$, and $f_{[NH_3]} = 424\,mmol/min$, respectively. Finally, In compositions in the InGaN NW samples were controlled by using a TMIn flow rate with growth temperature and pressure fixed at $715℃$ and $100\,tor$, respectively. The optical and material properties of InGaN NWs are provided in chapter 4.

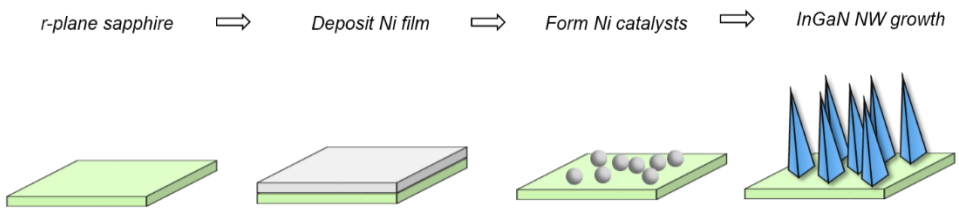

Figure 3.1: Schematic illustrating the VSS growth mechanism. Picture 1: single-side-polished *r*-plane sapphire, Picture 2: deposited 3 nm Ni film on top of sapphire, Picture 3: annealed Ni film to form Ni catalysts, Picture 4: vertical InGaN NW growth.

3.1.2 Impact of Growth Temperature

We first studied the substrate temperature dependence of InGaN NW growth at fixed growth pressure of 300 $torr$ and growth time of 1,200 s. Figs. 3.2(a)-(d) present the 45°-tilted scanning electron microscope (SEM) images of InGaN NWs grown at 660, 685, 715, and 735℃, respectively. The surface morphology of the InGaN NWs was found to be highly dependent on substrate temperature. A large number of small grain structures are observed on the surface when the growth temperature is as low as 660℃. At higher growth temperatures, the surface morphology changes from a film- to wire-like surface, as shown in Figs. 3.2(a)-(c). However, the NW density is again reduced significantly at growth temperatures above 735℃. The results demonstrate that the surface diffusion length and mobility of source species decreases with increasing growth temperature. The adatoms are more easily deposited on the side wall at higher temperatures; therefore, the wires can no longer exist at higher growth temperatures, and the samples exhibit thin film epitaxial growth. Vertically aligned InGaN NWs have also been observed only in the

sample grown at 715℃. The tendency of wire density and the fraction of vertical wires as a function of growth temperature will be discussed in the conclusion section.

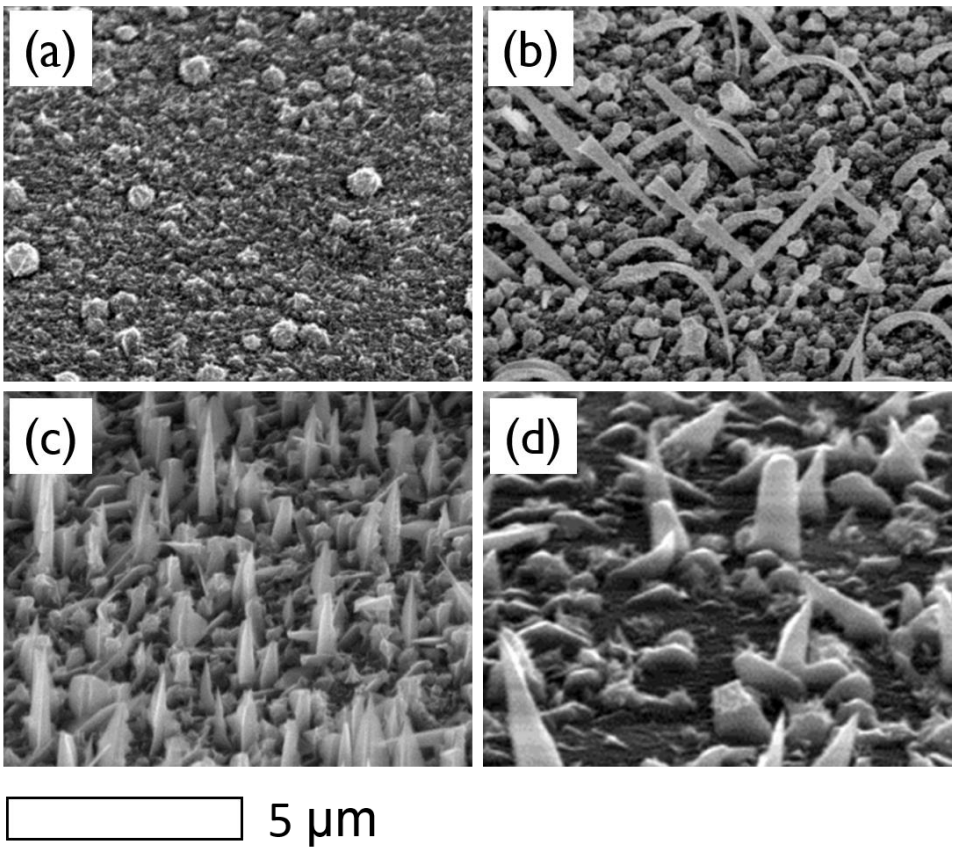

Figure 3.2: The 45°-tilted SEM images of InGaN NW grown at growth temperatures of (a) 600, (b) 685, (c) 715, and (d) 735℃. The growth pressure was fixed at 300 $torr$.

3.1.3 Impact of Growth Pressure

We also studied the impact of growth pressure on vertically aligned InGaN NWs. In this study, InGaN NWs were grown at various pressures between 50 and 400 $torr$ but a constant substrate temperature of 715℃. The SEM images of InGaN NWs samples grown at 50 , 100 , 200 , and 400 $torr$ are shown in Figs. 3.3(a)-(d), respectively. Good vertical alignment of the NWs is clearly observed in all samples. The base width of the InGaN NWs increased with growth pressure, perhaps because the adatom diffusion length of source species are easily changed by growth pressure. At high growth pressure, adatoms diffusion mainly originates from the surface and is caught by N at a NW side wall. Therefore, the NW length is short, and the base width is large. In contrast, the surface diffusion length can be relatively long at lower growth pressures. Low-pressure conditions can also lead to uniform growth of vertically aligned wires, however when the growth pressure at 50 torr, InGaN NWs sample shows taper again.

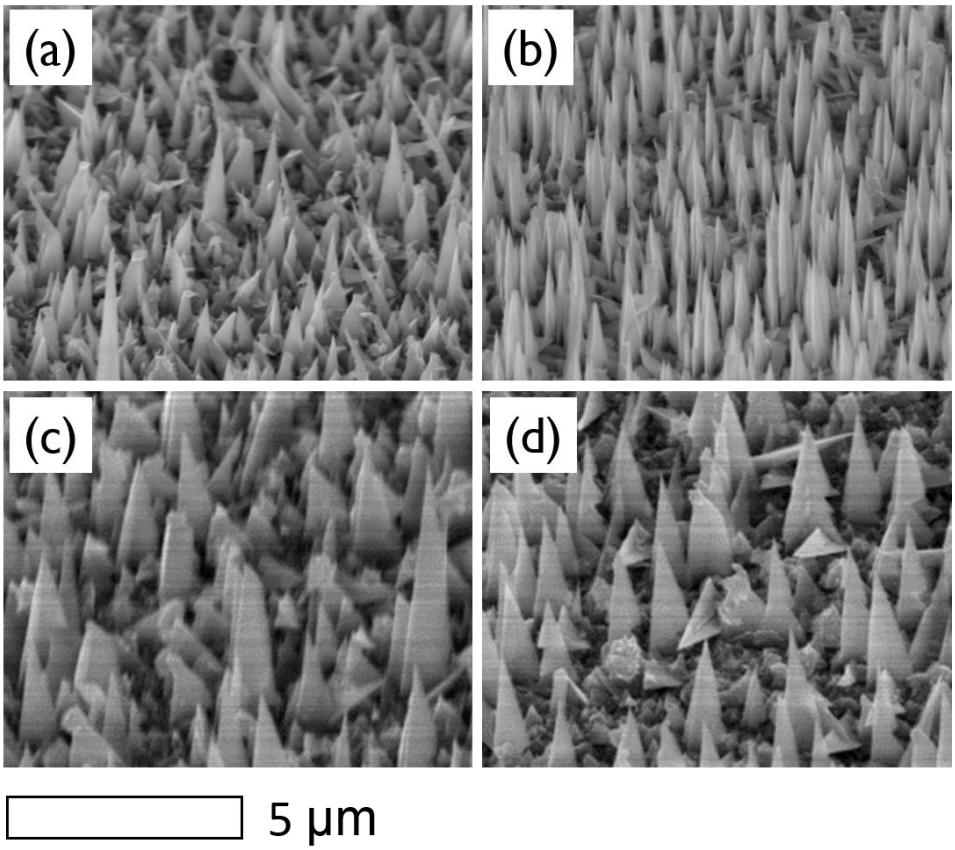

Figure 3.3: The 45°-tilted SEM views of InGaN NWs grown at pressures of (a) 50, (b) 100, (c) 200, and (d) 400 $torr$. The growth temperature was fixed at 715℃.

3.1.4 Summary

In summary, we demonstrated that InGaN NWs can be grown in a MOCVD chamber via the VSS growth mechanism. The results indicate the presence of InGaN NWs with a high degree of vertical alignment and high density on an *r*-plane sapphire substrate. This NW geometry is similar to that of GaN NWs grown by a Ni catalyst, as previously reported by Wang *et al* [78]. In two series of studies of growth

temperature and pressure, we discovered that InGaN NW growth is highly sensitive to both growth parameters via the Ni-catalyzed VSS mechanism. The reason of the growth window is very narrow, perhaps because two growth mechanisms, VSS and thin film epitaxial growth, are involved at similar growth conditions. Therefore, the thin film epitaxial growth cannot be ignored during NW VSS axial growth. The phenomena also can be found in Ni-induced GaN NW growth.

As temperature increases, the surface morphology changes from NW-like to thin film-like. This is likely because the carrier diffusion lengths change with substrate temperature. At lower temperatures, Ga adatoms incorporate with In and N at NWs sidewall, resulting in thin film growth. In contrary, axial NW growth occurs at higher temperatures, in the range of 705 to 725 ℃. However, atom energy also increases as temperature increases, resulting in a noticeable rise in incorporation rates at temperature > 715 ℃. Consequently, the diffusion length decreases slightly, and morphology changes back to film like surface when the temperature is higher than 725 ℃.

InGaN NW density is influenced by the catalyst density during NWs growth. In order to ignore the impacts from catalyst, the post-annealing process was performed at 780℃ in H_2 ambient for 900 s in pressure and temperature series. From the pressure series, it is observed that higher pressure during InGaN NW growth leads to less dense NWs with larger base width. This indicates that the Ga incorporation rate with catalyst is lower at higher growth pressure. Consequently, thin film growth dominates at high pressure.

A maximum NW density of $8.1 \times 10^8/cm^2$ was achieved through NW growth optimization, with nearly 90% vertical wires. Figs. 3.4(a) and (b) present the NW density and fraction of vertical wires as a function of growth temperature and pressure, respectively. Fig. 3.2.3(a) illustrates that the sample grown at 715℃ exhibits the highest NW density and most vertical wires across all samples. We estimate that the optimal temperature range for successful growth is approximately 20 to 30℃. Fig. 3.2.3(b) illustrates that growth pressure significantly impacts the NW density, and there is no clear difference in the percentage of InGaN NW vertical alignment for different growth pressures. These results confirm that the diffusion length of species is longer at low pressures than at higher pressures. In summary, we observed that the vertical alignment and density of NWs are correlated with both growth temperature and pressure.

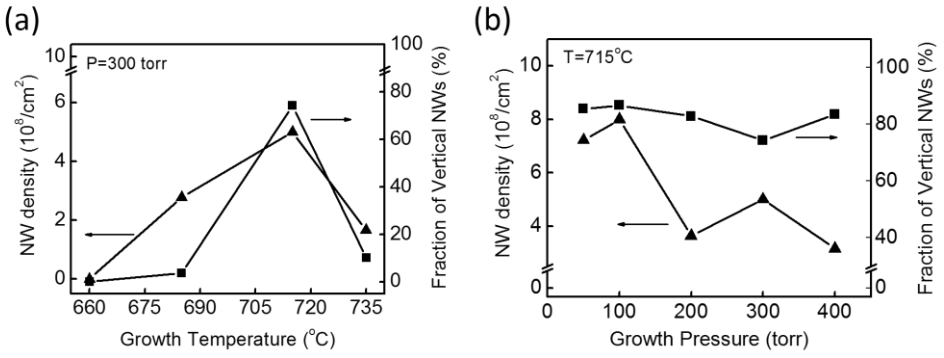

Figure 3.4: InGaN NW density and fraction of vertical aligned NWs as a function of (a) growth temperature and (b) growth pressure.

Although InGaN NWs have been grown, further understanding and control of morphology are required. Details of NW morphology will be provided in the following section. Because the size of a catalyst impacts its melting point, non-uniform InGaN NW growth occurs in this study; thus, we aimed to maintain a constant Ni film thickness and annealing process for all samples. Further control of the uniformity of catalyst size may be required.

3.2 Analysis of NW structure

Both 45°-tilted and cross-sectional SEM images reveal the orientation of NWs, as shown in Figs. 3.5(a) and (b), respectively. As shown in the cross-sectional SEM image, a $350\ nm$ film of InGaN was grown concurrently on the substrate. The lengths of the NWs range from 1.5 to 3.5 μm, with an average length of 2.2 μm. The diameters range from 250 to $450\ nm$ at the base and 20 to $40\ nm$ at the tip. The highest NW density achieved is $8.1 \times 10^8\ /cm^2$, with 63% surface coverage. The three NW side wall facets consisted of a {0001} plane and two equivalent {$\underline{1}$101} semi-polar planes, as shown in the top-view SEM image in Fig. 3.5(c) [79, 80, 81, 82]. Fig. 3.5(d) presents a schematic of InGaN NWs consisting of a triangular base and sharp tip. The figure also illustrates the shape of an InGaN NW, a tetrahedron with four triangular faces. The growth direction is along the [11$\underline{2}$0] direction, or the *a*-plane, which is perpendicular to the substrate. The NW growth direction was confirmed by selected area diffraction (SAED) patterns collected during TEM

measurements. Based on SEM images, we observe anisotropic NW growth on the side walls caused by different surface energies at the three facets. Hence, thin-film epitaxial growth on InGaN side walls is highly selective in favor of higher surface energy. In the following chapter, we further investigate the details of scaling in NW development with time-dependent studies.

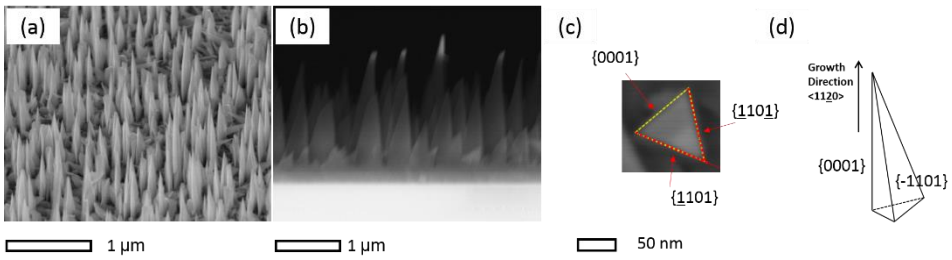

Figure 3.5: SEM images: (a) 45° tilted, (b) cross sectional, and (c) top view. (d) Schematic diagram of an InGaN NW. The NW growth direction is along [11$\underline{2}$0] and consists of three facets.

3.3 Time dependent InGaN NW Growth

After deposition of a 0.3 nm Ni thin film, the sample was annealed at 780℃ for 900 s. An atomic force microscopy (AFM) image of Ni catalysts was taken after the annealing process, as shown in Fig. 3.6(a). From the image, slight variations in the size and height of Ni catalysts were observed. Based on the AFM images, we can estimate the distribution of the Ni catalyst after annealing. As shown in Fig. 3.6(b), the size of Ni catalysts is between 10 and 20 nm. The experimental results indicated that Ni catalysts have an average diameter of 14.6 nm , height of $1 \pm 0.3\ nm$, and density of $3.8 \times 10^{12}\ /cm^2$. Based on experience, the catalyst size decreased with

increased annealing time and temperature. Thus, we are convinced that NW density can also be controlled by annealing conditions as a result of changes in catalyst density. In this study, we maintained constant Ni thickness and annealing conditions for all InGaN NW growth.

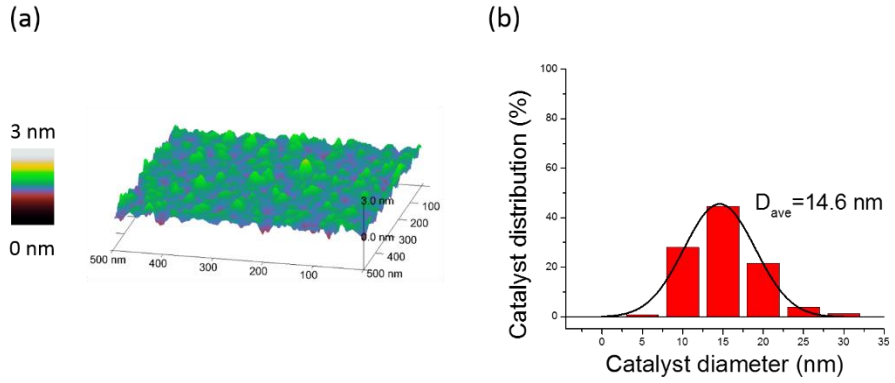

Figure 3.6: (a) Three-dimensional AFM image of the substrate after annealing for 900 s; (b) histogram of Ni catalyst distribution based on AFM images. The average diameter is 14.6 nm.

After the annealing process, the metal organic (MO) source begins to flow into the MOCVD chamber. The catalysts then react with MO species to form a new compound (Ni_2Ga_3). We consider this short period of catalyst reaction time as the first stage of NW growth (the "initial growth stage"), as NW growth can only occur after Ni_3Ga is formed. Following the initial growth stage, InGaN NW growth is then facilitated by the catalysts until the catalysts disappear. During NW growth, Ni catalysts may be incorporated into the InGaN NW, evaporate under the high

temperature, or undergo a combination of both. As long as the catalysts still exist on the top of NWs, VSS mechanism will dominate the growth process. We named this period of the growth process as the "NW growth stage". As soon as the Ni catalysts disappear, NW growth reaches its final phase, in which thin film deposition occurs everywhere on the sample. The actual growth rate of the NWs depends on the surface potential on each facet of the NW. Therefore, we can expect the thin film epitaxial growth to dominate the NW growth. This stage is the final stage of InGaN NW growth, and we named it the "thin film growth stage".

In summary, we propose an InGaN NW growth model to represent the process of NW growth as synthesized by the VSS mechanism. Because the catalysts play an important role in this process, the growth model can be divided into three major stages based on catalyst status. The initial stage features Ni catalyst (Ni_2Ga_3) formation. The second stage is the NW growth stage, in which the Ni catalyst still exists on the NW tip. In the final stage of InGaN NW growth, only thin film epitaxial growth occurs because the catalyst no longer exists. Fig. 3.7 provides a schematic of each stage.

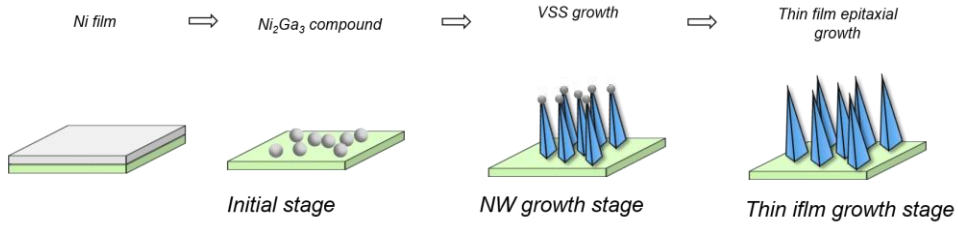

Figure 3.7: Schematic illustrating the growth of InGaN NWs by the VSS mechanism on an *r*-plane sapphire substrate. Picture 1:0.3 nm Ni on an r-plane sapphire substrate; Picture 2: Ni_2Ga_3 compound formation; Picture 3: NW growth by the VSS mechanism; Picture 4: NW growth by both VSS and epitaxial thin growth.

3.3.1 Time-dependent Evolution of NW Growth

Studying the time dependence of NW growth behavior experimentally enables us to estimate the NW shape during its formation. In addition, the results can further confirm the hypothesized growth model. For the following studies, InGaN NW samples were grown at the same growth conditions but various growth times. Two series of sample sets were prepared at various growth times from 300 to 1,500 s. Each series consists of four samples with 300 s of spacing. To eliminate measurement error, we measured hundreds of InGaN NWs from random SEM images. We can estimate the vertical length and base width of InGaN NWs based on the NW distribution. The average and range of measured NWs is presented in each figure as a symbol and error bar, respectively. In the sample with the shortest growth times ($300\ s$), the surface exhibits both a very short NW length and thin film nucleation layer. Therefore, we may expect some measurement errors. We believe that the other measurement errors are consistent and insignificant in this study.

3.3.2 Ni Catalysts with Growth Time

Figs. 3.8(a) and (b) present TEM images of InGaN NW tips taken after 600 and 1,200 s, respectively. The images reveal that the Ni-based catalyst is only present at the end of the NW in the 600 s growth sample. The TEM image also indicates that the catalyst no longer existed but left layered structures at the tip after

1,200 *s* of growth. Considering catalysts size before growth and after 600, and 1,200 s of growth, the catalyst size reduces with increased growth time. That implies the catalyst plays the essential role in the vertical formation of NWs. Thus, there is sufficient evidence of non-linear scaling growth behavior due to the catalyst involved during the growth period.

As mentioned, during NW growth, Ni catalyst may be incorporated into the InGaN NW, evaporate at high temperature, or undergo a combination of both. Assuming that the evaporation and incorporation rates are constant during NW growth, we propose that the catalyst volume and growth time are linearly related. Further studies are needed to correlate the catalyst size as a function of growth time.

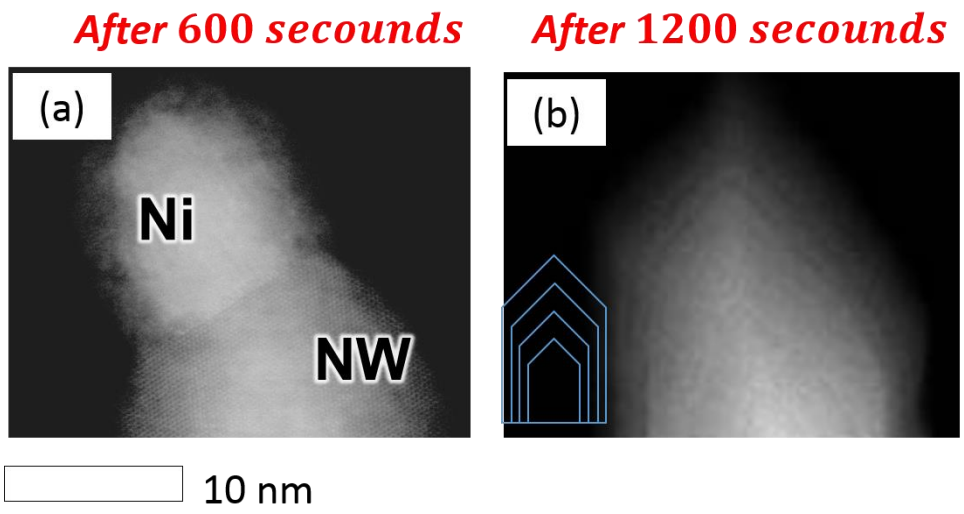

Figure 3.8: TEM images of InGaN NW tips after (a) 600 and (b) 1,200 *s* of growth.

3.3.3 Vertical Length and Base Diameter with Growth Time

For InGaN NW growth, we first study the vertical length and base diameter as a function of growth time. Two series of sample sets were prepared as mentioned above. We averaged over 100 NWs from each sample with various growth times. Based on SEM images, we determined the vertical length (H), semipolar width (W_1), and *c*-plane width (W_2), as shown in Fig. 3.9. The figure illustrates that the NW vertical length and semipolar width are linearly related. However, the NW vertical length and *c*-plane width correspond to the power law $H = AW_1^{\alpha}$, in which power index α equals 0.8 in our experimental results. Furthermore, the triangular shape of the *c*-facet does not change with time, meaning most deposition occurs at the semipolar facet during thin film epitaxial growth. We have experimentally observed that the aspect ratios of H/W_1 changed with increasing growth time. The time dependence of the NW vertical length and base will be discussed in detail below.

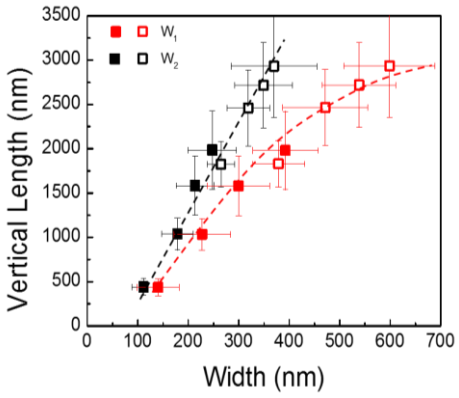

Figure 3.9: Two series of scaling NW length-width dependences of Ni-catalyzed InGaN NW growth. The fitting curve is shown as a dashed line, and experimental data are shown as symbols. W_1 and W_2 represent the semipolar and *c*-plane width, respectively. The vertical length is measured from an InGaN thin film.

3.3.4 Base Diameter with Growth Time

Fig. 3.10(a) presents SEM images of two NWs that have intersected each other during the growth, and the inset is a top-view SEM image. We believe that the VSS growth mechanism does not contribute to side wall deposition, leading only to NW growth along the vertical direction. In the experiment, we discovered that NW side walls scale up simultaneously with VSS growth. Participation from thin-film epitaxial growth is expected. Based on the SEM images, each NW has three side wall facets, the {0001} polar plane and two equivalent {$\underline{1}$101} semipolar planes. We estimated the surface of each facet using broken bond models. The two equivalent {$\underline{1}$101} planes have identical surface energies of $181\ meV/\text{Å}^2$, higher than the energy of the {000$\underline{1}$} plane, $128.9\ meV/\text{Å}^2$ [83]. Furthermore, the thin-film deposition rate depends on the thin films' surface potential energy, leading to anisotropic growth on each facet. Fig. 3.10(b) illustrates that the growth rate is side wall dependent. The results confirmed that the width of the *c*-plane saturates over time, whereas the widths of the semipolar sides do not. A similar scaling thermodynamic model for GaN NWs was reported [84].

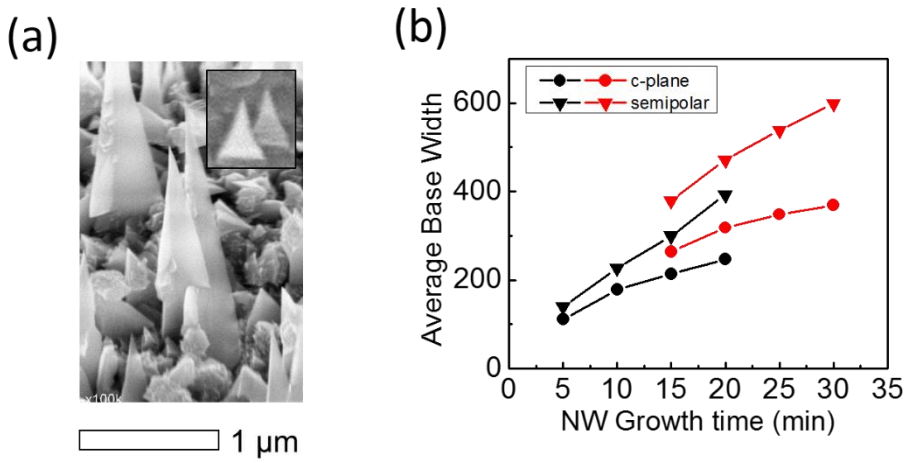

Figure 3.10: (a) 45°-tilted and top-view (inset) SEM images indicate that two NWs have enveloped each other during growth. The contribution on the side wall proceeds simultaneously with axial growth; (b) average base width of InGaN NWs as a function of growth time.

Based on TEM images, we discovered that NW diameter is significantly different after 600 and 1,200 *s* of NW growth as shown in Fig. 3.11(a) and (b), respectively. The result is an evidence of thin film epitaxial growth was dominated in the end of growth. In addition, it confirms that the expected anisotropic growth rate at the two equivalent semipolar {$\underline{1}$101} planes and the polar {0001} plane. The growth of InGaN NWs is largely lateral and likely to be one sided on the more energetically favorable facet.

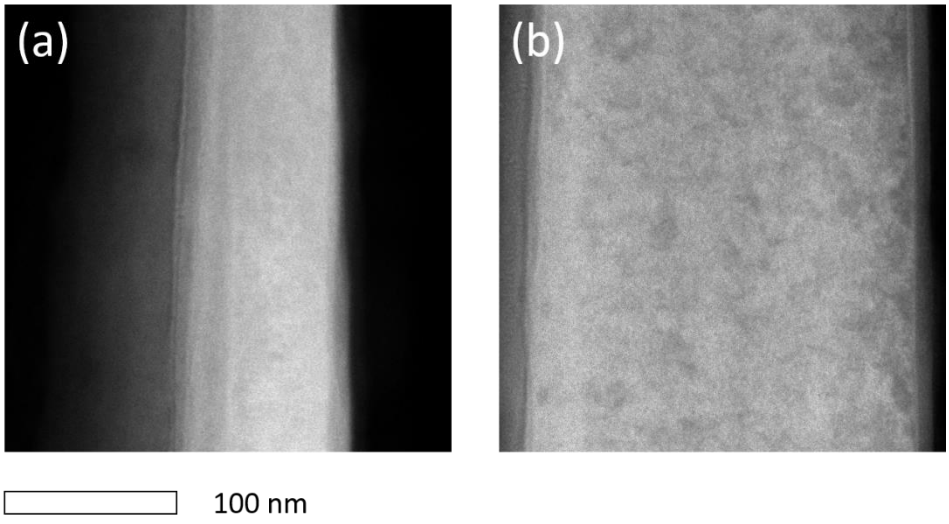

Figure 3.11: TEM images of an InGaN NW side wall after (a) 600 and (b) 1,200 s of growth. There is a significant contribution in the lateral direction between 600 and 1,200 s.

3.3.5 Vertical Length with Growth Time

Our experimental results indicated that the measured NW length $L(H)$ increased with increasing growth time and saturated over time. In contrast, the thin-film thickness continued to increase with increasing growth time, as shown in Fig. 3.12. We expected that thin-film thickness and growth time would have a linear relationship. The results match the common behavior of thin epitaxial growth. In NW axial growth, the Ga atom diffusion length, λ, is approximately 140 nm, which is relatively short compared to the vertical length of NWs after 300 s of growth. Therefore, the diffuse contribution from the bottom thin film exists for only a short period, and we could neglect the influence from the thin film overall. The NW

vertical growth rate decreased with increasing growth time, revealing that vertical length is limited by the existence of the catalyst; however, thin-film epitaxial growth remained constant over time, independent of the existing of a catalyst. This phenomenon is similar to bottom thin-film growth, which agrees with our model prediction as well.

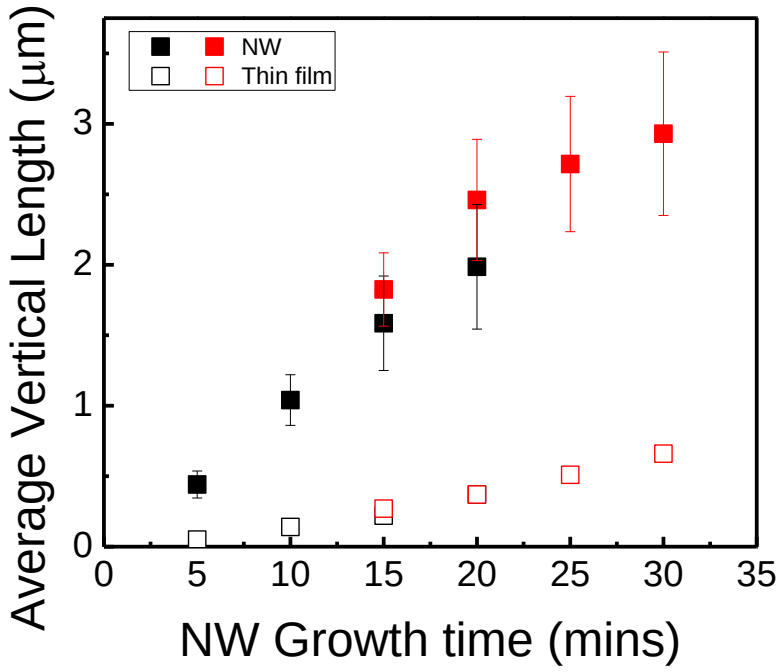

Figure 3.12: Experimental results of NW vertical length and thin film thickness as a function of growth time. The experimental data are shown as symbols. The error bars represent the range in which all samples were measured.

3.3.6 Three Facets with Growth Time

The epitaxial growth rate in semipolar planes is higher than that in the *c*-plane because epitaxial growth is surface-energetically selective. This anisotropic epitaxial lateral growth is due to the orientation-dependent, selective epitaxy of InGaN. Therefore, the triangular base could change its shape over time. Based on top-view SEM images, the angle between two semipolar planes reduces to 36° after 1,800 *s*. As shown in Fig. 3.13(a), the growth rate is very different on each plane. From the figure, the growth rate of the {0001} plane is considerably faster than those of the two {1̲101} semipolar planes. The angle between two semipolar planes reduced with increasing growth time. Furthermore, under our growth conditions, the angle between {0001} and {1̲101} increased over time, as shown in Fig. 3.13(b), meaning that NW growth evolves into thin-film growth over time.

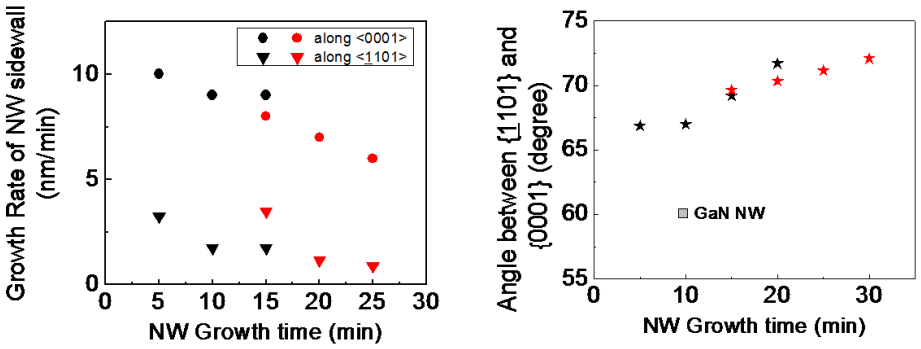

Figure 3.13: (a) Growth rate along the <0001> and <1̲101> directions as a function of growth time; (b) angle between two side wall facets {0001} and {1̲101} as a function of growth time. Values were measured based on SEM images.

3.3.7 Overview of InGaN NW growth model

In summary, we have demonstrated the scaling of vertical length and base width of MOCVD-grown InGaN NWs with time. We suggest a growth model of Ni-catalyzed NW growth whose behaviors are governed by catalyst size and atom surface diffusion length. InGaN NW growth combines both VSS and thin epitaxial growth mechanisms. These two growth mechanisms affect NW morphology at different growth stages. With increasing catalyst size, more time is required to reach super-saturated status for NW growth to proceed. Additionally, the amount of Ni catalyst decreased over time, and the NW has a tapered shape at the end of the growth process.

If change in catalyst size can be prevented over growth time, InGaN NWs could have constant radii during axial growth. However, in our experiment, we discovered that NWs have a layered structure, which causes thin-film epitaxial growth after the catalyst disappears. This understanding provides a direction to control NW morphology during growth.

3.4 Summary

In this chapter, we have demonstrated the highly dense and vertically aligned InGaN NWs grown on *r*-plane sapphire substrates via VSS growth using MOCVD. We found that the vertical alignment and NW density highly depend on the growth temperature and pressure, respectively. We have characterized InGaN NWs based on

TEM and SEM images and discovered that NWs consist of two equivalent semipolar planes {$\bar{1}$101} and a polar plane {0001} on the side walls. As the surface energy is different on each facet, epitaxial growth in the lateral direction causes anisotropic growth.

Our hypothesized growth model and experimental results suggested that two growth mechanisms, vapor epitaxial and VSS, occurred simultaneously and competed against each other. The VSS growth mechanism dominates when the catalyst still exists, and the thin-film epitaxial growth mechanism dominates at the end. The most critical part of the interface between the two growth mechanisms is the absence of the Ni catalyst due to incorporation into material and dissolution at high temperatures during NW growth. Therefore, the catalysts are important in the formation of InGaN NWs via the VSS mechanism. The ability to control the initial step is important to predict the geometry of NWs at any given time.

CHAPTER 4

Properties of InGaN NWs

4.1 Optical Properties

4.1.1 Photoluminescence and Cathodoluminescence

To investigate the optical properties of InGaN NWs, photoluminescence (PL), and cathodoluminescence (CL) measurements were conducted with a continuous wave (CW) He-Cd laser ($40\ W/cm^2$) as an excitation source. The PL result indicates an intense emission at $600\ nm$ and two weak emissions at 375 and $458\ nm$ at both room temperature (300 K) and low temperatures (30 K), as shown in Fig. 4.1(a). In particular, the commonly observed PL peaks of GaN involve the yellow ($2.2\ eV$) spectral range at room temperature and the band toward the red range with increasing In content in undoped $In_xGa_{1-x}N$. Therefore, the peak at 600 nm ($2.06\ eV$) is likely the common defect-related yellow band emission in nitride material based on an In composition of 18.9% from the InGaN NW sample. However, based on TEM results, the NWs have relatively few defects and dislocations, and the emission

intensity is enhanced in low-temperature (30 K) PL measurements. This emission may be due to either a localized state or dislocation defects from NWs and/or bottom InGaN films. This unknown emission remains under investigation.

According to the CL distribution image taken from all wavelength emissions shown in Fig. 4.1(b), the two emissions most likely originated from InGaN NW structures instead of from the bottom InGaN thin film or sapphire substrate. Based on low-temperature PL, employing a bowing coefficient of 2.95 [85], the In compositions corresponding to the emission peaks at 2.67 ($\lambda = 460\,nm$) and 2.06 eV ($\lambda = 600\,nm$) were calculated as 18.9 and 37.9%, respectively. The reasons for different In compositions in bulk InGaN NW will be discussed in the following chapter.

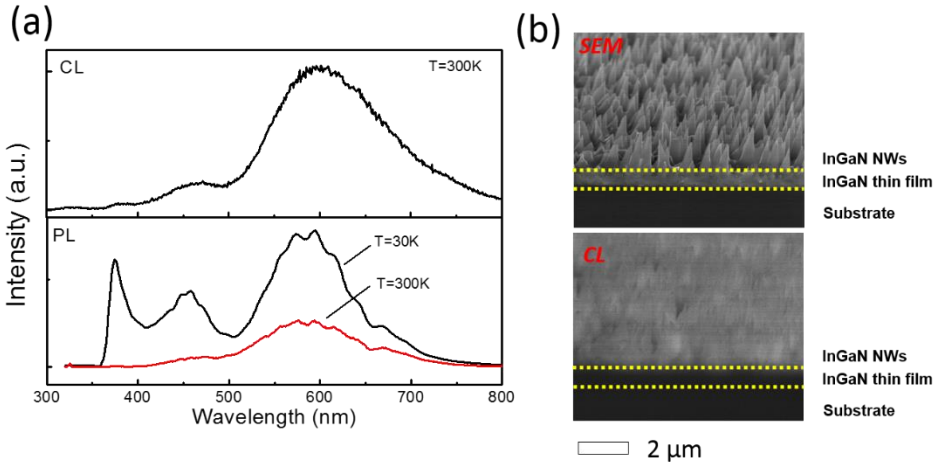

Figure 4.1: (a) CL spectra at 300 K (top) and PL spectra at 30 and 300 K (bottom) of InGaN NWs grown at 715℃ with fixed 200 torr at 300 and 30 K. (b) SEM image (top) and CL spectra (bottom) at all wavelength emissions at 300 K.

Fig. 4.2 presents NW-level CL images, with an emphasis on two major emissions at 460 and 600 nm, corresponding to the SEM image. The InGaN NW, InGaN thin film, and sapphire substrate are clearly distinguishable. We discovered both emissions from the InGaN NW region. According to XRD results and the bulk InGaN band gap [86], we estimate that the PL energy emission of InGaN NWs is approximately 2.7 eV, which is close to the higher energy emission. In TEM images *(data shown below)*, some of the threading dislocations might prompt high In clusters or high In content valleys across NWs. Therefore, it is reasonable to assign the low- and high-energy emissions to localized-state and bulk InGaN NW-related emissions. A deeper localized state can accumulate the carriers more easily than at a high-energy state, which could explain the enhanced emission of the localized state over that of the bulk InGaN NW from room-temperature PL. For that reason, the ratio of bulk to localized peak emissions could express the uniformity of InGaN NW growth. Furthermore, InGaN NW growth conditions must be optimized to reduce the dislocation density and remove the uniform In phenomenon.

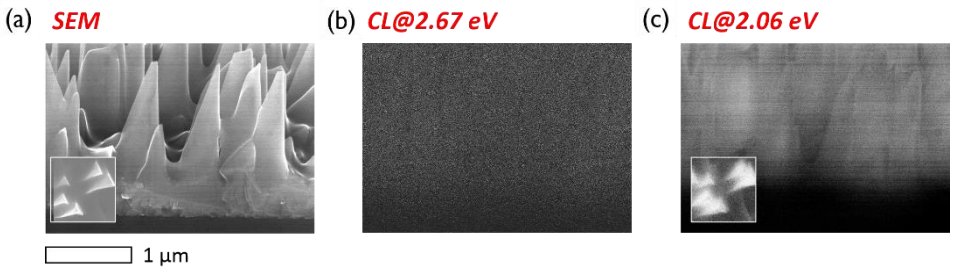

Figure 4.2: (a) Cross-sectional SEM image, with the top view as an inset. (b) NW-scale CL spectra at 2.67 eV. (c) CL spectra at 2.06 eV. CL measured at 300 K.

4.1.2 Energy-Dispersive Spectroscopy

TEM with energy-dispersive spectroscopy (TEM-EDX) investigations were performed using a JEOL 2010F electron microscope with an acceleration voltage of $200\ kV$. EDX was carried out during TEM measurements at the NW level, as shown in Figs. 4.3(a) and (b). We discovered some threading dislocations across the NWs in both horizontal and vertical line scans. These dislocation densities not only influenced the non-uniform In composition but also act as either radiative or non-radiative recombination centers in the NW sample. These densities may significantly impact the optical properties of the InGaN NWs. Additionally, these threading dislocation leads to non-uniform In incorporation during growth that could explains the wide full width at half maximum (FWHM) observed in the XRD measurements, as shown in Fig. 4.3(c). Based on InGaN peak shifting in two-theta rocking curve scans along the *a*-plane GaN [11$\underline{2}$0] direction, we can calculate an average In composition in InGaN NW samples of 15.4%. The result matches the average In contents of horizontal and vertical TEM-EDX scans (15.9 and 16.2%, respectively). TEM-EDX analysis was performed to investigate the electron-beam irradiation on the relative indium and gallium distribution within the NWs. The In composition was obtained by spectrum intensity of In to (In+Ga) ratio from TEM-EDX scanning across the each scanning point. The small difference between these two values might be because the XRD result is taken from hundreds of NWs, whereas the TEM-EDX result is taken from a portion of a single NW. Notably, an In cluster was found with high In composition (up to 30%). Thus, the carriers might easily migrate to the

localized state at higher In composition, possibly explaining the lower energy emission with high luminescence efficiency [87]. More details on this topic are provided below.

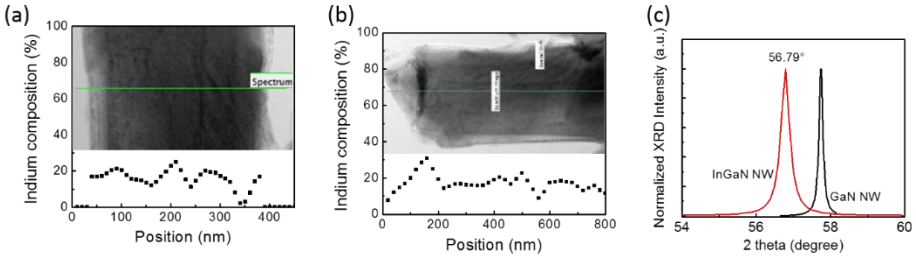

Figure 4.3: TEM-EDX scan of InGaN NWs with (a) horizontal and (b) vertical scans. In composition from each scan point is shown at the bottom of (a) and (b). The scan spacing is 10 *nm*. (c) X-ray diffraction (XRD) of InGaN and GaN NWs.

4.1.3 Temperature-dependent Photoluminescence

As shown in Figs. 4.4(a) and (b), we discovered that most dislocation densities close to NW side walls resulted from lateral growth. Those dislocation densities affect the In composition fluctuations during NW growth. The high-In-content valleys correlate with strong carrier localized states, which impact in either non-radiative or radiative recombination. To decrease dislocation density, we must suppress lateral growth and perform axis growth only.

The V:III ratio affects nitride-based epitaxial growth. Therefore, a series of InGaN NW samples was grown at V:III gas flow ratios of 1,300, 1,680, and 2,140 for 1,200 s, and the other growth conditions were fixed. We investigated the ratio of

high to low-energy emissions from all samples. From the results, at 300 K, the samples grown with V:III ratios of 1,300, 1,680, and 2,140 yielded PL ratios of high to low energy of 0.35, 1.2, and 5.4, respectively, as shown in Fig. 4.4(a). This result suggests that samples with high V:III ratios decrease the density of the high-In valley.

Deeper localization centers strongly confine carriers. As sample temperature increases during PL measurement, we can calculate the carrier activation energy, which represents carriers from localized to delocalized states by thermalization [88]. Therefore, temperature-dependent PL has been executed from 20 to 300 K. The integrated PL intensity of the low energy peak as a function of 1,000/T is shown in Fig. 4.4(b). The experimental data are fitted by Eq. 4.1, representing PL thermal quenching.

$$I(T) = \frac{I(0)}{1 + A_1\left(e^{-\frac{E_{a1}}{kT}}\right) + A_2\left(e^{-\frac{E_{a2}}{kT}}\right)} \tag{4.1}$$

The left side of Eq. 4.1 describes the integrated PL intensity as a function of temperature, and E_{a1} and E_{a2} on the right side are two thermal activation energies at temperatures above and below 40 K, respectively. Here, we denote the integrated PL intensity at 10 K as $I(0)$. We fitted two non-radiative channels from each sample based on the best fitting, as shown by a solid line in Fig. 4.4(b). Samples with V:III ratios of 1,300, 1,680, and 2,140 had activation energies of 179, 52, and $37\ meV$ at $T \geq 40\ K$ and 23, 18, and $10\ meV$ at $T < 40\ K$, respectively. We discovered that

both activation energies reduced with an increasing V:III ratio. The phenomenon indicates that In composition fluctuations in InGaN NWs were decreased considerably when NWs were grown in high-V:III environments. A high-V:III environment helps to suppress the lateral growth mode during NW growth, which provides in uniform bulk InGaN NW growth (*refer to section GaN NW*).

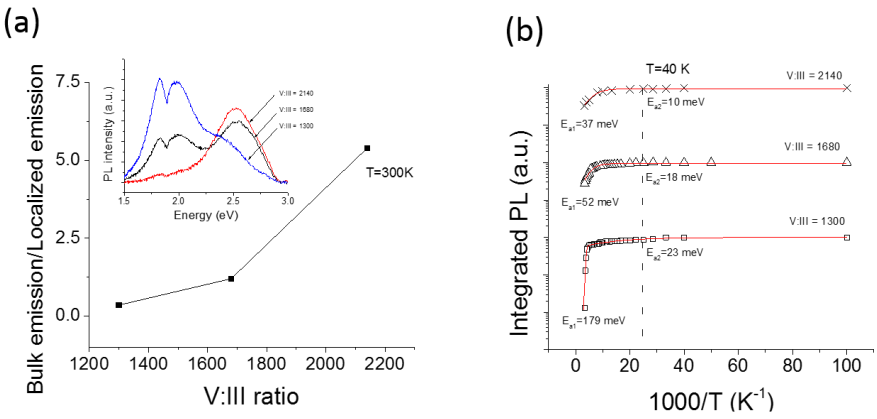

Figure 4.4: (a) Ratio of bulk to localized-state emission for various V:III ratios. The inset shows PL spectra of three samples at 300 K. (b) integrated PL spectra as a function of 1,000/T. The red lines represents fitting curves, and experimental results are shown as symbols.

4.1.4 Temperature-dependent and Time-resolved Photoluminescence

Photo-generated carriers may be trapped by non-radiative centers as well. This phenomenon results in low internal quantum efficiency, affecting device performance. In addition, we performed time-resolved PL (TRPL) measurements of

an InGaN NW sample with a V:III ratio of 2,140. The excitation condition used a $325\,nm$ He-Cd laser with power density of $150\,W/cm^2$. According to the FWHM of the laser spot, the resolution is $3\,ps$ for all measurements. The carrier lifetime results are fitted by the exponential decay function in Eq. 4.2.

$$I(T) = I(0)e^{-\frac{t}{\tau}} \tag{4.2}$$

Based on the TRPL measurement at 10 K, we have found a carrier lifetime of $30.6\,ps$ in bulk InGaN NWs. Figure 4.5(a) presents the color mapping of emission energy. Additionally, temperature-dependent TRPL results in a distinguishable transition at 40 K, as shown in Fig. 4.5(b). Carrier lifetime generally decreases with increasing temperature because of the gradual activation of non-radiative recombination centers by thermal energy with increased temperature; non-radiative recombination will dominate at room temperature. We found that the carrier life time remains rather constant ($30\,ps$) when the temperature is below 40 K but drops to $17\,ps$ at room temperature (300 K), suggesting that there are no non-radiative channels involved below 40 K. We calculated a non-radiative carrier lifetime of $38\,ps$ at 300 K, and nearly 45% internal quantum efficiency (IQE) was found by assuming a fixed radiative carrier lifetime at any given temperature. Those results match with simply integrated PL ratios of high to low temperatures, suggesting that InGaN NWs are a good candidate for optoelectronic applications.

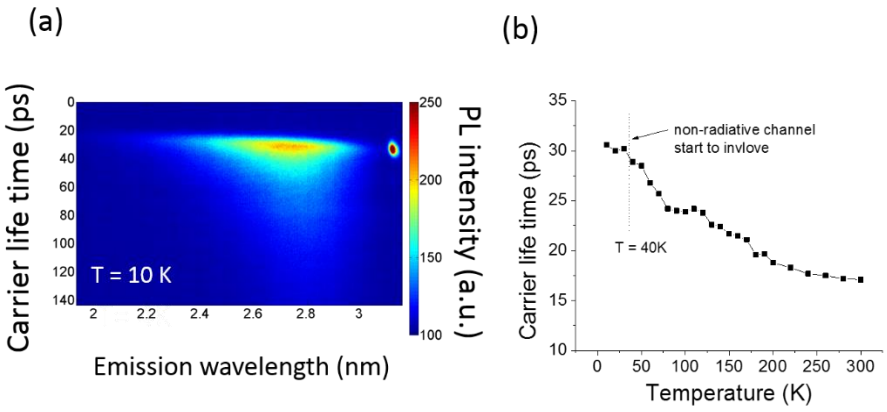

Figure 4.5: (a) TRPL result at 10 K; (b) carrier lifetime, fit by Eq. 4.2, as a function of temperature between 10 and 300 K.

4.1.5 Overview of optical properties

In summary, we have confirmed both high- and low-energy emissions from InGaN NWs, associated with bulk InGaN NW emissions and localized-state emissions, respectively. Due to non-uniform growth, In composition fluctuates across each NW, and a high-In-content valley may be present at each dislocation valley. The high-In-content valley can be eliminated by increasing the V:III ratio during growth. Based on thermal activation energy, InGaN NW samples with low V:III ratios display an accumulation of carriers at localization valleys. Under optimized growth conditions, we are able to obtain InGaN NWs with high crystal quality. Furthermore, the local auger recombination phenomenon is greatly reduced, which might have a positive impact on device performance. Additionally, we

observed nearly 45% internal quantum efficiency and a radiative carrier lifetime of 30 ps from PL and TRPL measurements, respectively.

4.2 Emission Energy of Bulk InGaN NWs

4.2.1 Surface Morphology

Fig. 4.6 presents SEM images of InGaN NW surface morphology with different growth conditions for tuning In composition. The first series of InGaN NWs was grown at fixed temperature of 715℃ and a growth pressure of 250 $torr$, with various TMIn flow rates of 5, 20, 40, and 100 $sccm$, as shown in Figs. 4.6(a) to (d), respectively. Another series of InGaN NWs was grown at fixed temperature of 715℃ and a growth pressure of 100 $torr$, with various TMIn flow rates of 50, 100, 200, and 300 $sccm$, as shown in Figs. 4.6(e) to (h), respectively. Fig. 4.6(i) presents a GaN NW sample as a control sample, which was grown at the same conditions, except that TMIn flow was maintained at 0 $sccm$. In this study, we maintained a constant V:III ratio for all samples. The results illustrate that NW alignment and density are not affected by TMIn flow.

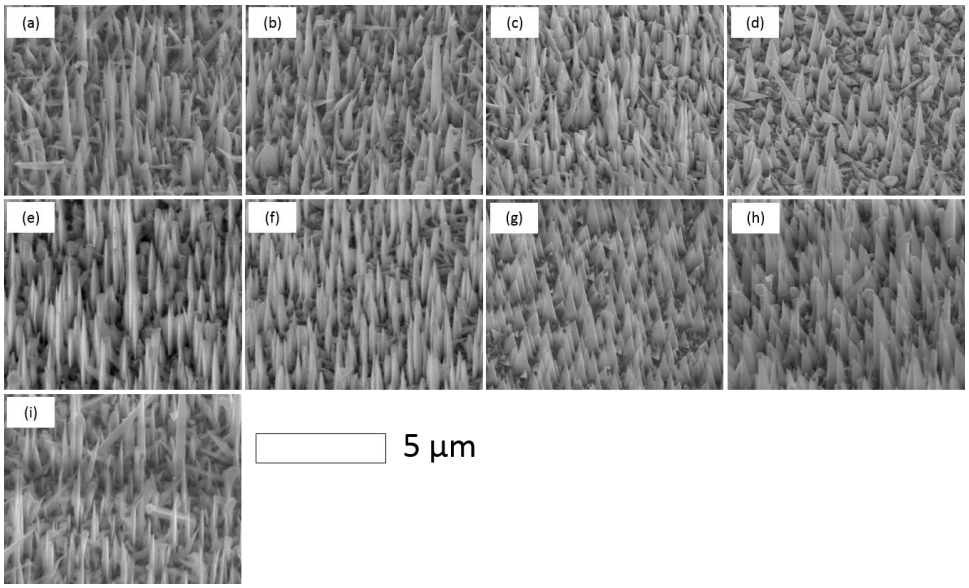

Figure 4.6: SEM images of InGaN NWs with growth temperature fixed at 715℃, pressure fixed at 250 $torr$, and TMIn flow of (a) 5, (b) 20, (c) 40, and (d) 100 sccm, and another set with the same growth temperature, pressure fixed at 100 $torr$, and TMIn flow of (e) 50, (f) 100, (g) 200, and (h) 300 sccm. A control GaN NW sample (i) was grown at the same conditions (V/III ratio, temperature, carrier gas, N_2, and pressure at 250 $torr$).

4.2.2 Fabrication Development for Optical Measurement

To prevent the excited emission from reaching the bottom InGaN thin film, we covered the film with metal and left the NWs exposed. Fig. 4.7(a) presents the fabrication flow. Vertically aligned InGaN NWs were first grown in MOCVD. After growth, a 200 nm conformal thin layer of chromium (Cr) was deposited on the sample by a sputter tool at a pressure of 10^{-6} $torr$. A photoresistor layer was spin-coated to 3 μm thickness and hard baked at 115℃ for 1 h. Coordinated-control plasma etching was performed until the tops of NWs were exposed. The photoresistor

layer remained approximately 400 nm thick, which only covered the bottom InGaN NW and InGaN thin film. In the following, we used a chemical etchant to etch away the Cr layer without protection by a photoresistor. At the end of experiment, we removed the photoresistor for PL measurement. Under this fabrication sequence, the Cr layer only covers the thin film and bottom NWs and remain atop the NW surface as before. Both 45°-tilted and cross-sectional SEM images indicate that the InGaN thin film was fully covered by the Cr layer, as shown in Fig. 4.7(b) and its inset, respectively.

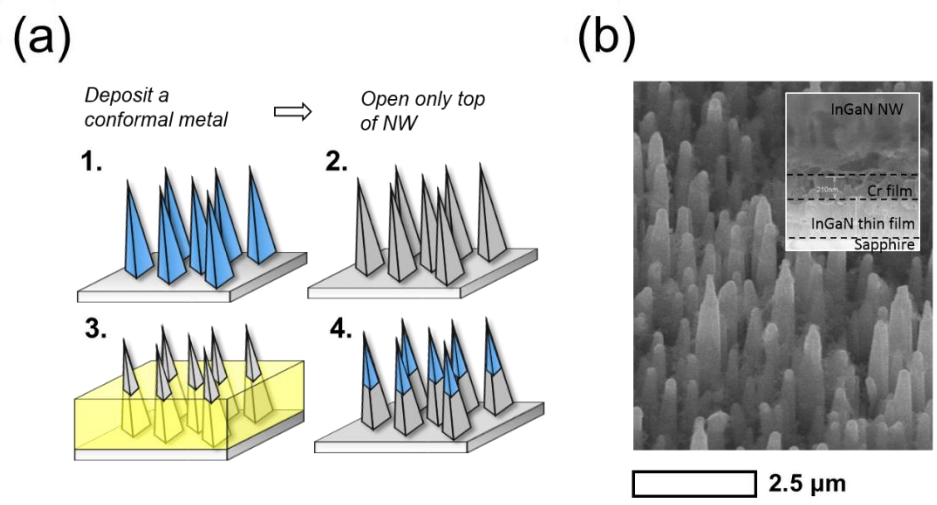

Figure 4.7: (a) Schematic illustrating process flow. Picture 1: InGaN NW growth; Picture 2: conformal 200 nm Cr deposited on NWs; Picture 3: spinning and coating of SPR 220 with 3 μm thickness and etching by plasma until the tops of NWs are exposed; Picture 4: Cr etching by chemical solution and removal of SPR 220. (b) SEM image of stage 4, with a cross-sectional SEM image as the inset.

Room-temperature (300 K) PL measurements were performed at the first and fourth fabrication stages in the same sample, as shown in Fig. 4.8(a). The sample was excited by a $260\,nm$ laser with an excitation power of $40\,mW$, and the emitted luminescence light was collected through a spectrometer. The focused spot size of the laser was estimated to be $100\,\mu m$ in diameter. As illustrated in Fig. 4.8(a), the room-temperature PL peak emission energy from Cr-covered InGaN NWs is approximately $2.81\,eV$ ($\lambda = 440\,nm$), determined by fitting a Gaussian curve. The Cr-covered sample exhibits extremely small YB-related emissions, which is strong evidence of low defect density in the InGaN NW region compared to that of the bottom thin film. However, the FWHM of the InGaN NW emission is $0.37\,eV$. This broadening phenomenon of the InGaN NW peak indicates that In composition fluctuates during growth. The average In composition in InGaN NW samples was measured from XRD along the [1$\underline{1}$02] a-plane. The In composition was estimated as 10.8% by Vegard's law for bulk relaxed lattice parameters. This value matches the bulk InGaN band gap, as shown in the inset of Fig. 4.8(b) [89].

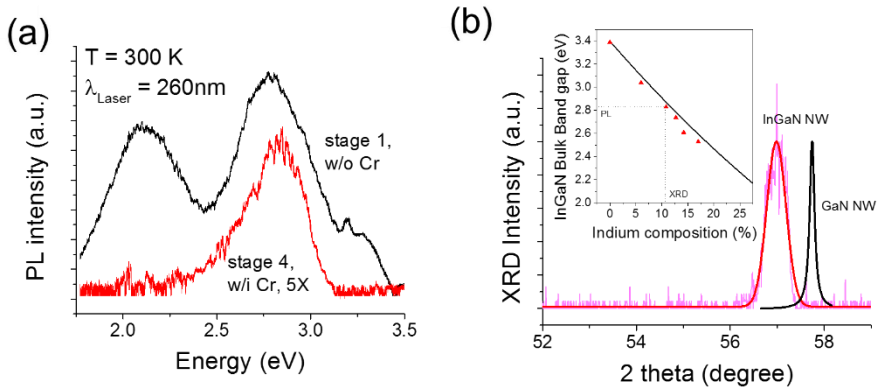

Figure 4.8: (a) PL of an InGaN NW at stages 1 and 4 in Fig. 4.2.2.1(a). PL intensity at stage 4 is five times the original intensity. (b) XRD of InGaN NW at stage 1 and of GaN NW. InGaN bulk band gap versus In composition is shown in the inset. In composition was calculated from XRD, and band gap was estimated from PL.

4.2.3 Tunable Emission Energy up to 2.5 eV

Several InGaN NW samples were investigated, as shown in Fig. 4.9. In-content tuning up to 18.6% was achieved by controlling the TMIn flow rate, as shown in Fig. 4.9(a). The XRD broadening phenomenon denotes an increasing degree of structural disorder with increased In composition. Through optimization of growth conditions, we could likely further prevent this deterioration. A range of InGaN NW densities between 5×10^8 and 8×10^8 cm^{-2} was achieved, as shown in Fig. 4.9(b). Based on a preliminary investigation, the NW density was not affected by TMIn flow. Fig. 4.9(c) illustrates PL spectra at 300 K of five InGaN NW samples and a GaN NW control sample. All samples were covered by a Cr layer with the same fabrication flows mentioned above.

The results indicate InGaN NWs with tunable emission energies by controlled TMIn flow. As expected, the FWHM spectral line width increased with In composition due to possible In composition inhomogeneity that continuously increases with In composition. Further optimization of growth conditions may be needed to improve In composition uniformity.

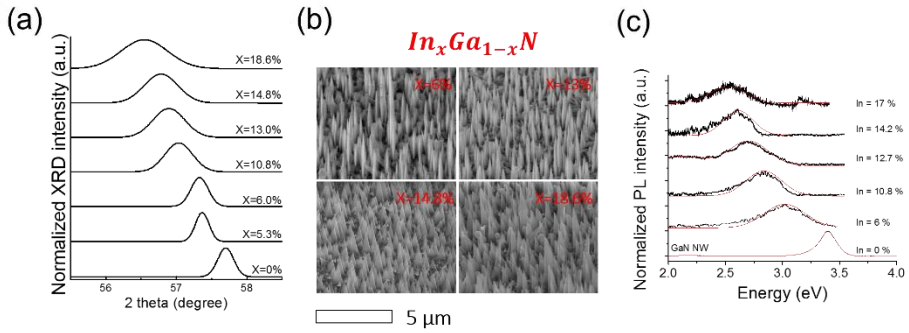

Figure 4.9: (a) Normalized XRD of InGaN NWs. In content was estimated from lattice constants. (b) SEM images of InGaN NWs at various In contents. (c) PL at stage 4 in Figure 4.7(a).

4.2.4 Overview of emission energy of bulk InGaN NW

In conclusion, we have demonstrated that InGaN NWs exhibit only high-energy emissions (*refer to section 4.1*) with the proper growth conditions. Furthermore, the In content of NWs can be controlled by TMIn flow rate with optimized growth temperature and pressure. NW emission energy can be tuned from 0 to 18.6%, which correspond to emission energies between 3.4 and 2.5 eV. In addition, In compositions from PL results match those from XRD measurements.

Table 4.1 presents the average and FWHM value of In composition from XRD, EDX and PL measurement.

The resolution of EDX analysis during TEM measurement is limited by the diameter of the electron beam. For example, the JEOL 2010 TEM system has an aperture of $10\ \mu m$ in diameter and a probe $50\ nm$ in diameter, achieving point-to-point resolution of $0.15\ nm$ in sample images. This ability makes the JEOL 2010 TEM system an ideal tool for measuring indium composition from EDX at NW scale. TEM-EDX provides In content in single NW, and other measurements can only provide an average of In content from the entire sample. Thus, result from TEM-EDX can be expected to show a broader distribution which leads to a higher FWHM value of In composition compared to other measurements. The broad distribution indicate non-uniform In content during NW growth. The fluctuation of In composition was confirmed from NW-level TEM-EDX images (*refer to section 4.1.2*). We defined the TEM-EDX measurement error as 2.05% based on the differences of FWHM values. It should be noted that the average values of In content from all measurements match between each other, suggesting that the TEM-EDX results are not outliers. However, further optimization of growth conditions may be needed to improve uniformity.

Table 4.1: The average and FWHM value of In composition from XRD, EDX, and PL measurement

	INDIUM COMPOSITION (%)	
	Average	FWHM
XRD	15.4	7.6
EDX - HORIZONTAL	16.2	10.3
EDX - VERTICAL	15.9	11.2
PL	13.6	8.4

4.3 Material Properties

4.3.1 InGaN Bottom Thin Film and Bulk Region

After InGaN NWs were grown by MOCVD, the sample was covered with $5\,\mu m$ of SiO_2 as a protecting layer for high-resolution TEM (HR-TEM) measurements. The cross-sectional TEM image shown in Fig. 4.10(a) clearly indicates the presence of a thin InGaN film between 250 and $350\,nm$ thickness on the substrate. The film buried the bottom InGaN NWs. Zoomed-in images of the NW and thin-film regions are shown in Figs. 4.10(b) and (c), respectively. High densities

of SFs and TDs are typically concentrated at the film region. The lattice mismatch was estimated as 17.3% by considering the 15% In content of the InGaN film on the *r*-plane sapphire substrate. Thus, high anisotropic elastic strain energy can be introduced during thin-film epitaxial growth. The NW geometry could fully release the surface strain energy and thus greatly reduce SF and TD densities. Based on the strain distribution in InGaN NWs with diameter of $300\,nm$, the epitaxial strain decreased to zero after moving $150\,nm$ away from the substructure. *(Data not shown)* 2D simulation processed by NEXTNANO.

The most interesting feature of InGaN NWs is their near lack of dislocations in the region approximately $480\,nm$ above the substrate. We observed highly ordered crystal structures, as shown in Fig. 4.10(b). In addition, the selected area diffraction (SAED) pattern exhibited the wurtzite crystal structure, as shown in the inset of Fig. 4.10(b). Based on the alignment of the pattern to a real space image, the NWs were confirmed to grow along the *a*-plane [11$\underline{2}$0] direction, perpendicular to the substrate. The growth direction is represented as the "g" vector in all figures. The results agreed with those of similar studies of GaN NWs grown on *r*-plane sapphires using Ni catalysts [90].

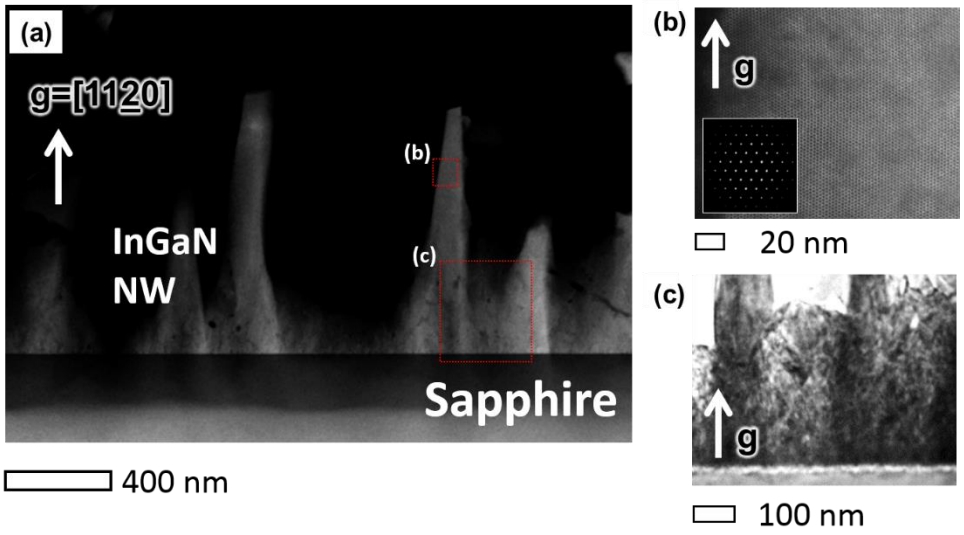

Figure 4.10: TEM images of (a) an InGaN NW sample at low magnification; (b) an InGaN NW side wall 500 nm away from substrate; (c) interface between InGaN and *r*-sapphire substrate. The NW growth direction is along the [11$\bar{2}$0] direction (*a*-plane), represented as g.

4.3.2 InGaN NW Surface Oxide Layer

Gallium oxide (Ga_2O_3) layers prefer to form epitaxially at the surface of NWs, as shown in the high-angle annular dark field (HAADF) image in Fig. 4.11(a). Based on the low-magnification STEM images shown in Figs. 4.11(b) and (c), we observed a thin, uniform oxide layer at the NW side wall, where enhanced resistance arises from the natural formation of an oxide layer on its surface. Based on STEM images with various focuses between 0 and $-42\,nm$, we observed a single crystalline epitaxial oxide layer with thickness between 3 and $5\,nm$ in most NWs with approximately $100\,nm$ diameters. However, these images do not provide

information about interfacial roughness or atomic structure. The TEM-EDX elemental line profile confirms the formation of a Ga_2O_3 layer when scanned across from point A to B, as shown in Fig. 4.11(d). During InGaN NW growth, the samples were grown in a N_2 environment at high temperature. The impurity of the N_2 source could result in the formation of an oxide layer during growth. Further investigation is required to understand when the oxidized layer is formed. This thin oxide layer was easily removed by chemical solution and thus should not significantly affect device performance.

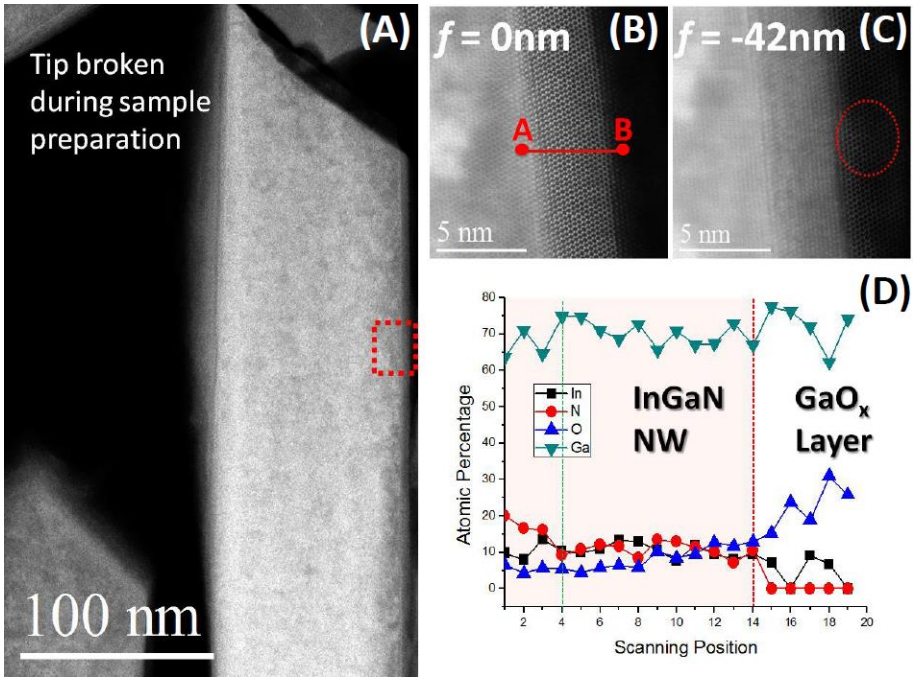

Figure 4.11: TEM images of (a) HAADF and low-magnification STEM images with focuses of (b) 0 and (c) -42 nm; (d) TEM-EDX image from the NWs to the oxide layer.

4.3.3 InGaN NW Tip

The SEM images indicated the presence of a sharp end on all NWs. TEM measurements were performed on the smaller NWs (with diameters of approximately $100\,nm$) and tips shaped into a layered structure were observed, as shown in Fig. 4.12(a). Fig. 4.12(b), a close-up HAADF image (rectangular area in Fig. 4.12(a)), clearly demonstrated that each layer is approximately $15\,nm$ thick. A thickness variation map is shown in Fig. 4.12(c), obtained from the focus series study using geometric phase analysis. Each layer is separated with a step. The layered structure is evidence of thin-film epitaxial growth and only occurs at the end of NW axial growth after the catalysts disappear. In addition, catalyst size is reduced as growth time increases linearly. Small NWs reach thin-film epitaxial growth more easily than large NWs. Therefore, we only observed this phenomenon for NWs with diameters of less than $100\,nm$. An EDX line scan was also performed, as shown in Figs. 4.12(d) and (e). InGaN NWs exhibit symmetrically varying In compositions from their center.

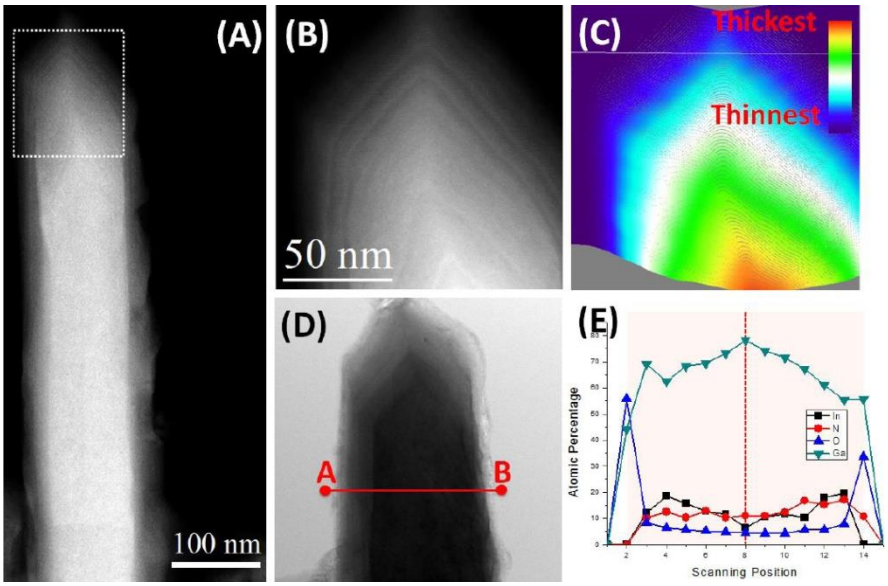

Figure 4.12: TEM images of (a) HAADF and (b) close-up image of the NW tip region; (c) geometric phase analysis for a needlelike NW; (d) TEM image, with (e) an EDX line scan image from A to B.

4.3.4 Overview of material properties

In summary, the growth of InGaN NWs has been confirmed along the non-polar [11$\underline{2}$0] direction. The TEM results demonstrated the presence of InGaN NWs free of SFs and TDs; most defects are confined to the bottom InGaN thin-film region. At the NW surface, we observed a crystalline Ga_2O_3 layer that may form during growth. At the tip region, we observed a layered structure with a symmetrically varying In composition. These results are solid evidence that thin-film epitaxial growth dominates at the tips of elevated NWs.

4.4 Summary

In this chapter, we studied the optical properties of InGaN NWs with PL, CL, and TEM-EDX and characterized the material with SEM, TEM, and XRD. Although nearly defect-free InGaN was observed by TEM, we detected both localized and InGaN emissions from InGaN NWs. Through optimized growth conditions, we can suppress the localized emission and enhance the bulk InGaN NW emission. We also confirm that the emission energy from InGaN NW can be tuned from 3.4 to 2.5 eV by controlling the TMIn flow rate. These emission energies match the bulk InGaN band gap estimated from the In content. Furthermore, TRPL indicated that InGaN NWs have 45% internal quantum efficiency and extremely short carrier lifetimes. These results are promising, as they demonstrate that InGaN NWs have potential for optoelectronic devices and provide significant implications for PV applications.

According to the investigation of InGaN NWs, we found that most SFs and TDs are concentrated and confined to the bottom part of an InGaN thin film, and InGaN NW remains free of defects. These defect structures are induced by strain at the interface between the epitaxial layer and sapphire substrate. In addition, an oxide layer formed at NW side walls could induce surface recombination and degrade optical performance. A layered structure at the tip of a NW corresponds to thin-film epitaxial growth at the end, confirming our hypothesized growth model introduced in chapter 2.

CHAPTER 5

Contributions and Future Work

5.1 Overview of Contributions

The most common commercial and technical solutions for solar cell devices are mainly Si- and GaAs-based materials. Lower-band gap materials absorb low-energy photons, which increase the material's carrier generation and photocurrent. However, the ideal conversation efficiency in a single-junction solar cell is 33% at a band gap of 1.4 eV. This limitation may be overcome in a tandem solar cell. The challenges associated with the development of a tandem solar cell are in designing more complex structures and lattice-matching alloys. Nitride semiconductors have recently gained considerable attention in photovoltaic applications due to the small band gap of ternary alloy InGaN and lattice-matched features. Furthermore, the InGaN emission spectrum spans from ultraviolet to infrared. This material has the potential to increase the conversion efficiency by over 50% by tandem technology.

Preliminary InGaN solar cell development is based on the optimization of the components of the InGaN structure, such as In content, thickness, and doping level,

to enhance the structure's performance. Increasing the In mole fraction in the InGaN alloy would decrease the alloy's band gap but increase the lattice mismatch between the epitaxial layer and substrate. Therefore, it is difficult to grow defect-free InGaN with a certain thickness at high In contents. In reality, due to the high In content, epitaxial film contains intrinsic defects that increase the density of traps and recombination centers. These issues decrease the short circuit current density in photovoltaic applications.

In this study, we first developed vertically aligned InGaN NWs with tunable In content. Due to their geometry, these NWs can be grown without defects on any lattice-mismatched substrate. Furthermore, we developed GaN on the NW-templated structure with few defects. Due to the suspension of the film, many of the defects are confined at the base of the NW region and remain a perfect film at the end of the growth process. To achieve high-performance optoelectronic applications, we propose the potential solution of vertically aligned InGaN NWs and *a*-plane GaN suspended by NWs to improve crystal quality. The goal of our work is to overcome the limitations of InGaN-based devices.

5.1.1 Vertical InGaN NWs

Defect-free vertically aligned bulk InGaN NWs were achieved by MOCVD for the first time. Based on our studies, we modeled the growth of InGaN NWs via the VSS mechanism and demonstrated that the In content of the InGaN alloy can be

continuously tuned from 0 to 19%. The emission energy from InGaN NWs covers the blue and green parts of the visible spectrum. Because of these significant wavelengths, our work demonstrates the potential to impact efficient energy conversion in PV applications and enable the use of InGaN NWs in high-power LEDs and LD devices. In future work, we will further demonstrate the possibilities of making solar cell devices using InGaN NWs. It is possible to overcome the current limitations of InGaN-based devices, namely, material quality and the total thickness of the InGaN layers that can be stacked on the substrate.

5.1.2 High-quality a-plane GaN

The unique growth mechanism of NWs can circumvent the strain induced at the epitaxial and sapphire substrate interface, thus allowing for the growth of defect- and strain-free materials by effectively relaxing the strain on the lattice-mismatched substrate. We report the growth of an *a*-plane GaN thin film on top of GaN NWs by MOCVD. We analyzed the microstructural properties and discovered small-angle tilts and twists of the GaN NWs, which were the main causes of defects in the GaN films. We then developed a novel multi-stack growth process to further improve the *a*-plane GaN film quality. Based on the results, the first *a*-plane GaN film grown on a NW template exhibits improved surface morphology and anisotropic growth along the *c*- and *m*-axes compared to the control sample. Based on these results, the *a*-

plane GaN film grown on the third-stack NW template exhibits more isotropic growth.

5.2 Future Work

5.2.1 Development of Solar Cells using InGaN NWs

We previously demonstrated the concept of improving the material quality of InGaN NWs. We identified the limitations of InGaN-based solar cells and overcome the material issues of such devices. Our next step is to address the device design of InGaN-based solar cells. In this chapter, we focus on the development of a prototype InGaN solar cell from InGaN NWs. Preliminary InGaN NWs are fabricated to test the photocurrent response.

5.2.2 Device Concepts

The aim of this work is to develop a high-performance InGaN NW solar cell with a band gap of 2.5 eV. Absorption measurements were made to verify which InGaN NW samples respond to incident spectra. In this study, we use an AM 1.5 solar simulator as an incident light source, an integrating sphere, and optical fiber as the measurement tools. To minimize background noise, the incident light passes through two beam cutters before being guided into the integrating sphere. The size

and intensity of the incident light are reduced after it passes through two beam cutters. Based on the size of the incident light, we estimated that only 0.1% of the intensity of AM 1.5 was used. The incident beam is perpendicular to the sample, and the collector is through a fiber from the side wall of the integrating sphere. Fig. 5.1(a) presents the specifications of the setup, and Fig. 5.1(b) presents the absorption spectra as a function of the incident wavelength at various InGaN NW densities and of a control sample without NWs. All samples were grown simultaneously; therefore, we could ignore fluctuation of In content between samples. Absorption clearly increases with NW density. InGaN NW samples with high NW density can allow for improved solar cell devices.

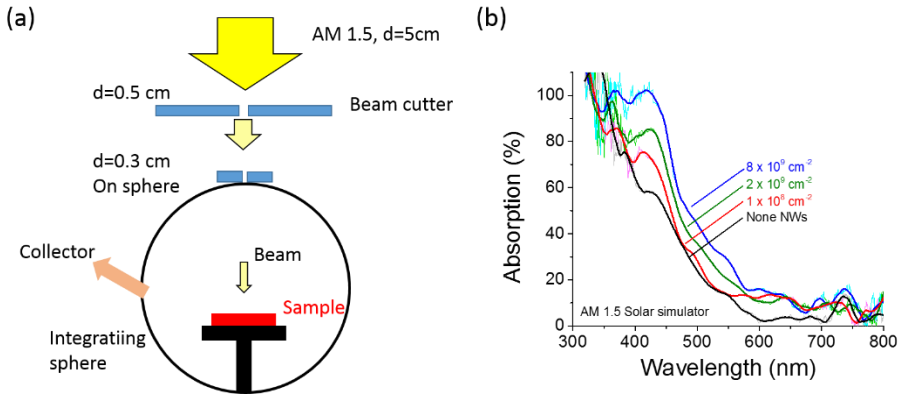

Figure 5.1: (a) Absorption measurement setup; (b) absorption at various InGaN NW densities and of a control sample without NWs.

A homo-junction-based InGaN NW sample was prepared with an n-type background doping concentration of $1.5 \times 10^{17}\ cm^{-3}$. We used the concept of a Schottky junction to transport carriers generated by incident photons [91]. Two

electrodes refer to Schottky and Ohmic contact at each side, as shown in Fig. 5.2(a). In Schottky contact, the metal side has a higher work function than the semiconductor side, whereas the opposite is true in Ohmic contact. The background doping concentration and barrier height are two key factors that deplete the InGaN NW. Fig. 5.2(b) presents an overall schematic of a prototype solar cell device using InGaN NWs. In this study, we used $50\ nm\ Pt/200\ nm\ Au$ as the bottom electrode and $10\ nm\ MoO_2$ as the front side of the electrode. Due to the thin layer of MoO2 and the transparent supporting layer of parylene, nearly 90% transparency was obtained. The fabrication details are provided below.

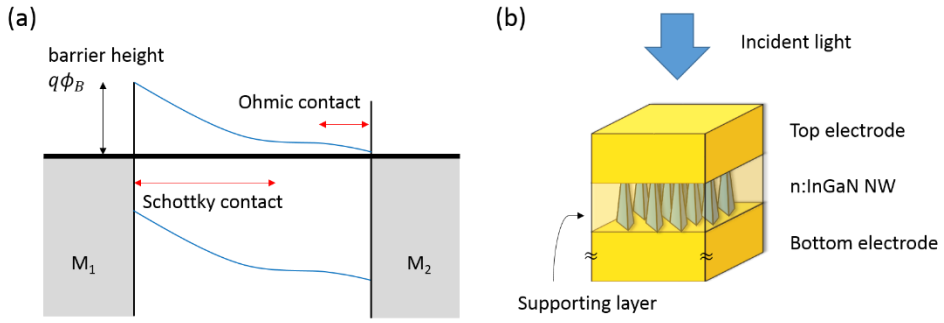

Figure 5.2: (a) Schematic of Schottky and Ohmic contacts; (b) overall diagram of InGaN solar cell device

5.2.3 Fabrication Design

As a test sample, we used InGaN NWs with a band gap of $\mathbf{2.5}\ \boldsymbol{eV}$. The crystalline quality was characterized using XRD and PL, as in the previous chapter.

The fabrication process is presented in Fig. 5.3. InGaN NW samples were grown on double-side-polished sapphire substrates with an average length of $\mathbf{1}\ \boldsymbol{\mu m}$. We then deposited a conformal coating of $\mathbf{1.5}\ \boldsymbol{\mu m}$ of transparent parylene as a protecting layer. The sample was then etched by a plasma etcher. With a proper controlling etching rate ($\mathbf{120}\ \boldsymbol{nm/min}$), we deposited a $\mathbf{200}\ \boldsymbol{nm}$ parylene layer to cover the NWs. The sample was then ready for metal deposition, with the following sequence: $\mathbf{50}\ \boldsymbol{nm}$ of platinum ($\boldsymbol{Pt}$), 200 nm of gold ($\boldsymbol{Au}$), and 1 $\boldsymbol{\mu m}$ of silver ($\boldsymbol{Ag}$). The InGaN NWs were buried by this metal combination. We used copper foil attached to the InGaN NW sample for wafer-handling. We then used a pulsed laser lift-off (LLO) on the substrate to transfer the film. The LLO method has been demonstrated by Wong *et al* [92]. With a short-pulse UV laser, the InGaN film was irradiated at the interface of film and substrate. The epitaxial layer can then detach from the sapphire substrate. We used a chemical solution to clean and etch the exposed surface. The last stage is the deposition of the bottom electrode. To form a large barrier height, a metal with a large metal work function was used. To maintain transparency for incident light, we used $\mathbf{10}\ \boldsymbol{nm}\ \boldsymbol{MoO_2}$ as the bottom electrode. In this manner, the Schottky junction was prepared for electric testing.

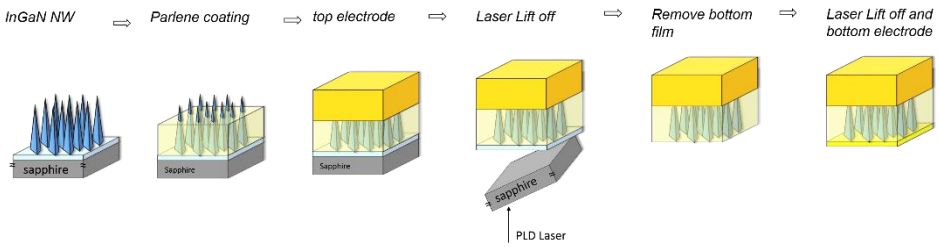

Figure 5.3: (a) schematic illustrating the fabrication process. Picture 1: InGaN NW growth to 1 μm on average; Picture 2: parylene spinning and coating to a 1.5 μm thickness and etching by plasma until the NW tops are exposed; Picture 3: metal deposition by 50 nm Pt/200 nm Au/1 μm Ag in sequence; Picture 4: lift-off substrate by the LLO process with a 248 nm pulse laser; Picture 5: removal of the bottom film by a dilute chemical solution; Picture 6: metal deposition with 10 nm MoO_2.

5.2.4 Photocurrent Response

The photocurrent response can be measured in solar cell devices due to the creation of electron-hole pairs by absorption. The IV characteristics of the test solar cells are shown in Fig. 5.4(a) to investigate a possible prototype NW device. To investigate the influence of incident light intensity, we compared the same probing spot with various incident light intensities by an attenuator. The measurement setup uses a microscope probing stage with an AM 1.5 solar simulator as the light source. The measurement used a tungsten oxide probe as the bottom electrode for convenience. Fig. 5.4(a) presents scenarios A to E, with light intensity ratios of 1, 0.7, 0.13, 0.01, and 0, respectively. The intensities are normalized to the light intensity without an attenuator, which is scenario A. The results indicate that the InGaN NW solar cell device responds to incident light. Furthermore, the photocurrent increases with increasing light intensity. Under weak illumination (scenario D), we did not

observe the open circuit voltage, but there are slight differences in the current compared to the dark current (scenario E). The open circuit voltage is increased with increasing illumination intensity. Under intense illumination, the V_{OC} was approximately $0.55\,V$, which is less than the expected value of $0.7\,V$ estimated from the height of the Schottky barrier. The values of each scenario are provided in table 5.1.

Fig. 5.4(b) presents the current and power densities as a function of forward bias in scenario A. From the plot, the maximum power density is $0.3\,mW/cm^2$, and a fill factor of approximately 33% is obtained. Based on the probing area, we can estimate that the contribution of the photocurrent originated from approximately 1,000 NWs with lengths of $200\,nm$ InGaN. The photocurrent could be further increased by increasing the NW density, increasing the array size, or reducing the fabrication error.

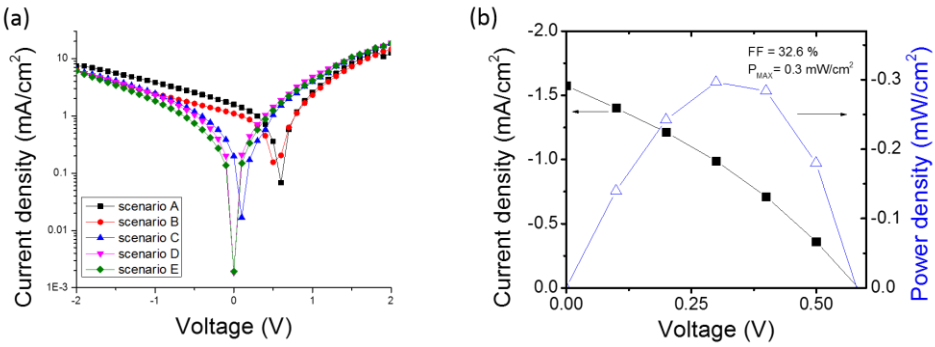

Figure 5.4: (a) I-V characteristics of InGaN NW samples with various incident light intensities; (b) current and power densities as a function of the applied voltage in scenario A.

Table 5.1: Photocurrent response from the experimental results of InGaN NW samples

Scenario	Measured values			
	Light intensity	V_{oc}	J_{sc}	Experimental ratio
A	1	0.584	1.575	1
B	0.78	0.543	1.099	0.7
C	0.27	0.110	0.198	0.13
D	0.05	0	0.002	0.01
E	0	-	-	-

5.2.5 Summary

In summary, we developed a prototype InGaN solar cell device by lift-off from a sapphire substrate and proper device fabrication. Based on the IV characteristics of the prototype device, we demonstrated Schottky and Ohmic contact at the front and bottom electrodes, respectively. Under illumination of AM 1.5 solar light, we observed the photocurrent response from InGaN NW samples with a microscope probe station. We also discovered that the photocurrent and open circuit voltage increase with increasing illumination intensity. The findings of this preliminary study suggest that InGaN NWs could represent a significant step forward in photovoltaic applications. Further improvements in device fabrication and InGaN NW density could significantly improve the device performance. Additionally, growing InGaN NWs on top of a GaN NW-templated substrate could result in a simple tandem junction device with a simpler approach. The performance of InGaN/GaN tandem cells could further increase the conventional efficiency.

APPENDICES

A

Appendix A: Wurtzite Nitrides Structure

A.1 Introduction of Wurtzite nitrides Structure

The GaN crystal structure is a wurtzite structure as opposed to the zineblend structure. The wurtzite structure holds symmetric property and can be described by the c anda lattice constant. The unite cell is shown in figure A.1. The lattice constant of c and a are related to each other for the ideal wurtzite structure. However,

$$\boldsymbol{c = 2\sqrt{\frac{2}{3}}a}$$

since the bond lengths between cation and anion do not exactly fit this relationship, a dipole moment results which is referred to as the spontaneous polarization effects [93]. The elimination of internal field effect in the III-V nitrides is done by growth orientation. The polarization discontinuities do not exist in the hetro-interfaces with growing on the *c*-plane axis such as *a*- / *m*- plane. Consequently, the internal electric field is absent in nonpolar quantum wells, and the band diagram can be flat.

Semipolar plane is the plane that has an angle with *c*-plane as shown in figure A.2. Different angles have different specific strain and polarization. The growth direction can be used to control the polarization effect [94]. Therefore, fabricating LEDs and LDs on semipolar or nonpolar could improve the performance of devices.

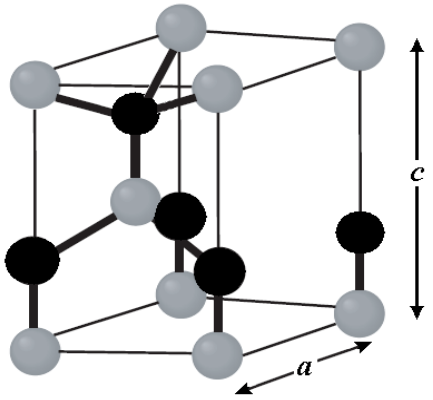

Figure A.1Wurtzite unit cell

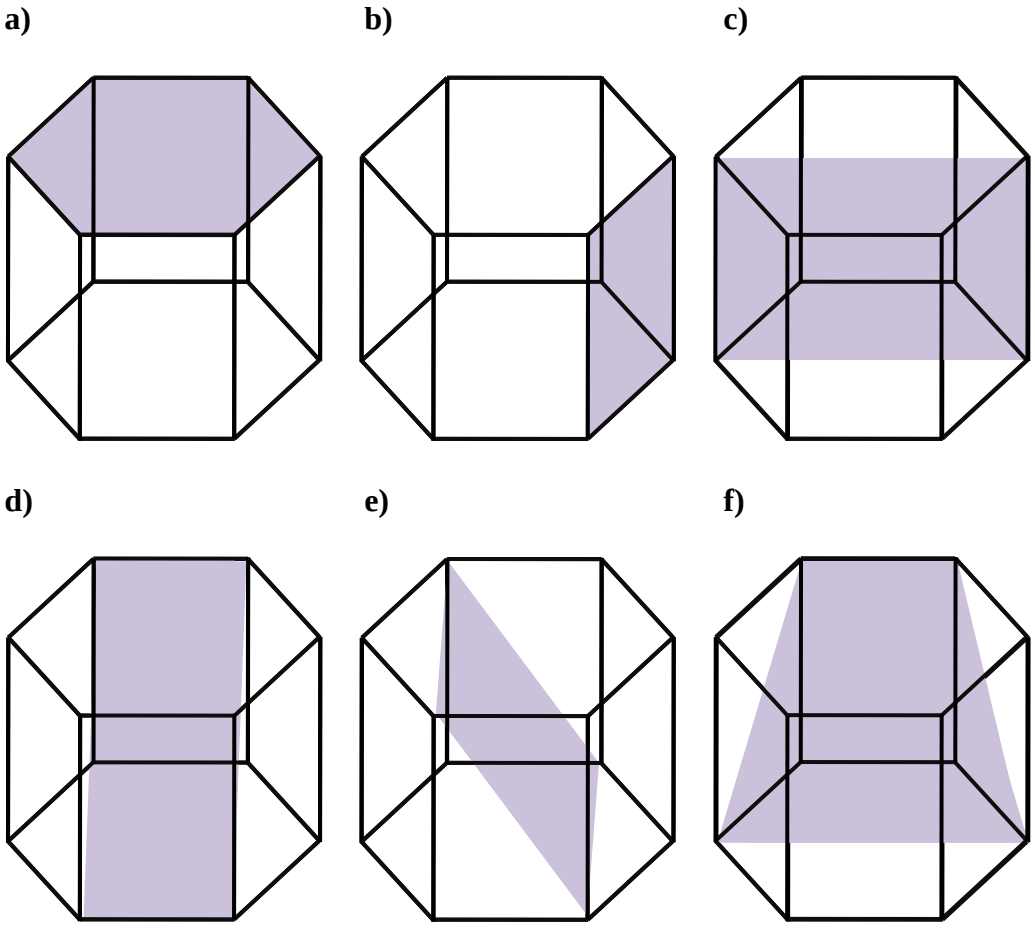

Figure A.2 Crystallography of wurtzite nitrides. Illustration of a) *c*-plane[0001] b) *m*-plane [10$\underline{1}$0] c) *a*-plane [11$\underline{2}$0]d) *r*- plane [1$\underline{1}$02]e) [11$\underline{2}$2]) f) [10$\underline{1}$0])

B

Appendix B: Parameters for III-nitrides

Material	GaN	$In_{0.05}Ga_{0.95}N$	$In_{0.2}Ga_{0.8}N$	InN
Band Gap (eV)	3.42	3.215	2.642	0.65
Electron Affinity (eV)	4.1	4.24825	4.672	6.4
Nc/Nv Ratio	0.038764	0.037836	0.034864	0.016424
Intrinsic Concentration: 200K (cm^{-3})	5.82E-25	2.16E-22	3.27E-15	2.58E+10
Intrinsic Concentration: 300K (cm^{-3})	2.35E-10	1.21E-08	7.21E-04	2.52E+13
Intrinsic Concentration: 400K (cm^{-3})	0.005368	0.10229	384.9695	8.94E+14
Dielectric constant	8.9	9.22	10.18	15.3
Electron Mobility (cm^2/Vs)	400	400	400	400
Hole Mobility (cm^2/Vs)	10	10	10	10
Refractive Index	2.29	2.3205	2.412	2.9
Auger Coefficients: n-type (cm^6/s)	1.4 E-30	1.4 E-30	1.4 E-30	1.4 E-30
Auger Coefficients: p-type (cm^6/s)	1.4 E-30	1.4 E-30	1.4 E-30	1.4 E-30
Auger Coefficients: high-inject (cm^6/s)	1.4 E-30	1.4 E-30	1.4 E-30	1.4 E-30
Band-to-Band (cm^3/s)	2.4 E-11	2.31 E-11	2.05 E-11	6.60E-11
Polarization Coefficients				
Spontaneous Polarization: P_{SP} (C/m^2)	-0.0340	-0.0326	-0.0297	-0.0420
Piezoelectric Constant: e_{31} (C/m^2)	0.730	0.742	0.778	0.970
Piezoelectric Constant: e_{33} (C/m^2)	-0.490	-0.494	-0.506	-0.570
Elastic Constant: c_{13} (Gpa)	1.03E+02	1.02E+02	1.01E+02	9.20E+01
Elastic Constant: c_{13} (Gpa)	4.05E+02	3.96E+02	3.69E+02	2.24E+02
Lattice Constant: a (Å)	3.189	3.2062	3.2578	3.533

BIBLIOGRAPHY

[1] Wu, J., et al. "Small band gap bowing in InGaN alloys." *Applied Physics Letters* 80 (2002): 4741.

[2] Krames, Michael R., et al. "Status and future of high-power light-emitting diodes for solid-state lighting." *Display Technology, Journal of* 3.2 (2007): 160-175.

[3] Shilkrot, L. E., D. J. Srolovitz, and J. Tersoff. "Morphology evolution during the growth of strained-layer superlattices." *Physical Review B* 62.12 (2000): 8397.

[4] A. A. Chernov, Modern Crystallography III, Crystal Growth (Springer-Verlag, Berlin, Heidelberg, New York, Tokyo, 1984), Chapters 1, 2.

[5] Morkoc, H., et al. "Large-band-gap SiC, III-V nitride, and II-VI ZnSe-based semiconductor device technologies." *Journal of Applied Physics* 76.3 (1994): 1363-1398.

[6] Jain, S. C., et al. "III–nitrides: Growth, characterization, and properties." *Journal of Applied Physics* 87.3 (2000): 965-1006.

[7] Pearton, S. J., et al. "GaN: Processing, defects, and devices." *Journal of Applied Physics* 86.1 (1999): 1-78.

[8] Ponce, F. A., et al. "Microstructure of GaN epitaxy on SiC using AlN buffer layers." *Applied physics letters* 67.3 (1995): 410-412.

[9] Shen, Y. C., et al. "Auger recombination in InGaN measured by photoluminescence." *Applied Physics Letters* 91 (2007): 141101.

[10] David, Aurélien, and Michael J. Grundmann. "Droop in InGaN light-emitting diodes: A differential carrier lifetime analysis." *Applied Physics Letters* 96.10 (2010): 103504-103504.

[11] Kioupakis, Emmanouil, et al. "Indirect Auger recombination as a cause of efficiency droop in nitride light-emitting diodes." *Applied Physics Letters* 98.16 (2011): 161107-161107.

[12] Kim, Min-Ho, et al. "Origin of efficiency droop in GaN-based light-emitting diodes." *Applied Physics Letters* 91 (2007): 183507.

[13] Ni, X., et al. "Hot electron effects on efficiency degradation in InGaN light emitting diodes and designs to mitigate them." *Journal of Applied Physics* 108.3 (2010): 033112-033112.

[14] Hader, J., J. V. Moloney, and S. W. Koch. "Density-activated defect recombination as a possible explanation for the efficiency droop in GaN-based diodes." *SPIE OPTO*. International Society for Optics and Photonics, 2011.

[15] Walukiewicz, W., et al. "Structure and electronic properties of InN and In-rich group III-nitride alloys." *Journal of Physics D: Applied Physics* 39.5 (2006): R83.

[16] Hsu, L., and W. Walukiewicz. "Modeling of InGaN/Si tandem solar cells."*Journal of Applied Physics* 104.2 (2008): 024507-024507.

[17] Yamamoto, Akio, et al. "Recent advances in InN-based solar cells: status and challenges in InGaN and InAlN solar cells." *physica status solidi (c)* 7.5 (2010): 1309-1316.

[18] Neufeld, Carl J., et al. "Effect of doping and polarization on carrier collection in InGaN quantum well solar cells." *Applied Physics Letters* 98.24 (2011): 243507-243507.

[19] Wierer, J. J., A. J. Fischer, and D. D. Koleske. "The impact of piezoelectric polarization and nonradiative recombination on the performance of (0001) face GaN/InGaN photovoltaic devices." *Applied Physics Letters* 96.5 (2010): 051107-051107.

[20] Dahal, R., et al. "InGaN/GaN multiple quantum well concentrator solar cells."*Applied Physics Letters* 97.7 (2010): 073115-073115.

[21] Farrell, Rober M., et al. "High quantum efficiency InGaN/GaN multiple quantum well solar cells with spectral response extending out to 520 nm." *Applied Physics Letters* 98.20 (2011): 201107-201107.

[22] Matioli, Elison, et al. "High internal and external quantum efficiency InGaN/GaN solar cells." *Applied Physics Letters* 98.2 (2011): 021102-021102.

[23] Hwang, Yun Jeong, et al. "Si/InGaN core/shell hierarchical nanowire arrays and their photoelectrochemical properties." *Nano letters* 12.3 (2012): 1678-1682.

[24] Qian, Fang, et al. "Core/multishell nanowire heterostructures as multicolor, high-efficiency light-emitting diodes." *Nano letters* 5.11 (2005): 2287-2291.

[25] Duan, Xiangfeng, et al. "Indium phosphide nanowires as building blocks for nanoscale electronic and optoelectronic devices." *Nature* 409.6816 (2001): 66-69.

[26] Duan, Xiangfeng, et al. "Single-nanowire electrically driven lasers." *Nature* 421.6920 (2003): 241-245.

[27] Lauhon, Lincoln J., et al. "Epitaxial core–shell and core–multishell nanowire heterostructures." *Nature* 420.6911 (2002): 57-61.

[28] Dong, Yajie, et al. "Coaxial group III− nitride nanowire photovoltaics." *Nano letters* 9.5 (2009): 2183-2187.

[29] Li, Qiming, and George T. Wang. "Strain influenced indium composition distribution in GaN/InGaN core-shell nanowires." *Applied Physics Letters* 97.18 (2010): 181107-181107.

[30] Dogan, Pinar, et al. "GaN nanowire templates for the pendeoepitaxial coalescence overgrowth on Si (111) by molecular beam epitaxy." *Journal of Crystal Growth* 323.1 (2011): 418-421.

[31] Yeom, Bo-Ra, et al. "Growth behavior of GaN epilayers on Si (111) grown by GaN nanowires assisted epitaxial lateral overgrowth." *CrystEngComm* 14.17 (2012): 5558-5563

[32] Kim, Hwa-Mok, et al. "High-brightness light emitting diodes using dislocation-free indium gallium nitride/gallium nitride multiquantum-well nanorod arrays."*Nano letters* 4.6 (2004): 1059-1062.

[33] A.R. Guichard, D.N. Barsic, T.I. Kamins, S. Sharma, M.L. Brongersma. “Light Emission from Quantum-Confined Excitons in Silicon Nanowires Grown via Chemical Vapor Deposition.” *Nano Letters*, **6**, (2006) 2140

[34] Armitage, R., and K. Tsubaki. "Multicolour luminescence from InGaN quantum wells grown over GaN nanowire arrays by molecular-beam epitaxy."*Nanotechnology* 21.19 (2010): 195202.

[35] Calarco, Raffaella, et al. "Nucleation and growth of GaN nanowires on Si (111) performed by molecular beam epitaxy." *Nano letters* 7.8 (2007): 2248-2251.

[36] Cerutti, L., et al. "Wurtzite GaN nanocolumns grown on Si (001) by molecular beam epitaxy." *Applied physics letters* 88.21 (2006): 213114-213114.

[37] Kuykendall, Tevye, et al. "Complete composition tunability of InGaN nanowires using a combinatorial approach." *Nature materials* 6.12 (2007): 951-956.

[38] Guo, Wei, et al. "Catalyst-free InGaN/GaN nanowire light emitting diodes grown on (001) silicon by molecular beam epitaxy." *Nano letters* 10.9 (2010): 3355-3359.

[39] Huang, Jeng-Jie, et al. "Improved a-plane GaN quality grown with flow modulation epitaxy and epitaxial lateral overgrowth on r-plane sapphire substrate." *Applied Physics Letters* 92 (2008): 231902.

[40] Gao, Haiyong, et al. "Growth of nonpolar a-plane GaN on nano-patterned r-plane sapphire substrates." *Applied Surface Science* 255.6 (2009): 3664-3668

[41] Li, Qiming, et al. "Nanowire-Templated Lateral Epitaxial Growth of Low-Dislocation Density Nonpolar a-Plane GaN on r-Plane Sapphire." *Advanced Materials* 21.23 (2009): 2416-2420

[42] Chakraborty, Arpan, et al. "Defect reduction in nonpolar a-plane GaN films using in situ SiNx nanomask." *Applied physics letters* 89.4 (2006): 041903-041903

[43] Ko, T. S., et al. "Study on optimal growth conditions of a-plane GaN grown on r-plane sapphire by metal-organic chemical vapor deposition."*Journal of crystal growth* 300.2 (2007): 308-313

[44] Miyagawa, R., et al. "Reactor-pressure dependence of growth of a-plane GaN on r-plane sapphire by MOVPE." *Journal of Crystal Growth* 310.23 (2008): 4979-4982

[45] Dogan, Pinar, et al. "GaN nanowire templates for the pendeoepitaxial coalescence overgrowth on Si (111) by molecular beam epitaxy." *Journal of Crystal Growth* 323.1 (2011): 418-421.

[46] Yeom, Bo-Ra, et al. "Growth behavior of GaN epilayers on Si (111) grown by GaN nanowires assisted epitaxial lateral overgrowth." *CrystEngComm* 14.17 (2012): 5558-5563

[47] Kim, Dong Chan, et al. "ZnO Wurtzite Single Crystals Prepared by Nanorod-Assisted Epitaxial Lateral Overgrowth." *Crystal Growth & Design* 10.1 (2009): 321-326

[48] Cao, X. A., and S. D. Arthur. "High-power and reliable operation of vertical light-emitting diodes on bulk GaN." *Applied physics letters* 85.18 (2004): 3971-3973.

[49] Fujii, T., et al. "Increase in the extraction efficiency of GaN-based light-emitting diodes via surface roughening." *Applied physics letters* 84.6 (2004): 855-857.

[50] Chen, W. H., et al. "Study of the structural damage in the (0001) GaN epilayer processed by laser lift-off techniques." *Applied Physics Letters* 91.12 (2007): 121114-121114.

[51] Othman, M. F., et al. "Current crowding effect in lateral and vertical LED configurations: 3D simulation and characterisation." *Control System, Computing and Engineering (ICCSCE), 2012 IEEE International Conference on*. IEEE, 2012.

[52] Ertekin, Elif, et al. "Equilibrium limits of coherency in strained nanowire heterostructures." *Journal of Applied Physics* 97.11 (2005): 114325-114325.

[53] Amano, Hiroshi, et al. "P-type conduction in Mg-doped GaN treated with low-energy electron beam irradiation (LEEBI)." *Jpn. J. Appl. Phys* 28.12 (1989): L2112-L2114.

[54] Nakamura, Shuji, Masayuki Senoh, and Takashi Mukai. "Highly p-typed Mg-doped GaN films grown with GaN buffer layers." *Japanese journal of applied physics* 30.10A (1991): 1708-1711.

[55] Matsuoka, Takashi. "Calculation of unstable mixing region in wurtzite In1-x-yGaxAlyN." *Applied physics letters* 71.1 (1997): 105-106.

[56] Kondow, Masahiko, et al. "GaInNAs: A novel material for long-wavelength-range laser diodes with excellent high-temperature performance." *Japanese Journal of Applied Physics* 35.part 1 (1996): 1273-1275.

[57] Dahal, R., et al. "InGaN/GaN multiple quantum well solar cells with long operating wavelengths." *Applied Physics Letters* 94.6 (2009): 063505-063505.

[58] Shioda, Tomonari, et al. "Enhanced light output power of green LEDs employing AlGaN interlayer in InGaN/GaN MQW structure on sapphire (0001) substrate."*physica status solidi (a)* 209.3 (2012): 473-476.

[59] Crawford, Mary H. "LEDs for solid-state lighting: performance challenges and recent advances." *Selected Topics in Quantum Electronics, IEEE Journal of*15.4 (2009): 1028-1040.

[60] Craven, M. D., et al. "Structural characterization of nonpolar (1120) a-plane GaN thin films grown on (1102) r-plane sapphire." *Applied physics letters* 81 (2002): 469

[61] Wagner, R. S., and W. C. Ellis. "Vapor-liquid-solid mechanism of single crystal growth." *Applied Physics Letters* 4.5 (1964): 89-90.

[62] Wu, Yiying, and Peidong Yang. "Direct observation of vapor-liquid-solid nanowire growth." *Journal of the American Chemical Society* 123.13 (2001): 3165-3166.

[63] Campos, Leonardo C., et al. "Vapor–Solid–Solid Growth Mechanism Driven by Epitaxial Match between Solid AuZn Alloy Catalyst Particles and ZnO Nanowires at Low Temperatures." *Advanced Materials* 20.8 (2008): 1499-1504

[64] Li, C. B., et al. "Vapor-solid-solid radial growth of Ge nanowires." *Journal of Applied Physics* 106.4 (2009): 046102-046102

[65] Persson, Ann I., et al. "Solid-phase diffusion mechanism for GaAs nanowire growth." *Nature materials* 3.10 (2004): 677-681.

[66] Zubia, D., and S. D. Hersee. "Nanoheteroepitaxy: The Application of nanostructuring and substrate compliance to the heteroepitaxy of mismatched semiconductor materials." *Journal of applied physics* 85.9 (1999): 6492-6496

[67] Haskell, B. A., et al. "Defect reduction in (11$\underline{2}$0) a-plane gallium nitride via lateral epitaxial overgrowth by hydride vapor-phase epitaxy." *Applied physics letters* 83.4 (2003): 644-646.

[68] Yoo, Jinkyoung, et al. "Photoluminescent characteristics of Ni-catalyzed GaN nanowires." *Applied physics letters* 89.4 (2006): 043124-043124

[69] Liu, R., et al. "Luminescence from stacking faults in gallium nitride." *Applied Physics Letters* 86.2 (2005): 021908-021908

[70] Reshchikov, M. A., et al. "Manifestation of edge dislocations in photoluminescence of GaN." *Physica B: Condensed Matter* 367.1 (2005): 35-39

[71] Chen, Hung-Ying, et al. "Structure and photoluminescence properties of epitaxially oriented GaN nanorods grown on Si (111) by plasma-assisted molecular-beam epitaxy." *Applied physics letters* 89.24 (2006): 243105-243105

[72] Luryi, Serge, and Ephraim Suhir. "New approach to the high quality epitaxial growth of lattice-mismatched materials." *Applied physics letters* 49.3 (1986): 140-142

[73] Alizadeh, A., et al. "Templated wide band-gap nanostructures." *Journal of applied physics* 95.12 (2004): 8199-8206

[74] Wang, Hongmei, et al. "Anisotropic structural characteristics of (11$\underline{2}$ 0) GaN templates and coalesced epitaxial lateral overgrown films deposited on (101$\underline{2}$) sapphire." *Applied physics letters* 84.4 (2004): 499-501

[75] Zytkiewicz, Z. R., et al. "Tilt and dislocations in epitaxial laterally overgrown GaAs layers." *Journal of applied physics* 101.1 (2007): 013508-013508

[76] Sakai, Akira, Haruo Sunakawa, and Akira Usui. "Transmission electron microscopy of defects in GaN films formed by epitaxial lateral overgrowth."*Applied physics letters* 73.4 (1998): 481-483

[77] Cheze, Caroline, et al. "Collector Phase Transitions during Vapor− Solid− Solid Nucleation of GaN Nanowires." *Nano letters* 10.9 (2010): 3426-3431.

[78] Li, Qiming, and George T. Wang. "Improvement in aligned GaN nanowire growth using submonolayer Ni catalyst films." *Applied Physics Letters* 93.4 (2008): 043119-043119

[79] Wang, George T., et al. "Highly aligned, template-free growth and characterization of vertical GaN nanowires on sapphire by metal–organic chemical vapour deposition." *Nanotechnology* 17.23 (2006): 5773.

[80] Qian, Fang, et al. "Gallium nitride-based nanowire radial heterostructures for nanophotonics." *Nano letters* 4.10 (2004): 1975-1979

[81] Qian, Fang, et al. "Core/multishell nanowire heterostructures as multicolor, high-efficiency light-emitting diodes." *Nano letters* 5.11 (2005): 2287-2291

[82] Qian, Fang, et al. "Multi-quantum-well nanowire heterostructures for wavelength-controlled lasers." *Nature materials* 7.9 (2008): 701-706

[83] Jindal, Vibhu, and Fatemeh Shahedipour-Sandvik. "Theoretical prediction of GaN nanostructure equilibrium and nonequilibrium shapes." *Journal of Applied Physics* 106.8 (2009): 083115-083115

[84] Dubrovskii, Vladimir G., et al. "Scaling thermodynamic model for the self-induced nucleation of GaN nanowires." *Physical Review B* 85.16 (2012): 165317

[85] Wu, J., et al. "Small band gap bowing in InGaN alloys." *Applied Physics Letters*80 (2002): 4741

[86] Moses, Poul Georg, and Chris G. Van de Walle. "Band bowing and band alignment in InGaN alloys." *Applied Physics Letters* 96.2 (2010): 021908-021908

[87] Shapiro, N. A., et al. "Relation between Structural Parameters and the Effective Electron–Hole Separation in InGaN/GaN Quantum Wells." *physica status solidi (b)* 228.1 (2001): 147-151

[88] Cho, Yong-Hoon, et al. "“S-shaped” temperature-dependent emission shift and carrier dynamics in InGaN/GaN multiple quantum wells." *Applied physics letters*73.10 (1998): 1370-1372

[89] Moses, Poul Georg, and Chris G. Van de Walle. "Band bowing and band alignment in InGaN alloys." *Applied Physics Letters* 96.2 (2010): 021908-021908

[90] Wang, George T., et al. "Highly aligned, template-free growth and characterization of vertical GaN nanowires on sapphire by metal–organic chemical vapour deposition." *Nanotechnology* 17.23 (2006): 5773

[91] Mahala, Pramila, et al. "A study on the 2D simulation of Pt/InGaN/GaN/metal Schottky junction solar cell." *Semiconductor Science and Technology* 28.5 (2013): 055012

[92] Wong, W. S., et al. "Fabrication of thin-film InGaN light-emitting diode membranes by laser lift-off." *Applied physics letters* 75.10 (1999): 1360-1362

[93] Tavernier, P. R., et al. "The growth of N-face GaN by MOCVD: effect of Mg, Si, and In." *Journal of crystal growth* 264.1 (2004): 150-158.

[94] Fiorentini, Vincenzo, et al. "Effects of macroscopic polarization in III-V nitride multiple quantum wells." *Physical Review B* 60.12 (1999): 8849.